Fluid Effects on Attenuation and Dispersion of Elastic Waves

by

Kumar Gautam

A thesis submitted to the Faculty and the Board of Trustees of the Colorado School of Mines in partial fulfillment of the requirements for the degree of Master of Science (Geophysics).

Golden, Colorado

Date _____

Signed: _____
Kumar Gautam

Approved: _____
Dr. Michael Batzle
Professor of Geophysics
Thesis Advisor

Golden, Colorado

Date _____

_____
Dr. Terence Young
Professor & Department Head
Department of Geophysics

ABSTRACT

Attenuation ($1/Q$, inverse of quality factor) is a fundamental property of rocks with great potential to discriminate fluid types and processes. In sedimentary rocks attenuation is dominated by fluid-rock interactions. Fluid motion in the pores cause energy loss through several mechanisms, and as a result $1/Q$ is strongly frequency dependent. However $1/Q$ is poorly understood, largely due to lack of reliable data. Almost all the reported $1/Q$ laboratory measurements are in the megahertz frequency range with high strain levels which does not lie in the seismic frequency-amplitude range. To address this issue, a low-frequency, low-amplitude apparatus was used to measure both seismic frequency velocities and attenuations.

Strain gages bonded directly to the surface of the rock allow simultaneous measurement of complex *compressional* and *shear* moduli, giving both velocity and attenuation. The losses can be separated into Bulk ($1/Q_K$), shear ($1/Q_S$), compressional ($1/Q_P$) and Young's ($1/Q_E$) modes. Confining pressure, saturation, and pore pressure can all be controlled independently. A sinusoidal stress is applied such that sample strain amplitudes remain below 10^{-7}, yet phase angles can be resolved within 0.1 degree. The frequency range is between 25 Hz and 1000 Hz. The low frequencies are thus directly applicable to seismic exploration and broad bandwidth allows investigation of loss mechanism and velocity dispersion.

After calibration, a series of experiments were carried out on sandstone and carbonate samples concentrating on the role of fluids in determining the frequency-

dependent elastic and inelastic responses of the rock-fluid system. Attenuations and velocities were measured at different saturations, pressures and boundary conditions. Velocity increases and attenuation decreases with increasing differential pressure. Attenuation due to grain contact is not the major source and movement of pore fluids is the major cause of energy loss. Different modes of attenuation are related to each other and these inequality relations change with saturation state. Bulk attenuation is twice the shear attenuation at partial saturations and at full saturation bulk and compressional attenuation values drop to half that of shear attenuation. At full saturation, opening the sample boundary can significantly change the attenuation and velocity values: acoustic velocity decreases and attenuation increases. This effect is only observed at low-frequencies, and depends on fluid mobility. Maximum attenuation is observed at partial gas saturation. Laboratory measurements show that velocity dispersion (change in velocity with frequency) and attenuation are dependent on viscosity and permeability and the relaxation peak shifts toward low or high frequency by decreasing or increasing the fluid mobility respectively. This behavior is predicted by many theories except Biot's dispersion/attenuation mechanism. Fluid distribution does not make much difference in attenuation and velocity for the length of sample used in these experiments. A layer of gas on top of fluid is detected by the fluid for all frequencies. The fluid is always in relaxed state and this causes loss in energy even if the rock is saturated with brine and has only a layer of gas on top. Clays influence velocity and attenuation. Due to chemical interaction with water clays swell and change the properties of rock. In order to avoid such influences brine was used instead of water. These results help to understand the different proposed attenuation/dispersion mechanisms. One of the potential applications would be using attenuation to predict changes in saturation or viscosity in case of thermal enhanced

oil recovery. It can also be used to detect zones of high permeability. Using attenuation as a seismic tool would be very favorable in a time lapse sense because most of other sources of amplitude loss remain constant.

TABLE OF CONTENTS

LIST OF FIGURES

LIST OF TABLES

ACKNOWLEDGEMENTS

I started working on the seismic attenuation topic as part of my first comprehensive project and got so interested that I converted it into my Master's thesis. My advisor Dr. Michael Batzle has been a wonderful guide and a great source of inspiration. His ideas and guidance has helped me through this research and my studies at CSM. I am deeply grateful to him for his trust in me.

I would like to acknowledge the FLUIDS and ITF consortia for funding the research and providing the rock samples for analysis. I would also like to thank the members of my committee Dr. John Scales and Dr. Richard Christiansen for their guidance, help and support. Also, I sincerely thank Dr. Ken Larner for helping me out at difficult times, Dr. Gary Olhoeft for enlightening me on the subject of attenuation, Dr. Tom Davis for all his help and encouragement.

I feel very fortunate to have had such wonderful fellow students in the Geophysics department. I would specially like to thank Ronny Hofmann for allowing me to share his office space and for all the deep insightful thoughts and discussions I have had with him. My special thanks to my friends Pawan, Arvind, Raj, Kosu, Sudipta, Charlie and Catherine for bearing with me and for all the wonderful moments that I have shared with them.

Last but not the least I would like to thank all my dear friends who are scattered everywhere on this planet and my family to whom I owe everything.

To my mother

Chapter 1

INTRODUCTION

Seismic and acoustic methods are among the primary tools in oil exploration. These methods also find increasing use in reservoir delineation and monitoring recovery processes. Sonic logs give us the detailed vertical measure of the in-situ rock properties at 10^4 Hz frequency range. Seismic data gives us the horizontal resolution and its interpretation helps in locating and analyzing geological features, including hydrocarbon accumulation. It is important to calibrate these techniques and also understand the fundamentals of wave propagation at different frequency-amplitude ranges.

Compressional and shear velocities have been measured in the laboratory for a number of years but most of these measurements are done at ultrasonic frequencies. Alternatively, low-frequency moduli can be derived from stress strain measurements, but these macroscopic strains levels are far outside the range of seismic or logging amplitude. This is illustrated in Figure 1.1. Exploration seismic data is usually collected between 10-100 Hz and at strain amplitude around 10^{-7} [Wideman and Major, 1967]. Sonic well logs are in the same amplitude range but with frequencies in tens of KHz range. Ultrasonic measurements are easily carried in laboratory but they lie in megahertz frequency range. Resonance techniques are very useful in measuring velocity dispersion and attenuation. For small samples they can go to the KHz range. For larger samples it can go down to the lower KHz range. And resonance is the only

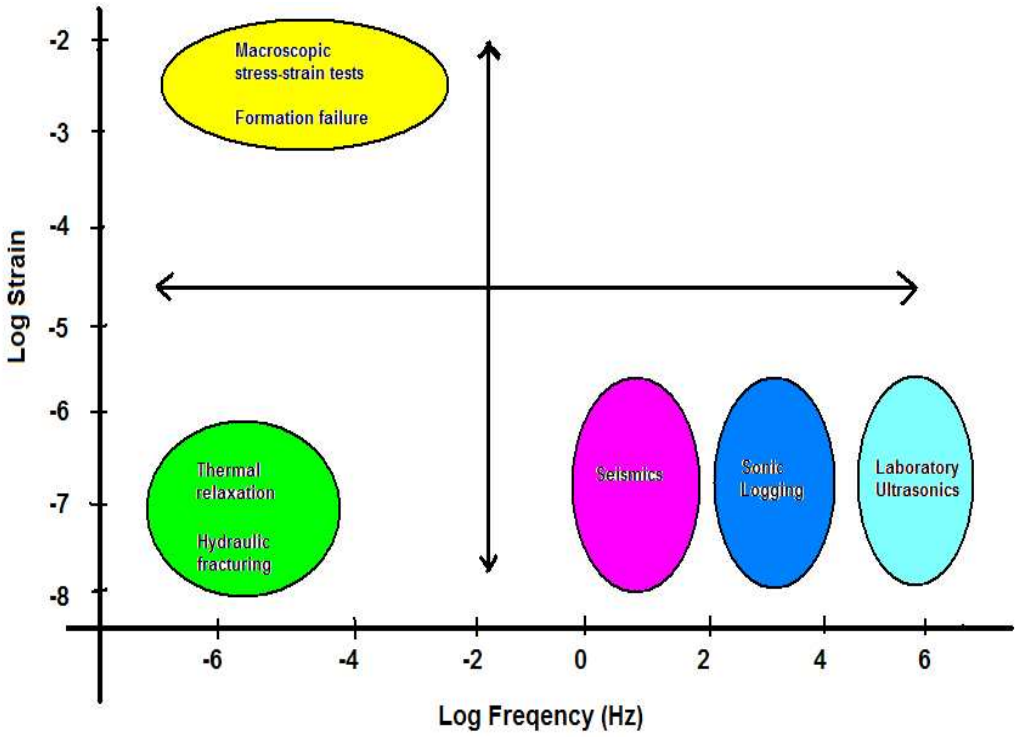

FIG. 1.1. Frequency and amplitude relationship among various measurement techniques as well as *in-situ* processes. Note that most alternative measures of elastic properties are outside the seismic range.

technique that gives an unambiguous measurement of intrinsic Q since the sample is decoupled from the apparatus. When we try to compare these techniques we will get systematic errors because of the reasons mentioned above.

The other fundamental seismic property of rocks, attenuation (inverse of quality factor Q) is poorly understood because of the lack of data. Compressional and shear waves propagating through a *visco-elastic* medium loose a part of their energy in the form of heat. This process is called intrinsic-attenuation and the loss in en-

ergy or amplitude is in excess of the losses due to spherical divergence, scattering, transmission and diffraction. Several laboratory measurements of attenuation on rock samples under varying pressure, temperature, strain amplitudes, frequency and saturation conditions have been made [Wyllie, Gardner and Gregory, 1962; Winkler, Nur and Gladwin, 1978; Winkler and Nur,1979; Spencer, 1981]. These data suffer from the same problems as with velocity measurements. Attenuation is strongly dependent on frequency and strain amplitude. Different attenuation mechanisms operate at different location in amplitude-frequency space shown in Figure 1.1. Thus attenuation measured ultrasonically may be totally unrelated to the one measured at seismic frequency band. This is the motivation behind doing low-frequency, low-amplitude seismic attenuation and velocity measurements.

Taner and Sheriff [1976] mention the use of *instantaneous frequency* and *'weighted averaged frequency'* as seismic attributes. In several field examples they show that there is a sharp shift toward low frequencies below the gas reservoir indicating loss of high frequency in the gas reservoirs. Their observation was emperical and at that time they had no explanation for these observations. Castagna and Sun [2003] discuss the concept of Instantaneous Spectrum Analysis (ISA) and show that it can be used as a direct hydrocarbon indicator. In spectrally decomposed seismic data they claim to observe low-frequency shadows below gas reservoir. They argue that these shadows are not due to attenuation but could be produced due to processing of the data [Ebrom,1996]. Recently Goloshubin et al. [2000, 2001, 2002] have tried to explain the above mentioned low-frequency shadows using 'frictional-viscous' theoretical modeling and laboratory experiments. Real seismic and VSP examples are also illustrated to strengthen their explanation. Their explanation has serious flaws because they do

not care about the attenuation mechanism and they assume that attenuation mechanisms can be scaled. The frequency range used by them is in the order of KHz and the dispersion/attenuation mechanism in this range is totally different from the seismic frequency range. Richard Gibson has tried to combine the effect of tuning, attenuation and dispersion of seismic waves to explain low-frequency anomalies from thin layers. He has used the same frequency dependent Q as used by Goloshubin et al. which contradicts a lot of laboratory measurements. Thus it becomes very important to understand the attenuation mechanism and how it is effected by rock properties (porosity, permeability), fluid properties, fluid distribution and presence of clay before we try to explain the anomalies discussed above and try to use these anomalies as direct hydrocarbon indicator.

There are a number of theories which explain attenuation mechanism under different physical conditions. Some of the theories contradict each other and it is important to examine these with real data. It is also important to find out which one is more applicable under a given condition. The main effort of my thesis work has been to come up with the best acquisition system for extracting attenuation at seismic frequencies and use these measurements to better understand the effect of fluids on attenuation and dispersion. A number of rock samples were measured and definite conclusions are made about the effect of pressure, fluid saturation, distribution, boundary conditions and clays. We are still in the process of understanding the different attenuation/dispersion mechanisms. The use of absolute attenuation may not be possible in near future but it can be a very good tool for time-lapse monitoring processes and in case of monitoring a water flood it can be a better tool than velocity changes because of the problems with partial saturation. Ken Hedlin [2001] for his

Master's thesis investigated the potential of attenuation of seismic waves to monitor steam flood. He modeled attenuation effect in seismic and came to the conclusion that for heavy oil samples the seismic frequencies act as ultrasonic frequencies and the peak relaxation frequency is less than the seismic frequency range. Similar measurement done on the Uvalde carbonate sample which is saturated with heavy oil showed similar results.

The concept of AVO was introduced long ago (1950's), but it took a while before the industry actually started using it as a Direct Hydrocarbon Indicator (DHI). Recently there has been an increase in the effort to understand attenuation and use it as a seismic attribute. In my view we need to put more effort on understanding it rather than trying to extract and use it from seismic data because without a proper understanding it would be a total waste of effort, time and money.

Chapter 2

THEORY

Observed seismic waves do not travel with a simple elastic propagation. Amplitudes are lost both in distance and time. The loss in amplitude is due to scattering, diffraction, transmission and spherical divergence. When the material is not purely elastic there is a loss in excess to the above mechanisms. This phenomena is called intrinsic attenuation and is a characteristic of a linear viscoelastic material. There are three conditions which define ideal elastic behavior [Nowick and Berry, 1972]. These are: 1) Strain response to each stress value has unique equilibrium value. 2) equilibrium response is reached instantaneously 3) response is linear. If conditions 1 and 2 are removed then we have linear viscoelastic behavior. For linear viscoelastic systems there is a specific relation between modulus or velocity dispersion and attenuation. If the dispersion is characterized at all frequencies then attenuation is known for all frequencies and vice versa (Kramers-Kronig relations between velocity dispersion and Q). Kramers-Kronig relations allows to put some constraints on the material behavior. A low and high frequency limit of the modulus is obtained which are real quantities and the frequency dependent modulus is defined using these limiting values. Then the attenuation is computed using the real and imaginary part of the modulus [Cole-Cole, 1941; Futterman, 1962].

In a linear viscoelastic medium, the stress and strain are related via a complex modulus. This complex modulus introduces a phase shift between applied stress and observed strain. This effect is shown in Figure 2.1.

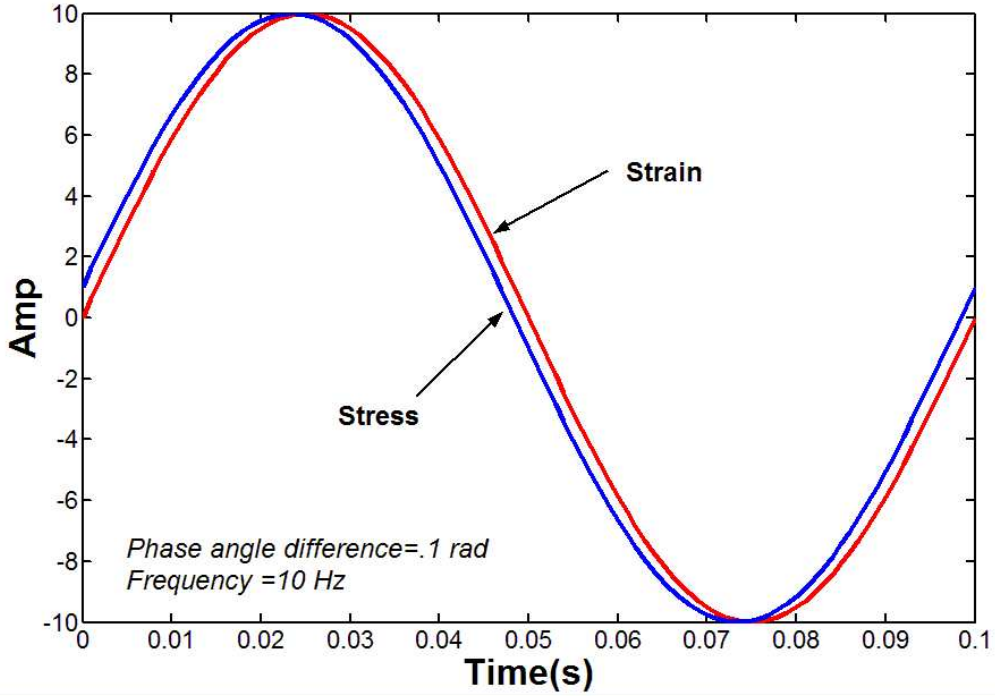

FIG. 2.1. Phase lag between the applied stress and observed strain in a linear visco-elastic medium. The phase lag is 0.1 radians for this illustration and the driving frequency is 10 Hz.

2.1 Measures of attenuation

One of the issues with attenuation is that there are several different methods and techniques to estimate and describe attenuation. The attenuative properties of rock are specified by a wide range of measures. The most commonly used measure is *alpha* (α) or plane-wave attenuation coefficient. This gives the exponential decay in the amplitude of a plane wave. For a plane wave propagating in an elastic homogeneous

medium the amplitude is given by:

$$A(x,t) = A_0 e^{i(kx-\omega t)} \tag{2.1}$$

where, A_0 is the maximum amplitude, k is the wavenumber and ω is the frequency. All the three quantities are real. If we assume that the frequency or the wavenumber is complex we can introduce attenuation. In case of a complex wavenumber,

$$k = k_r + i\alpha \tag{2.2}$$

where k_r is the real part of the wavenumber and α is the plane wave attenuation coefficient and has the units of inverse length, the plane wave equation becomes,

$$A(x,t) = A_0 e^{-\alpha x} e^{i(k_r x-\omega t)} \tag{2.3}$$

Using this definition of attenuation we can define α in terms of the amplitude of the wave at two different positions x_1 and x_2 as:

$$\alpha = \frac{1}{(x_2 - x_1)} \ln \left[\frac{A(x_1)}{A(x_2)}\right] \tag{2.4}$$

and the units are nepers/unit length. Alternatively α can be written as :

$$\alpha = \frac{1}{(x_2 - x_1)} 20 \log \left[\frac{A(x_1)}{A(x_2)}\right] \tag{2.5}$$

in units of dB/unit length. The other common measure of attenuation is the *Logarithmic decrement* (δ) and is defined for an oscillating system in free decay and follows from equation 2.4:

$$\delta = \ln\left[\frac{A_1}{A_2}\right] = \alpha\lambda = \frac{\alpha v}{f} \tag{2.6}$$

where, A_1 and A_2 are the amplitude at two consecutive cycles and λ is the wavelength of the cycle with velocity v and frequency f. Another measure of attenuation is called Q or *Quality factor* and is used commonly. O'Connell and Budiansky [1977] have discussed in detail the various definitions of the *Quality factor*. This internal loss in energy gives the intrinsic Q value and is in excess to all other losses encountered during wave propagation as discussed earlier. Each of these loss parameters (α, Q, δ) can be related to each other. The relationship is neatly derived in literature [White, 1983; Toksoz and Johnston, 1981]. For compressional wave the relations are:

$$\alpha_p = \frac{|\omega|}{2QV_p} = \frac{|\omega|\,\delta_p}{2\pi V_p} \tag{2.7}$$

$$\frac{2\alpha_p V_p}{|\omega|} = \frac{1}{Q_p} = \frac{\delta_p}{\pi} \tag{2.8}$$

$$(\frac{\Delta f}{f})_p = (\frac{\delta}{\pi})_p \tag{2.9}$$

where, V_P is the compressional velocity.

The real modulus $M^R = \lambda + 2\nu$ describes the compressional velocity in a medium [Gassmann, 1951a]. If the modulus becomes a complex quantity M^C then the material becomes attenuative, where M^*=Im $[M^C]$ and M=Re $[M^C]$. If we assume that the medium is nearly elastic [White, 1968] such that $M^* << M$ then it is justified to use

the following approximations:

$$tan^{-1}(\frac{M^*}{M}) = \frac{M^*}{M} \tag{2.10}$$

$$(1 + i\frac{M^*}{M})^{-1} = 1 - i\frac{M^*}{M} = e^{-i\frac{M^*}{M}} \tag{2.11}$$

The relation between stress and strain in a nearly elastic solid for simple extension is given as:

$$P_{xx} = (M + i\,\mathrm{sgn}\,\omega M^*)E_{xx} \tag{2.12}$$

where, P_{xx} is the stress in x direction, E_{xx} is the strain in x direction and M is defined as above. With the definition $\frac{1}{Q} = \frac{M^*}{M} = \tan\,\phi \sim \phi$ [White, 1965]
where ϕ is the phase angle between applied stress and observed strain, and using equations 2.10, 2.11 and 2.12 the expression for stress and strain in simple extension is given as:

$$P_{xx}e^{i\omega t} = ME_{xx}e^{i(\omega t + \phi\,\mathrm{sgn}\,\omega)} \tag{2.13}$$

which means that in a near-elastic solid when a stress is applied the resulting strain has the magnitude proportional to the real part of the modulus and the phase angle between the stress and strain is given by the ratio of imaginary to real part of the modulus. The same rule applies for shear stress and shear strains.
A consequence of this phase angle is a slightly elliptical stress-strain diagram. The area of the ellipse gives the energy expended during a stress-strain cycle. The loss in energy divided by the maximum stored energy is also a parameter for characterizing an attenuative medium. This is also the definition of the *Quality factor*. Thus intrinsic

Q can be defined as:

$$Q = \frac{\omega E}{-dE/dt} = \frac{2\pi W}{\Delta W} \tag{2.14}$$

where, E is the instantaneous energy in the system and dE/dt is the rate of energy loss, W is the maximum energy stored during one stress-strain cycle and ΔW is the energy loss per cycle of oscillation. This is the reason why even for a constant Q value the high frequencies have more energy loss compared to the low-frequencies as they have a greater number of oscillations for a given distance covered by the wave.
An additional dynamic measurement Q is defined in terms of resonance-peak bandwidth of a resonating sample:

$$Q = \frac{f_r}{\Delta f} \quad for\ Q >> 1 \tag{2.15}$$

where, Δf is the frequency width between the half power points about the resonance peak f_r.

2.2 Modes of attenuation

Attenuation can be measured in different ways both in the laboratory and in the field. Throughout this thesis I will use 1/Q for attenuation. I have defined Q in terms of complex moduli, but since even for an isotropic medium there are several different moduli, we expect several types of Q. There are different modes of wave propagation such as *compressional*, *shear* and *Young's* mode. If we measure the extensional stress-strain phase lag then Q_E^{-1} describes the visco-elastic behavior of the Young's modulus. The bulk loss Q_K^{-1} can be obtained from hydrostatic stress and dilational strain. Compressional and shear wave propagation provide Q_P^{-1} and Q_S^{-1}

respectively. All these different attenuation (Q^{-1}) values are related to each other. These relations are derived from the well established relations between the various moduli. White [1965] gives a table of relations among complex moduli for near-elastic solids. Using these relations and the fact that $Q_M^{-1} = \frac{M_I}{M_R}$ where, M stands for the modulus of the mode of propagation, M_I=Im [M] and M_R=Re [M], the relations between the various modes of attenuation can be derived (see Appendix A). The final equations relating the different stress state Q values are given below [Winkler and Nur, 1979]:

$$\frac{(1-\nu)(1-2\nu)}{Q_P} = \frac{(1+\nu)}{Q_E} - \frac{2\nu(2-\nu)}{Q_S} \tag{2.16}$$

$$\frac{3}{Q_E} = \frac{(1-2\nu)}{Q_K} + \frac{2(1+\nu)}{Q_s} \tag{2.17}$$

$$\frac{(1+\nu)}{Q_K} = \frac{3(1-\nu)}{Q_P} - \frac{2(1-2\nu)}{Q_S} \tag{2.18}$$

where Q_P, Q_S, Q_K and Q_E stand for *compressional*, *shear*, *bulk* and *Young's* attenuation parameters respectively. ν is the Poisson's ratio which is measured either directly or can be computed from the compressional and shear velocities by using the relation :

$$\nu = \frac{V_P^2 - 2V_S^2}{2(V_P^2 - V_S^2)} \tag{2.19}$$

2.3 Proposed attenuation mechanisms and theories

Different measurement techniques are not the only problem (feature) associated with quantifying attenuation. There are many different proposed mechanisms of attenuation in literature. At any given physical state of the rock a particular mechanism

may be the important contributor to the intrinsic attenuation. It may also be possible that different mechanisms operate at the same time and it can be difficult to differentiate among them or quantify their individual contribution. It is interesting to understand the similarities and differences between some of the important proposed attenuation mechanisms.

2.3.1 Friction at grain contacts

A *Sphere pack model* of granular rocks is a well known model used to describe the skeleton of a rock. This model consists of rounded grains in contact, with varying degree of cementation. When a load is applied to this rock the spherical grains of unequal radii come in contact with each other. The area of contact can be cemented to various degrees and this controls the compaction of the rock. Such a mathematical model allows us to compute the average elastic constants. When a wave propagates through such a medium the grains slide along the contact boundary. In such a situation the stress-strain curve should be a closed curve independent of strain rate [White,1983]. The assumption is that the *tangential* and *normal* stresses at the point of contact are governed by the Coulomb friction. When sliding occurs the two components of friction are related as:

$$p_T = K_d p_N \tag{2.20}$$

where, p_T is tangential stress, p_N is normal stress at the point of contact and K_d is the coefficient of friction. The force-displacement curve is a hysteresis loop and the area of the loop gives the loss in energy. The fractional energy loss per cycle for a shear waves along an axis of a cubic array of spheres, is:

$$\left(\frac{\Delta W}{W}\right) = \frac{4\Delta G'}{9K_d G} \tag{2.21}$$

where, G is the normal force by which the rock is pressed and $\Delta G'$ is the maximum tangential force. The attenuation is proportional to frequency with reference to equation 2.7. However the attenuation is also proportional to strain amplitude [Mavko and Nur, 1979]. The strain-amplitudes in seismic wave propagation is of the order of 10^{-7} [Wideman and Major, 1967] and thus should not be a significant contributor to the overall attenuation.

Movement along elliptical crack surfaces are also a source of frictional attenuation in seismic waves. Faces of elliptical cracks can slide, causing loss in energy. An increase in load across the crack can close the cracks and thus reduce sliding and cause a reduction in attenuation. Attenuation is found to be independent of amplitude and depends on such parameters as crack size, crack orientation and crack density [Walsh, 1966]. Winkler and Nur [1979] made some measurements on sandstone rods and concluded that Q^{-1} is independent of amplitude for strain level less than 10^{-6}, yet increases non-linearly for higher values of strain. Recent work by Abeele et al. [2002] suggest that for strains less than 10^{-6} non-linearity in Q^{-1} is observed. But again the magnitude of non-linearity decreases with decreasing strain level and becomes insignificant at strain values less than 10^{-7}. In conclusion we can say that for strains observed in seismic exploration, sliding friction probably is not responsible for the observed Q^{-1} values.

Attenuation for fully or partially-saturated rocks is higher than for dry rocks and depends upon the degree of saturation, fluid type and frequency in complicated ways

[Tittmann et al., 1981; Clark et al., 1980]. In the sections to follow we will discuss the different theories which try to explain the attenuation mechanism based on fluid flow.

2.3.2 Biot theory

Biot developed a theory to describe the wave propagation in a fluid saturated rock [Biot, 1956a,b]. The rock consists of a matrix of solid grains mixed with a pore space. Pore spaces are typically interconnected and permit fluid to flow through the rock. The pore spaces could be filled with fluids and they influence the acoustic wave velocity and the attenuation. If the fluid is viscous there is frictional force between the pore boundary and the fluid as propagating elastic waves cause relative motion between the fluid and pore. This frictional force was the proposed attenuation mechanism by Biot. Poiseuille flow is assumed below a characteristic frequency which is governed by the kinematic viscosity of the fluid and the pore size. The characteristic angular frequency is given as [Biot, 1956a]:

$$\omega_c = \frac{\mu\phi}{k\rho_f} \tag{2.22}$$

where, k is the permeability ρ_f is the density of the fluid, μ is the fluid viscosity and ϕ is the rock porosity.

Gassmann's [1951] relations are among the most popular for describing the elastic properties of porous materials. The Biot theory was an improvement over this theory. Gassmann did not consider relative motion between the fluid and the rock and thus could not account for dispersion/attenuation. His equations break down at high frequencies and he gave no indication of this limiting frequency. The Biot low-frequency limiting velocities are the same as predicted by Gassmann.

The material is described by four non-dimensional parameters and a characteristic frequency. For frequency above the characteristic frequency a different approach is used to describe velocity dispersion and attenuation. Poiseuille flow breaks down above the characteristic frequency and a complex viscosity correction factor is applied to consider the oscillatory motion of fluid between the parallel walls or circular tubes [Biot, 1956b]. Fluid inertia is the dominant cause of energy loss in the high frequency regime. In the high frequency limiting case we have two dilatational waves and one shear wave. The two P-waves are called the waves of the first and second kind or fast and slow P-waves. The second dilatational wave is diffusive in nature and is heavily attenuated and thus is not observed in real situations very often. The cross product of the velocities in the fluid and the solid gives rise to a mass coupling term. Biot's theory covers a wide range of frequency but when the wavelengths are of the order of the pore size, then scattering dominates and a different treatment to the problem is required.

It is useful to note down the assumptions and drawbacks of Biot's theory. The assumptions made are [Biot, 1956a]:

1. The rock is homogeneous and isotropic.
2. The rock and fluid densities are comparable.
3. Thermoelastic effects are disregarded.
4. Pore sizes are concentrated around an average value.
5. Shear modulus unaffected by fluids.

The first assumption is made in order to make the formulations simple and is a very common assumption. The second assumption limits the use of this theory in case

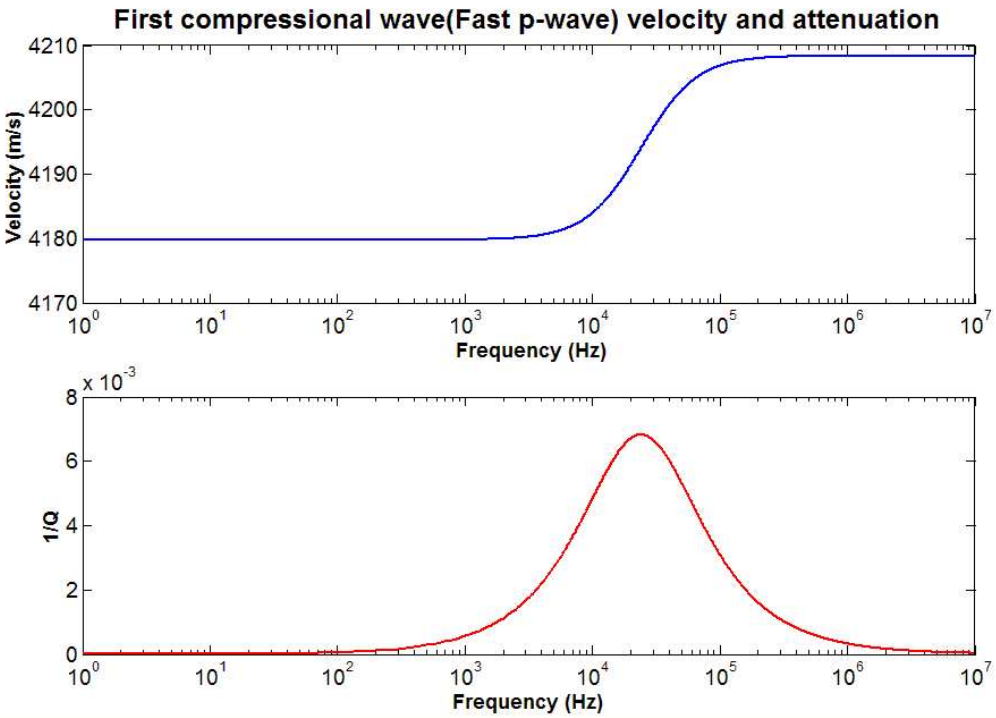

FIG. 2.2. Fast P-wave (Biot): Porosity=19%, permeability=400 mD, viscosity=.01 poise, coupling mass density=420 kg/m^3 (from Mavko-Jizba squirt theory), matrix density=2125 kg/m^3, fluid density=1200 kg/m^3.

where rock and fluid densities are not comparable. The third assumption disregards any thermal contribution to the energy loss. Assumption four discounts any extreme distribution of pore sizes and cracks, which is common in nature. Assumption five is a very well accepted fact. Despite all these assumptions, the predicted Biot 'slow' P-wave has been observed in the laboratory samples [Plona, 1980]. Figure 2.2 shows the predicted velocity dispersion and the attenuation(1/Q) values for the fast P-wave. As can be seen in the figure the velocity dispersion is not very large, less than a percent. Also the 1/Q values are very small. Biot theory underestimates the

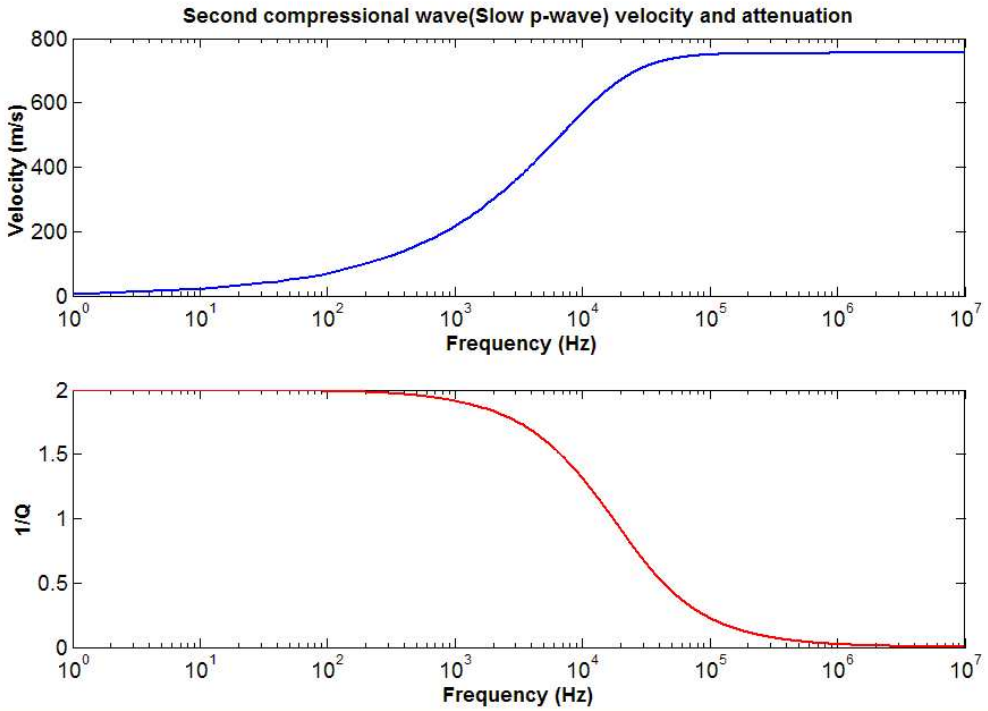

FIG. 2.3. Slow P-wave (Biot): Porosity=19%, permeability=400 mD, viscosity=.01 poise, coupling mass density=420 kg/m^3, matrix density=2125 kg/m^3, fluid density=1200 kg/m^3.

dispersion and attenuation observed in the rock fluid systems. Figure 2.3 shows the slow P-wave velocity and attenuation. The slow wave has very low velocity and there is no dispersion above 10^5 Hz. Also, the attenuation is very small in this range and it increases to a value of 2 at low-frequencies which is huge attenuation and has been mentioned by other people too.

When the pore-fluid viscosity is increased the Biot attenuation peak moves toward higher frequencies (Figure 2.4). Biot theory predicts solid/fluid coupling at low-frequencies and decoupling at higher frequencies. However in some measurements

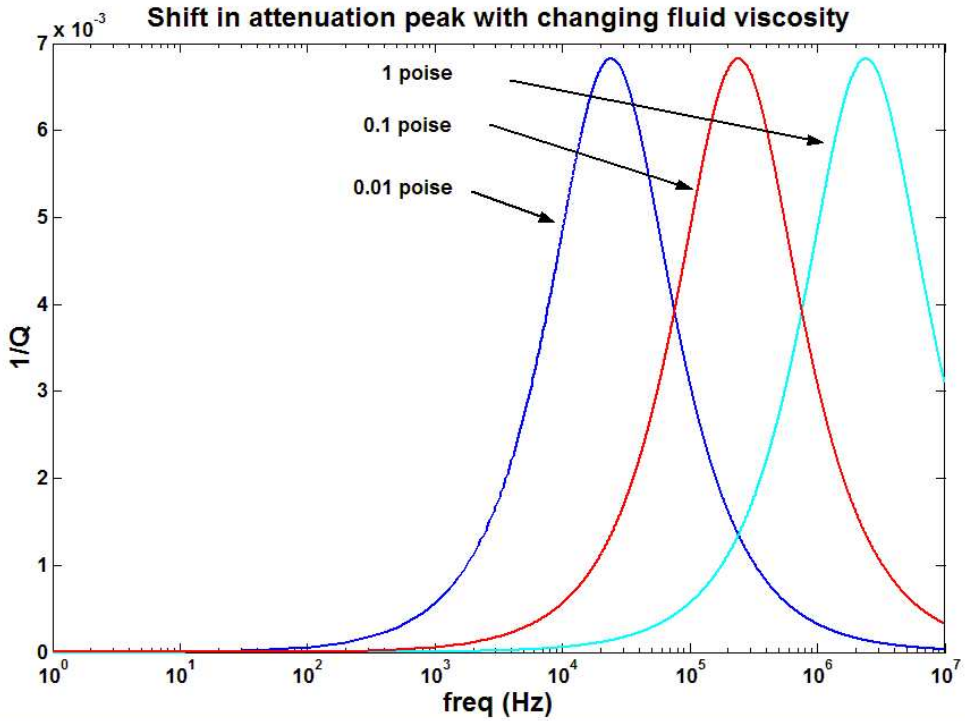

FIG. 2.4. Shift in attenuation peak with changing viscosity predicted by Biot's theory. Porosity=19%, permeability=400 mD, coupling mass density=420 kg/m^3, matrix density=2125 kg/m^3, fluid density=1200 kg/m^3. Note that with higher viscosity, the peak shifts to higher frequencies.

(including my own) it is observed that with increase in viscosity the attenuation peak shifts toward low-frequencies (see Chapter 4).

2.3.3 Squirt flow

In the Biot mechanism the fluid interacts with the the oscillating solid through viscous friction and inertial coupling. In the squirt flow mechanism the passing acoustic/seismic wave causes squirting between pore fluid and gas pocket and also fluid in the soft pore space 'squirt' out to adjacent non-compressible pores [O'Connell and

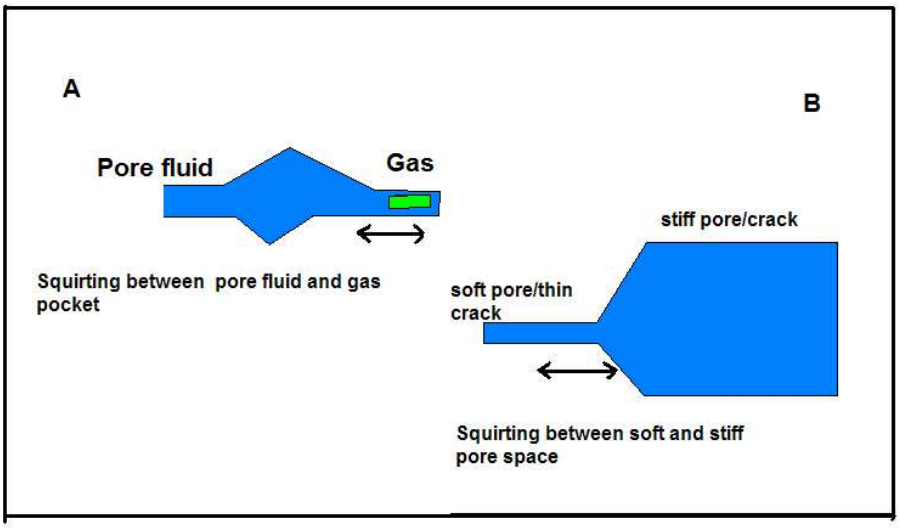

FIG. 2.5. The Squirt model: (A) Squirting flow in saturated rock with small amount of compressible gas (B) squirt in fully saturated rock between the compliant soft pores to non-compliant stiff pores.

Budiansky, 1977]. Both the squirting mechanisms are shown in figure 2.5.

Mavko and Nur [1979] presented the model that describes the squirt mechanism in partially saturated rocks. In cracks or pores with small aspect ratio $\left(\frac{width}{length}\right)$ if a small amount of gaseous phase is present then the fluid can flow freely when the pore is compressed. They showed that the resulting attenuation was much higher than that predicted by Biot. The aspect ratio of the pores/cracks play an important role and the pore geometry is not that significant factor in their analysis. Rocks with compliant pores are more sensitive to fluids and can easily deform under compressional/shear stress. Round and spherical pores have less compliance and do not respond to pressure or fluids. The local heterogeneity in the pore causes large fluid flow which is the source

of attenuation.

In case of full saturation two separate approaches were made to describe squirt induced attenuation and velocity dispersion. In the first approach Dvorkin and Nur [1993] introduced a 'unified model' with squirt and Biot mechanism. They argued that the Biot mechanism and squirt are coupled via fluid mass balance and occur in a rock simultaneously. They proposed a Biot/Squirt (BISQ) theory in which the motion of fluid parallel (Biot) to the P-wave propagation and perpendicular (Squirt) causes velocity dispersion and attenuation (figure 2.6).

In this approach they were able to relate the attenuation and dispersion to the macroscopic rock and fluid properties as opposed to pore scale description of partial squirt phenomena. They use characteristic squirt flow length to relate the dynamic poroelastic behavior which is assumed to be independent of frequency and is an inherent rock property. There are certain assumptions made :

1. Mineral matrix is homogeneous and isotropic.
2. Permeability is same in all directions.
3. There is a small amount of high compressibility gas present in the pore spaces.
4. The squirt flow length is independent of rock/fluid properties and frequency.

The first assumption is typical. The second assumption excludes any rock with permeability anisotropy which is very common in rocks. The third assumption is very important as it means that the rock is not fully saturated with a single fluid phase. This is the reason why the low-frequency limit of Biot/squirt predicted velocity is smaller than the Biot/Gassmann predicted velocity for fully saturated rock. The last assumption has been defended by the authors by saying that the squirt flow length

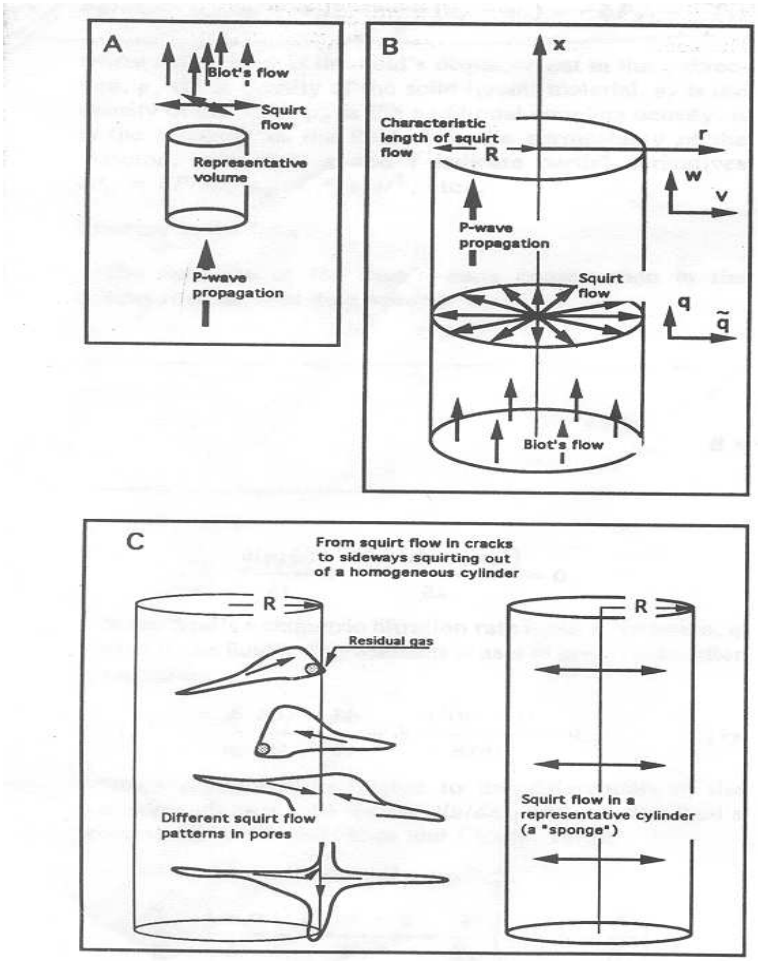

FIG. 2.6. The BISQ model: (A) Biot's flow and squirt flow in a rock due to seismic excitation (B) A cylindrical representative volume of the rock (C) From squirt flow in cracks to the sponge model (from Dvorkin and Nur, 1993).

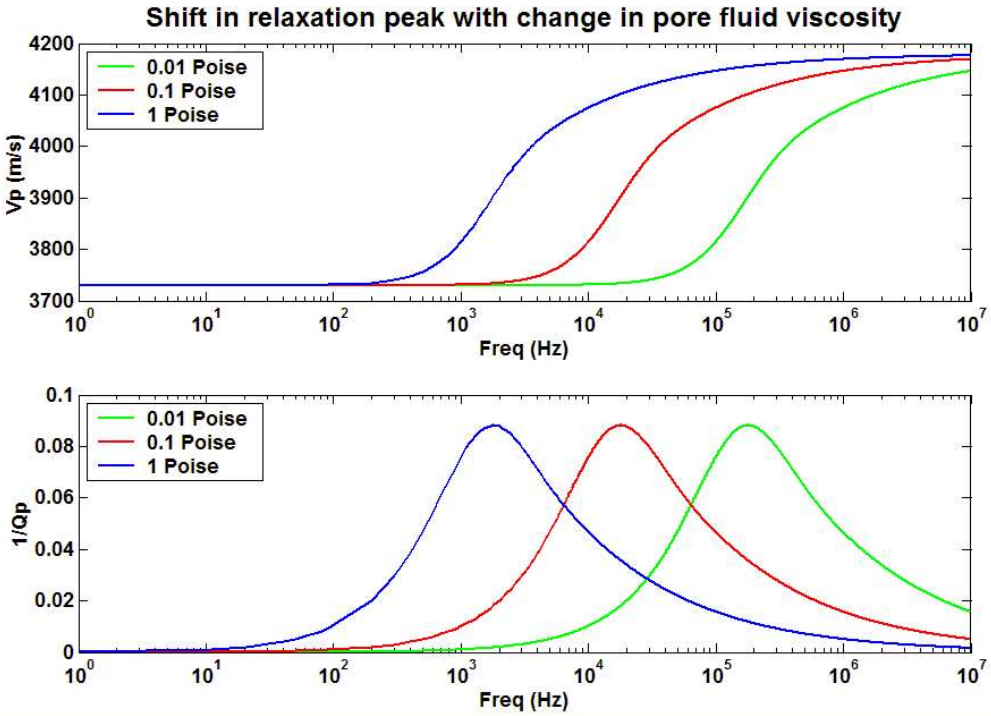

FIG. 2.7. The Biot/squirt model: Decrease in relaxation frequency as the viscosity of the pore fluid increases. Porosity=19%, permeability=400 mD, coupling mass density=420 kg/m^3, matrix density=2125 kg/m^3, fluid density=1200 kg/m^3, squirt length=5 mm.

can be computed by matching the data with their predicted results of either velocity dispersion or attenuation. The BISQ model is a more complete version of Biot and involves simultaneous effects of both Biot and Squirt mechanisms. The low-frequency assumption is a squirt mechanism and in high frequency both mechanisms operate. It predicts higher velocity dispersion and attenuation as is observed in most rocks. Also it predicts a shift in relaxation to lower frequency as the fluid viscosity increases (Figure 2.7). There is also a shift in relaxation to higher frequency as the permeability increases which is observed in real rocks.

Dvorkin, Mavko and Nur [1995] described the second squirt-flow mechanism of solid/fluid interaction through macroscopic fluid/solid parameters. The previous works on squirt flow involved partially saturated rocks and nearly saturated rock with small amount of compressible gas. In this approach fully saturated rock is considered and the fluids quirt from compliant pores (thin cracks/flat pores) to non-compliant round pores and to pores of different geometry (figure 2.5). At high pressures the velocity dispersion and attenuation is small and the reason is that the compliant pores close at high pressures. The approach is to use a modified solid phase which includes the rock matrix and the compliant pores and extract the information of the compliant pores from high pressure velocity data. 1-D radial flow is modeled using fluid mass conservation equations, pore pressure, poroelastic (Biot) relations among strains and Darcy's law. Some of the assumptions involved are :

1. Shear induced pore pressure is determined by the normal (to the pore wall) component of the shear stress.

2. The effect of this normal component is identical to bulk compression.

Both these assumptions are made to compute the shear modulus of the modified frame and have been discussed in Mavko and Jizba [1991] paper. The improvement in this approach is that all of the macroscopic parameters are unified in one expression R^2/κ, where R is the characteristic squirt flow length and κ is the diffusivity of the soft pores. But again it is assumed that this expression is independent of frequency and is found by matching velocity/attenuation data. One of the drawbacks is that numerous parameters have to be estimated or measured in order to compute dispersion/attenuation like dry velocities at high differential pressure, solid phase density and compressibility.

2.3.4 White's Gas Pocket model

White [1975] proposed the *gas pocket model* to describe attenuation and dispersion in partially saturated rocks. This theory is very similar to squirt mechanism. In this model the rock is assumed to be partially saturated with a liquid and the rest of the rock has pockets of gas. Compressional wave produces pressure gradients in the fluid. The gradient is very high at the boundary of liquid and gas causing fluid motion and thus acts as a local zone of high energy loss. White uses some idealized geometry to mathematically model his theory. Some of the assumptions are :

1. Skeleton is uniform.
2. The gas pockets are spherical and uniformly distributed in cubic lattice fashion (figure 2.8).
3. The gas acts a complete pressure release.

All the three assumptions are made in order to simplify the computations. The requirement that the gas zone should be a complete pressure release is significant as in some of the heavier gases or high pore pressures can not be modeled using this theory. This theory exhibits a relaxation phenomena and the characteristic time is dependent on the size of the gas pocket and the distance between them. When the frequency of the compressional wave is small compared to this characteristic time then there is complete pressure release and the bulk modulus is close to dry modulus with no dispersion. At high frequency there is no fluid flow and the velocity is high and 1/Q is small. Between these two frequency limits we have attenuation and velocity dispersion. This model has been successful in predicting the change in velocity with saturation [Gist, 1994; Dutta and Odé, 1979]. It is important to note that the

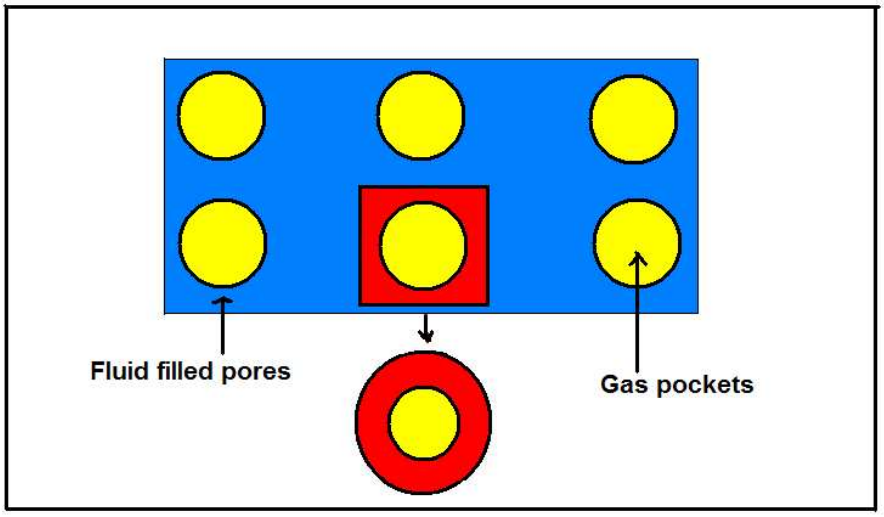

FIG. 2.8. White's [1975] gas pocket model: Porous rock with mixed saturation. Gas pockets present in cubic lattice fashion and the intermediate spaces are filled with a liquid. A typical volume considered for calculation is a pair of concentric circles shown in the bottom.

shear-wave attenuation and velocity are not affected in this model.

All these theories have some similarities. The first important conclusion is that fluid flow is the most important reason for the observed attenuation/dispersion in saturated rock [Tittmann, 1977; Clark, 1980]. In Biot's theory the energy loss is due to relative fluid flow causing shearing loss and inertial coupling. In squirt flow mechanism the pressure gradient in the fluid is created due to propagating seismic waves. The gas pockets act as a release in pressure for partially saturated case and allow more flow which explains higher attenuation values compared to Biot. In fully

saturated rocks fluids flow from compliant pores to stiff pores. In White's [1975] model, fluid flow occurs along the boundary of gas pockets and liquid. The difference between White's model and squirt is that squirt assumes fluid flow at pore dimensions whereas in White's model several pore volumes are saturated with gas pockets. At low-frequencies Q^{-1} is proportional to ω in both Biot and squirt models. At high frequencies Biot Q^{-1} varies as $\omega^{-1/2}$ whereas squirt varies as $\omega^{-3/2}$. White's low-frequency Q^{-1} also depends on ω whereas the high frequency Q^{-1} depends on ω^{-1}. All of these theories have some kind of characteristic frequency where the dispersion is maximum and the Q^{-1} peaks. Biot characteristic frequency has already been defined (equation 2.22). In the squirt flow mechanism the viscoelastic behavior is defined by a single non-dimensional parameter $\omega R^2/\kappa$ where:

1. R is the characteristic squirt flow length (in mm).
2. $\kappa = \frac{kF}{\mu\phi}$.
3. $F = (\frac{1}{\rho_f c_0^2} + \frac{1}{\phi Q})^{-1}$.
4. ϕ= porosity and k is permeability.
5. ρ_f is fluid density and c_0 is compressional velocity in fluid and μ is fluid viscosity

The dimension of κ/R^2 is of inverse frequency. In White's model the characteristic frequency is called the reference frequency and is given as:

$$2\kappa k_E/\eta b^2 \tag{2.23}$$

where, κ is permeability, k_E is the bulk modulus of the fluid, η is viscosity and b is the radius of outer sphere. In conclusion we can say that these theories are related

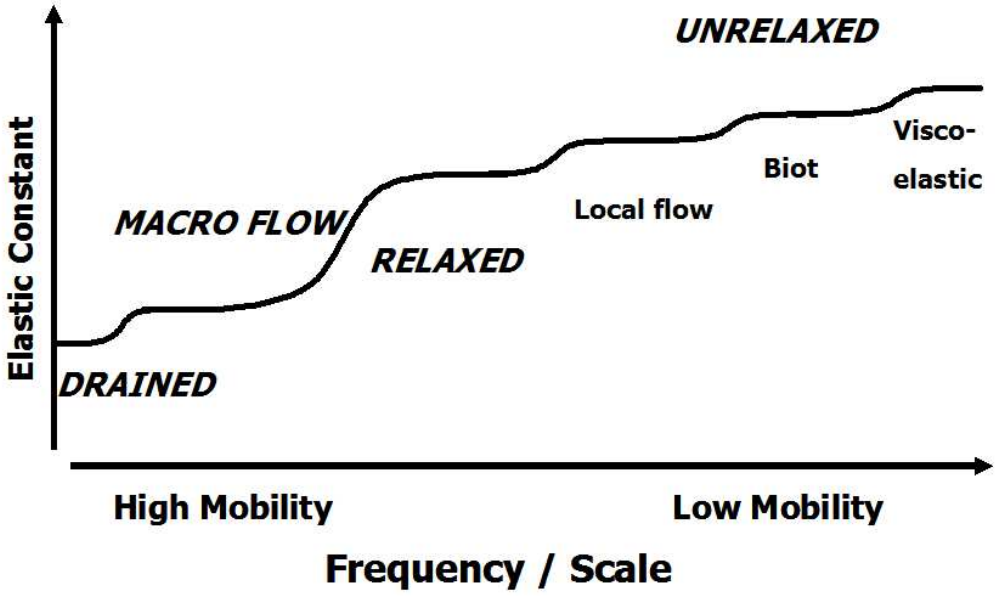

FIG. 2.9. For a particular rock and fluid mobility the various mechanisms can be localized to specific frequency bands where they are the most effective (Courtesy: Hofmann, 2003)

to each other in that they all require fluid motion and they contribute to the velocity dispersion and attenuation simultaneously for partially and fully saturated rocks. A given theory can be effective or dominant under certain physical conditions. All of them have their own sets of assumptions and limitations but they tend to predict the observed attenuation/dispersion in real rocks. It is almost impossible to theoretically quantify the contribution of individual mechanisms but for a given rock and fluid mobility it is possible to identify the frequency band in which a particular mechanism would be most effective as shown in figure 2.9.

The effective elastic moduli of a fluid -saturated solid depends on the degree of saturation and interconnection between pores and cracks. In this figure four separate

regimes are defined: Macro flow, in which fluid in pores can flow out of bulk regions of compression and is similar to drained condition. For a given fluid mobility drained case requires very low frequencies so that fluid has enough time to drain out of the pore spaces. The fluid does not contribute to the modulus of the composite rock. The second regime is the local flow where fluid flows from one pore/crack to another but there is no bulk flow. The frequency range is higher than macro flow and this mechanism is also called the 'squirt' flow. The third regime is the Biot dispersion mechanism where the crossover frequency has already been defined (equation 2.22) and the range of frequency where Biot mechanism operates is higher than local flow. Transition between these cases involve fluid flow, resulting in dissipation/attenuation. Relaxation of shear stresses in viscous fluids also results in dissipation and this kind of mechanism operates at very high frequency as can be seen in the figure 2.9. For every mechanism there is a characteristic frequency where the dissipation is maximum and the moduli change is rapid with frequency. When we decrease the mobility of the fluid the characteristic frequency for all the mechanisms except Biot's mechanism move toward lower frequencies. The opposite happens when the mobility is increased.

2.4 Laboratory measurement

The best way to test these theories and their predictions is to perform laboratory measurements under controlled conditions. A number of such measurements have been made over the years [Wyllie, Gardner and Gregory, 1962; Winkler and Nur, 1979; Spencer, 1979]. All these measurements have their own assumptions and errors. Most of these measurements are done at ultrasonic frequencies and has been discussed in the Introduction chapter. Also it is important to test and adjust the different proposed attenuation/dispersion mechanisms. It may not be possible to differentiate between

them but the understanding of the effects of fluids on attenuation and dispersion in seismic frequency range. The next chapter describes the method used to measure seismic dispersion/attenuation.

Chapter 3

LABORATORY MEASUREMENT

There are several different methods to measure attenuation in the laboratory and these are broadly classified as :

- Free vibration
- Forced vibration
- Wave propagation
- Stress-strain phase angle measurement

The choice of a particular method depends on the range of frequency, strain level and the physical conditions. The stress-strain measurements are applicable at low-frequencies. Wave propagation is usually at ultrasonic frequencies (100 KHz or higher), whereas resonance vibration method is done at 100Hz-100 KHz. The range of frequencies depend on the size of the sample. In this chapter I describe the low-frequency apparatus which I have used to measure the seismic range attenuation and velocity dispersion. Laboratory setup, data-acquisition, data-processing and equipment calibration are described for the low-frequency velocity and attenuation measurements. Then the sources of error are discussed in brief followed by error analysis. Finally the ultrasonic measurement technique is described with the sources of error.

3.1 Low-frequency measurements

In order to compute the velocity dispersion and attenuation we measure the strain amplitude and the phase lag between the applied quasi-static stress and the resulting strain on a rock sample. The basic theory has been discussed in detail in Chapter 2. The technique involves applying a sinusoidal stress of a chosen frequency to a rock sample. This results in a 'Young's modulus' type of deformation. Note that for low-frequencies (5 to 1000 Hz) we do not measure seismic velocity directly, but calculate velocities from the extracted moduli. The system is similar to those developed by Spencer [1981] and Mörig and Burkhardt [1989]. Spencer's measurements were contaminated due to boundary fluid flow and the fact that he did not apply any confining or pore pressure.

The apparatus used for this kind of measurement is suitably named the low-frequency device and is shown in figure 3.1. The cylindrical rock sample is placed between the vessel lid and the shaker on the bottom. The shaker produces vertical displacements which produces axial deformation on the rock. These deformations are picked by the resistive strain gages bonded directly to the surface of the rock. We assume that the sample is isotropic because all our computations are for an isotropic rock. All these measurements are quasi-static in nature. This means that there is no wave-propagation. The ratio of wavelength to sample length is huge and the deformation along the sample length is linear. This requires that our driving frequency should be restricted to small seismic frequency range. This allows us to measure the dispersion and attenuation in seismic band only. The sample is encapsulated in flexible epoxy both to prevent the confining gas from entering the sample and to seal the outer boundary against pore fluid movement. The sample assembly is shown in

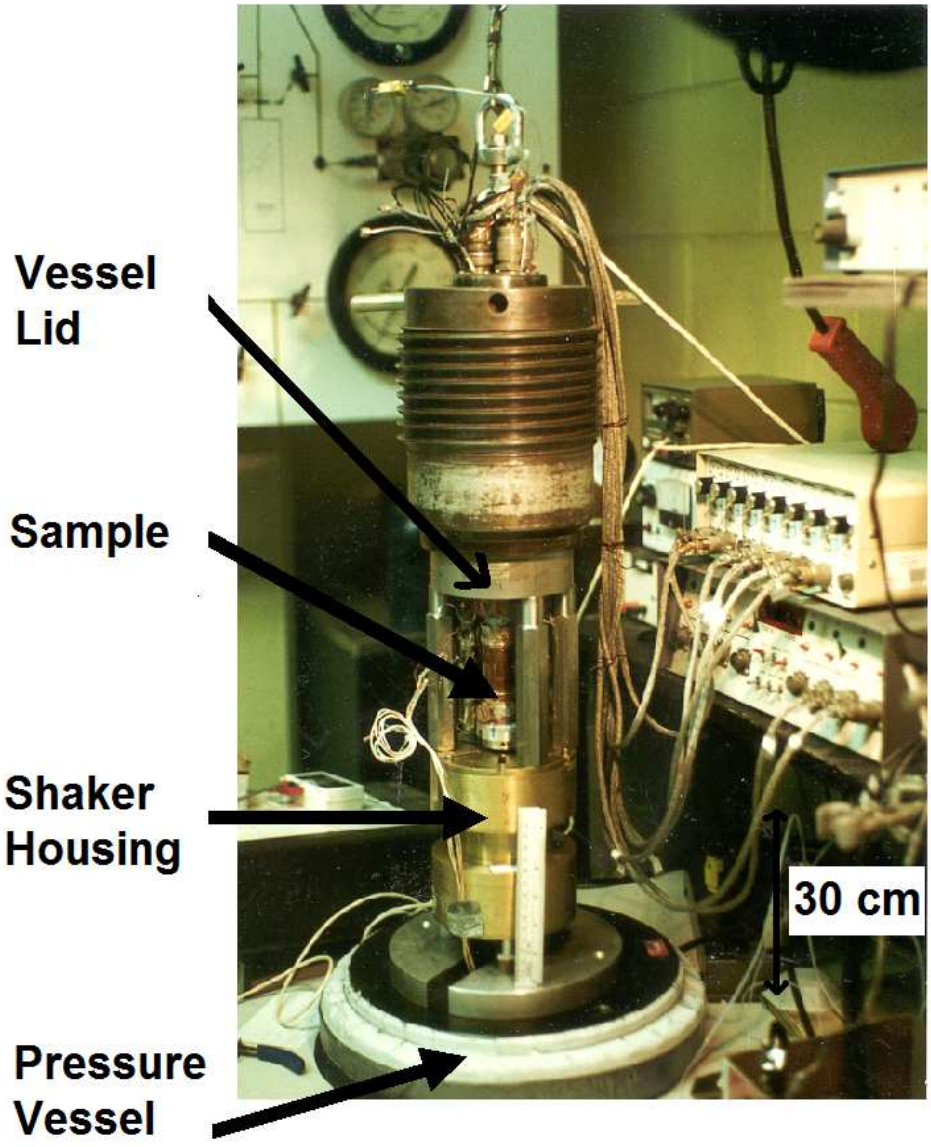

FIG. 3.1. Low-frequency device.

figure 3.2. Two aluminum caps are placed on top and bottom of the sample for use as a strain reference as described later (figure 3.3). There are four pairs of strain gages on the rock: two horizontal and two vertical. Two pairs of vertical strain gages are placed on the top aluminum standard as well. The strain gage pairs are placed diagonally opposite on the sample to eliminate any bending effect. Uniaxial sinusoidal stress is applied at known discrete frequencies by the shaker. The strains are picked up by the gages on the rock and on the aluminum standard (figure 3.3). The magnitude of these strains give the elastic moduli of the rock and the phase angle between the rock strain and aluminum strain gives the Q^{-1} values. We assume that the stress distribution is homogeneous throughout the rock sample assembly. Pore fluid line contacts the top and bottom of the sample which allows fluid flow inside the sample and independent control of pore pressure.

The pore fluid lines have small valves which can be opened and closed to simulate open and closed boundary conditions. White [1983] pointed out that macroscopic fluid flow to the free boundary of the sample contributes to the attenuation and can be a source of significant error. The sample is sealed on its lateral surface to prevent boundary flow. It is still possible that the fluid movement can occur in and out of the pore fluid line. The entire assembly is then kept inside pressure vessel to apply confining pressure. The pressure inside the vessel is generated by nitrogen gas.

To measure the amplitude and the phase of the applied stress we use an aluminum standard in series with the sample with similar strain gages as as on the sample (figure 3.3). Aluminum is elastic (compared to rocks) and thus the applied stress is in phase with the observed strain on the aluminum. The signals from both the aluminum standard and the rock sample go through the same amplification and acquisition

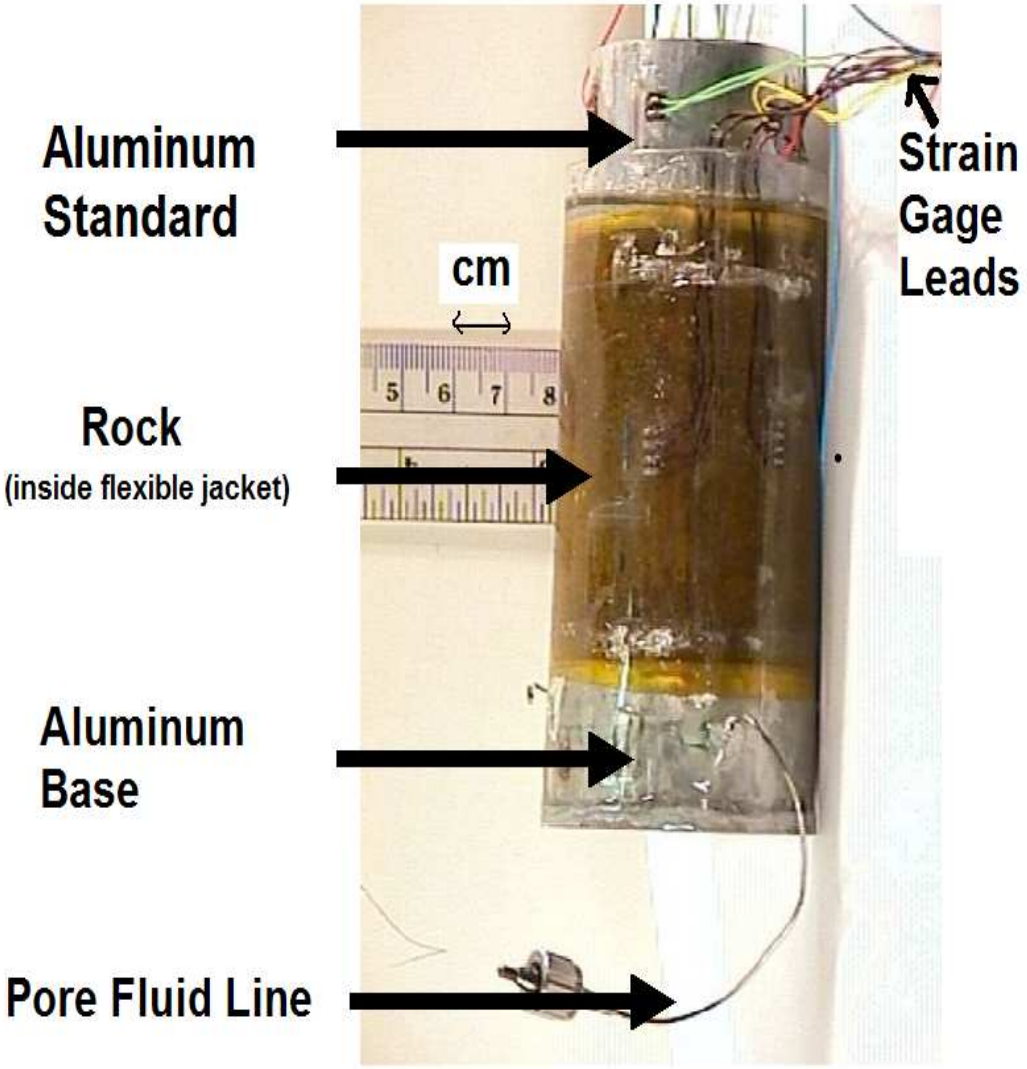

FIG. 3.2. Rock sample is a cylindrical sample assembly with diameter around 3.8 cm and length 6.3 cm.

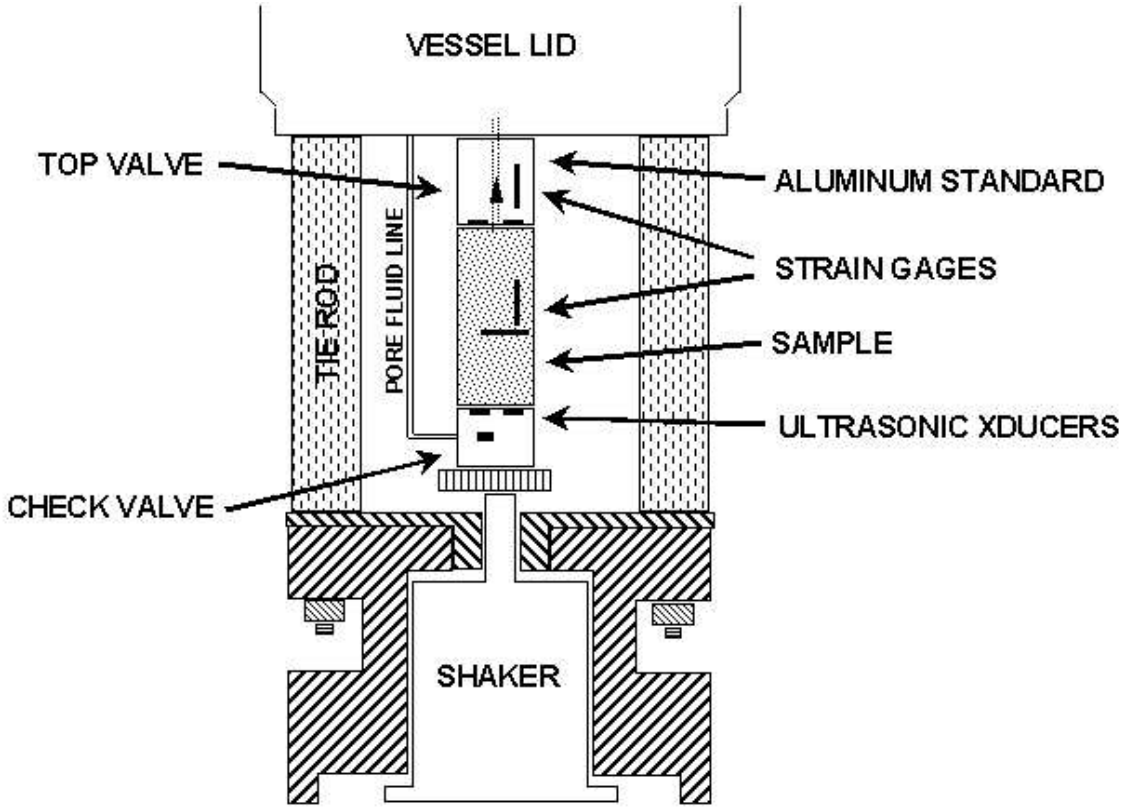

FIG. 3.3. Schematic of the low-frequency setup.

path. In this way, phase shifts and amplitude changes due to the driving or acquisition electronics are cancelled. The aluminum strains thus serve as our reference. Figure 3.4 shows the relative amplitudes of the strains which result from sinusoidal stress.

For an isotropic material, there are only two independent elastic parameters. We measure, the vertical and horizontal strains to extract Young's modulus (E) and Poisson's ratio (ν). Under the assumption of isotropy all other parameters can be derived. The Young's strain (vertical gage) in the rock lags the strain on the aluminum and this lag gives the Q_E^{-1} or the Young's mode attenuation. The horizontal (Poisson's gage) strain is π radians out of phase with the Young's strain on the rock if the rock

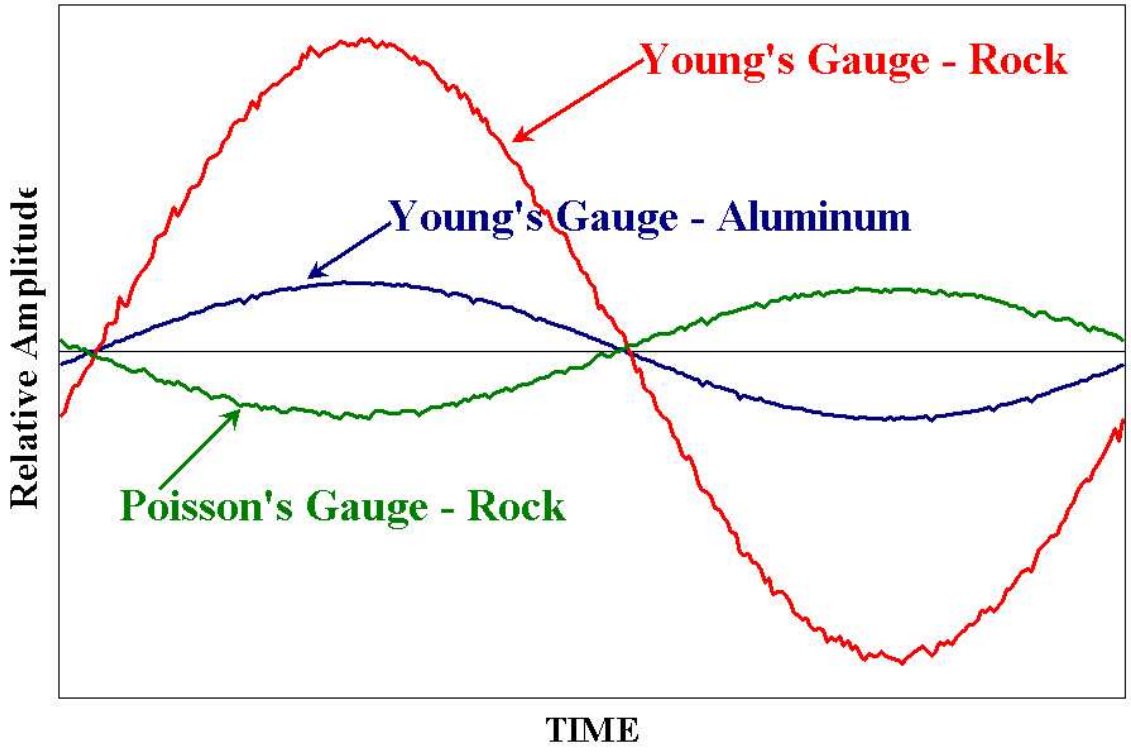

FIG. 3.4. Relative amplitudes of the strains from the rock sample and the aluminum standard. The waveforms are averaged over a number of periods. Young's gage is parallel to the sample axis and Poisson's gage is orthogonal to the axis.

is perfectly elastic. This effect is shown in figure 3.5.

3.1.1 Low-frequency sample preparation

One advantage of using this low-frequency technique is that small core plugs can be used in our measurements. The dimensions of these samples vary but in most cases they are approximately 5.1 cm (2 inches) long and 2.54 or 3.81 cm (1 or 1.5 inch) in diameter. An aluminum standard and a base are epoxied to the sample. The sample's lateral surface is coated with epoxy and kapton film.

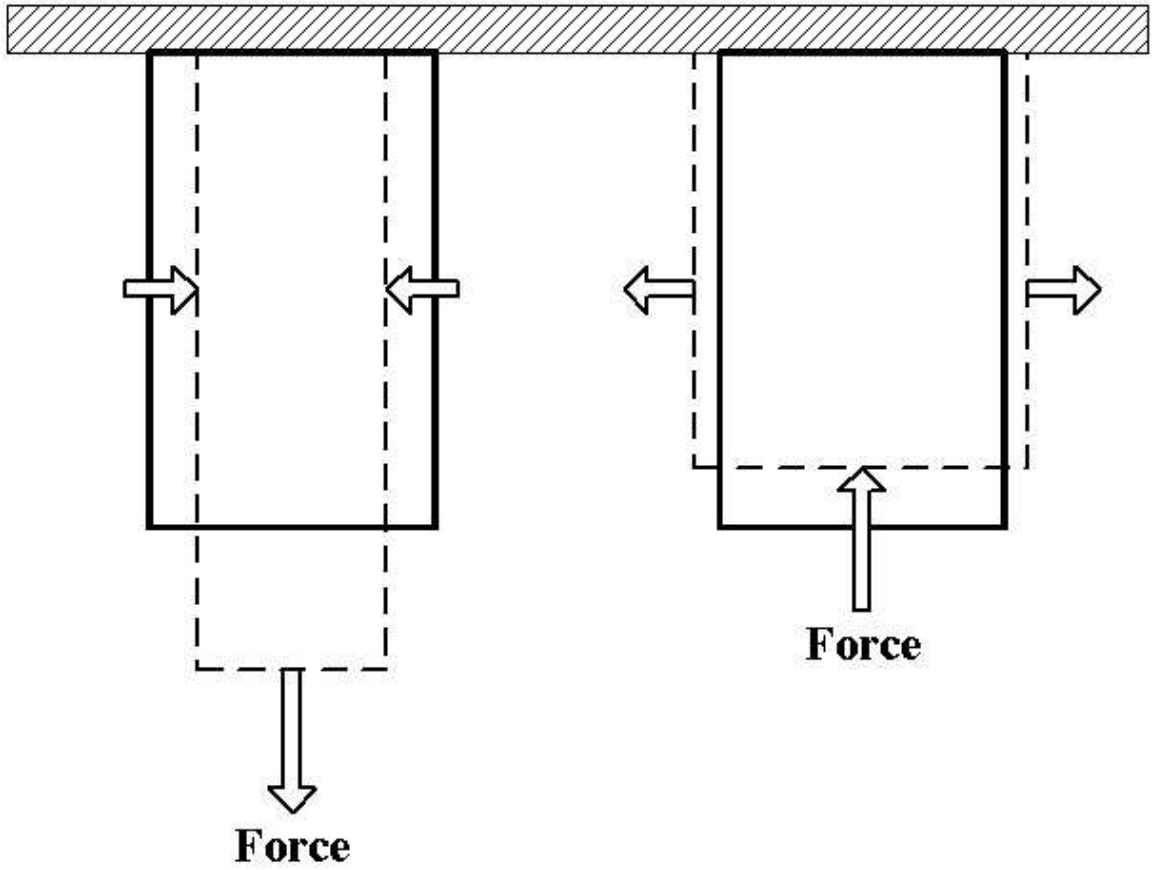

FIG. 3.5. Vertical and horizontal deformation as the rock is axially deformed by the shaker. Both during loading and unloading the horizontal deformation is approximately π radians out of phase with the vertical deformation.

Resistive strain gages are bonded to the surface of the samples. At present we can have a maximum of eight pair of strain gages. The advantage of using strain gages is that they can be oriented in two different directions (horizontal and vertical) to collect both axial and circumferential strain data. Also these strain gages are small and are less sensitive to equipment resonance as compared to other transducers. Each pair of the strain gage is hooked to the opposite sides of a Wheatstone Bridge. The

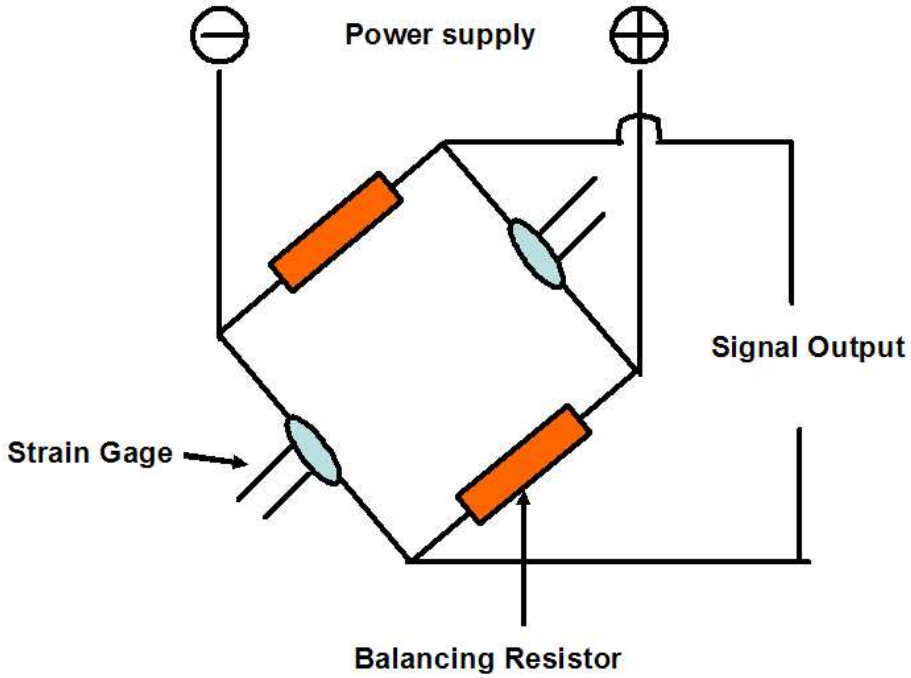

FIG. 3.6. Wheatstone Bridge: The change in resistance is converted into voltage which is the output from the equipment.

deformation on the sample causes a change in resistance of the gage and is converted to voltage in the Bridge (figure 3.6).

A pore fluid line is used to inject different fluids and control pore pressure. Two tubes run from the top and bottom of the sample. The sample is then covered with Kapton tape which has low diffusivity and thus creates a pressure seal. The strain gages are connected with wires and the sample covered with shrink tubing. The whole sample is then coated with resin. The entire schematic is shown in Figure 3.7.

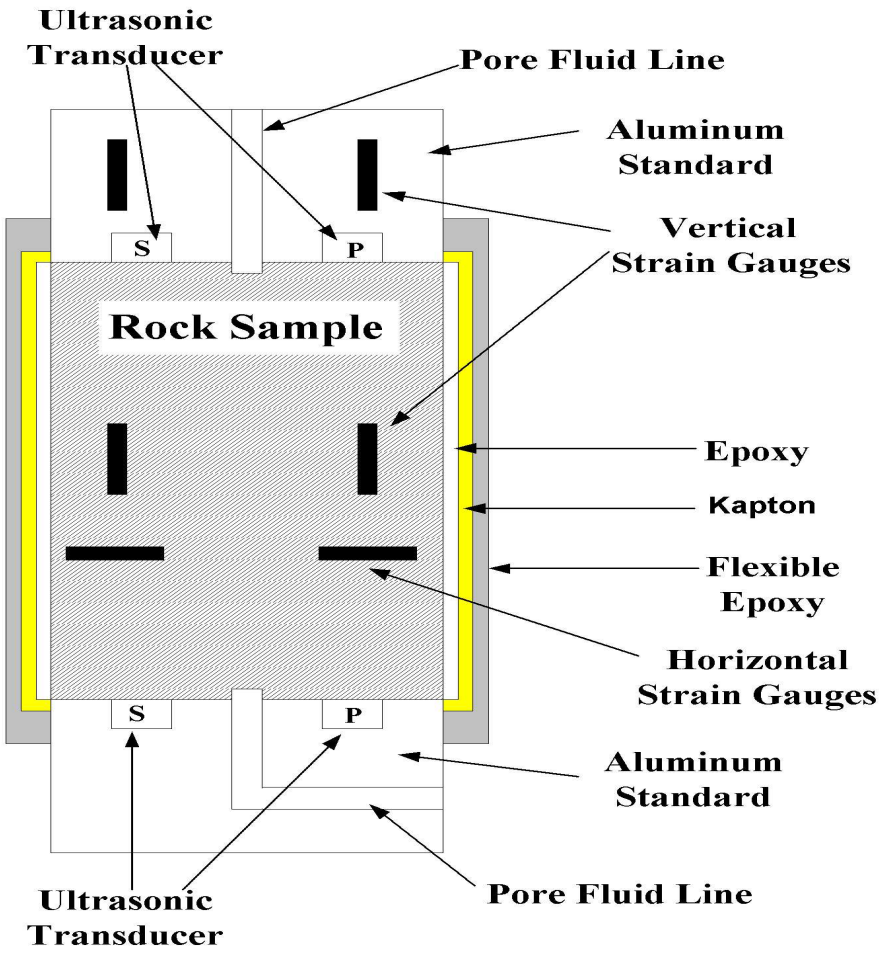

FIG. 3.7. Schematic of the sample assembly.

3.1.2 Calculation of strain and elastic moduli

The ratio of the output from the Wheatstone Bridge (figure 3.6) and the power supply gives us the strain from a particular gage. If the supply voltage is V volts and the output from the unbalanced bridge is V_0 then the strain ϵ is given by :

$$\frac{V_0}{V} = \frac{F\epsilon}{2 + F\epsilon 10^{-6}} \tag{3.1}$$

$$\epsilon = \frac{2\frac{V_0}{V}}{F\left(1 - \frac{V_0}{V}10^{-6}\right)} \tag{3.2}$$

where the gage factor (F) is defined by the manufacturer and it depends on the kind of gage being used. The foil gages have a gage factor of $2.08 \pm 0.5\%$, whereas the semi-conductor gage has the factor of $155 \pm 5\%$. Semiconductor gages are more sensitive compared to the foil gages but they are less accurate, very small and mounting becomes difficult. On the other hand foil gages are more robust as they they are less affected by pressure and temperature but their low-resolution makes them less preferable compared to semi-conductor gages for our experiments because the expected strains are very low ($\sim 10^{-8}$).

The stress in the sample is related to the strain via Young's modulus (equation 3.3). The negative ratio of the horizontal (Poisson's gage) strain to the vertical (Young's gage) strain gives the Poisson's ratio (equation 3.4).

$$\sigma_{11} = E\epsilon_{11} \tag{3.3}$$

$$\nu = -\frac{\epsilon_{22}}{\epsilon_{11}} \tag{3.4}$$

where σ_{11} is the vertical stress and ϵ_{22} and ϵ_{11} are the horizontal and vertical strains respectively. If we assume that the stress is uniformly distributed in the column such that $\sigma_{11} = \sigma_{al}$, where σ_{al} is the axial stress on the aluminum standard, the Young's modulus of the rock can be computed by using the relation:

$$\sigma_{11} = E_{rx}\epsilon_{11}^{rx} = \sigma_{al} = E_{al}\epsilon_{11}^{al} \tag{3.5}$$

$$E_{rx} = E_{al}\frac{\epsilon_{11}^{al}}{\epsilon_{11}^{rx}} \tag{3.6}$$

where sub and superscripts rx stands for a rock and sub and superscripts al stands for aluminum standard. The Young's modulus for aluminum is a known quantity. Using the Poisson's ratio and the Young's modulus we can compute the shear, bulk moduli and the velocities by using the following relations:

$$\mu = \frac{E_{rx}}{2(1+\nu)} \tag{3.7}$$

$$k = \frac{E_{rx}}{3(1-2\nu)} \tag{3.8}$$

$$V_S = \sqrt{\frac{\mu}{\rho}} \tag{3.9}$$

$$V_P = \sqrt{\frac{k + \frac{4}{3}\mu}{\rho}} \tag{3.10}$$

where ρ is the density of the rock. The phase angle between ϵ_{11}^{al} and ϵ_{11}^{rx} gives the Q_E^{-1}. Using this result and the phase angle between ϵ_{11}^{rx} and ϵ_{22}^{rx} we can compute the Q^{-1} for other propagation modes as discussed in Chapter 2.

3.1.3 Data acquisition and processing

Currently, eight channels are available to collect strain data from the rock sample and aluminum standard. The schematic of the acquisition system is shown in figure

3.8.

The source sinusoidal signal is either generated from the function generator or the lock-in amplifier. The signal is then amplified and fed into the shaker. The output is again amplified and is then branched into two paths. One path is digitized using a National Instruments A/D board. The A/D board has fixed digitizing rates available. Given the choice of samples/cycle (32,64,256) the frequency of investigation becomes fixed. The second path goes to the lock-in amplifier and this will be discussed later. My initial work involved finding the most suitable method of acquiring and processing this data.

In the first approach, which was used initially, the time series (first path) was subdivided into three and a Fast Fourier Transform (FFT) was applied to each subdivision. A mean and standard deviation was computed for the RMS voltage of each channel at a particular driving frequency. This was done using a subroutine in the LabView acquisition software. The frequency range was from 3 Hz to 3000 Hz. Frequencies above 1000 Hz caused resonance in the system and is undesired in our measurement scheme. This approach was appropriate to measure the strain amplitudes but the phase angle extraction was not very accurate and in most of the measurements negative attenuation values were obtained and also the results were not consistent. Also, this approach restricts us to some unique frequencies. The major difficulty of this kind of measurement stems from the weak and noisy signal. The strains generated in the sample are of the order of 10^{-7} (seismic strain amplitudes) which corresponds to a weak signal of the order of 10^{-6} volts. The signal goes through the amplifier and is digitized. Also, if we are measuring quality factors in the range of 10 to 100 it would mean phase angle measurements in the range of 0.01-0.1 radian (see Chapter 2).

In theory the output signals should be sinusoids with different phase shifts. In re-

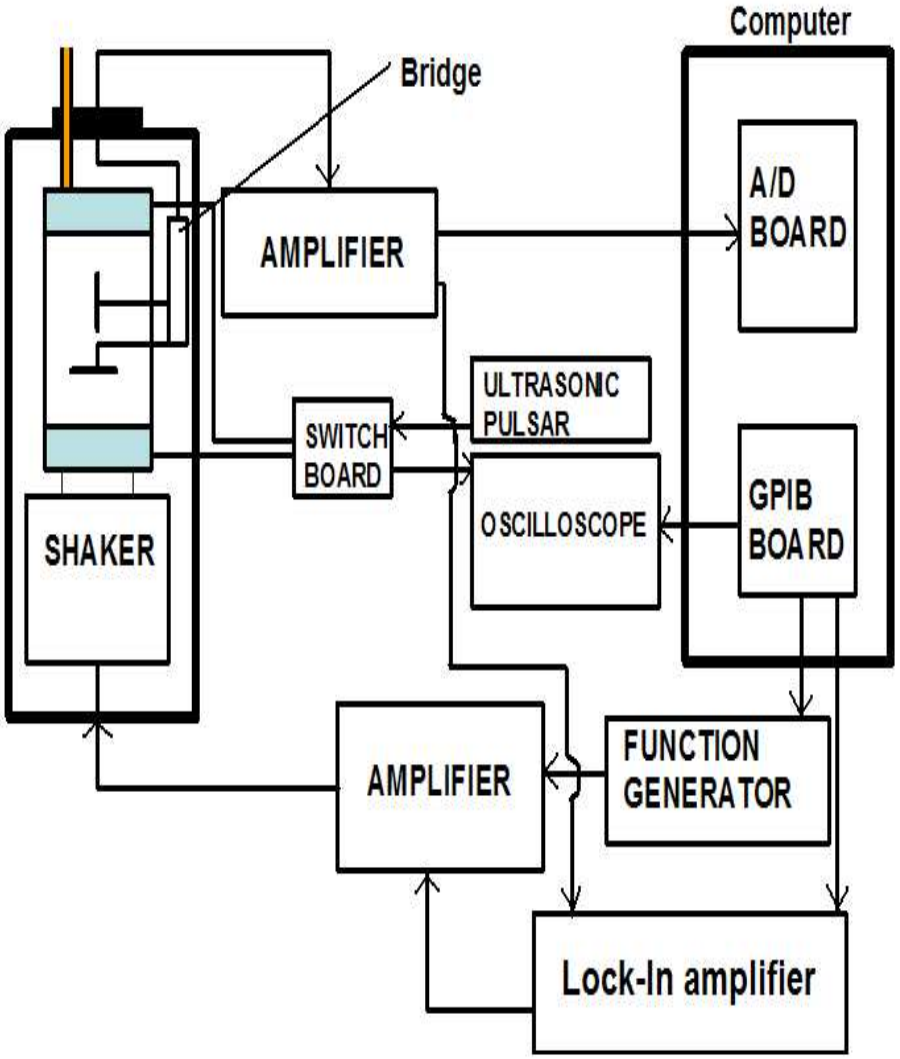

FIG. 3.8. Schematic of the acquisition setup: Both low-frequency and ultrasonic setup are shown here.

ality the signals have both low and high frequency noises. These random noises are generated from the electronics and the laboratory environment. In the second approach, the low-frequency noise (time varying offset) is removed, by a process called normalization, and is done by either a moving average or linear interpolation. Then the mean period is calculated by computing the mean at each corresponding point in all the periods of the sinusoid. This helps to remove the high frequency noise. Then the mean period could be approximated with a function $A*\sin(T)+B*\cos(T)$. The coefficients A and B can be computed by either by regression or Fourier analysis. Figures 3.9 and 3.10 show the result of one such operation where we go from a raw signal cycle data to the summed (mean) period. This approach still did not give us satisfactory results. The reason could be that we were still involving analog to digital conversion and the filtering process was not good enough to eliminate the noise.

In the third approach I used a lock-in amplifier (Stanford research model). This instrument detects very low amplitude signals on the order of nano-volts and can work well with extremely low signal to noise ratio. It uses a technique called the phase-sensitive detection which can filter out the signal at a given reference frequency and phase and eliminates all other signals/noise. After taking several measurements the time constants (averaging) for every reference frequency was established. More detail about the lock-in amplifier can be obtained from the manual (SRS-850 basics).

The frequency range we use is from 25 Hz to 1000 Hz. The lower frequency limit was decided on the basis of time required to measure over numerous cycles. Too large a time (half an hour) for measurement violates our assumption that the state of the rock has not changed. The upper limit was kept at 1000 Hz because above that frequency we encounter system resonance, which we want to avoid as has been stated earlier.

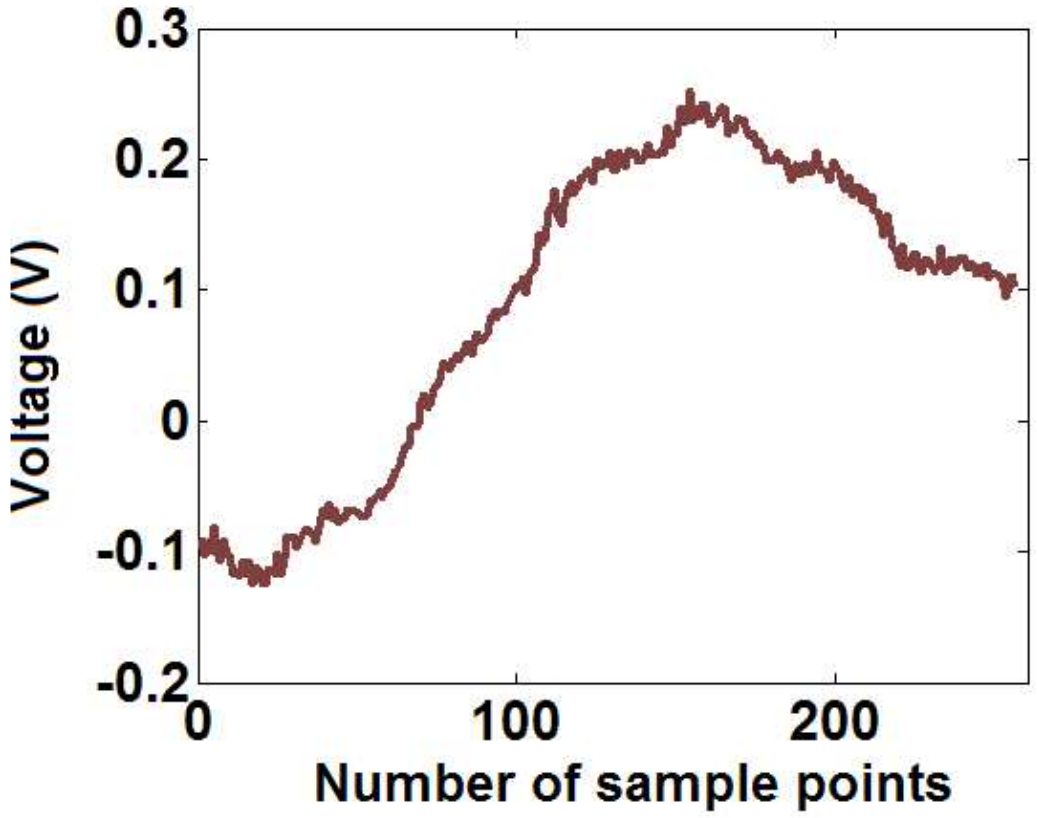

FIG. 3.9. Input voltage data to the processing sequence. Y-axis has the amplified voltage and x-axis has the number of digitized points.

3.1.4 Error, assumptions and limitations

As stated earlier one of the biggest problems with these low-frequency measurements is the poor signal. The source of errors are manifold and in many cases they are related to the setup and preparation of the sample. These errors could be classified as systematic.

Some of the issues with sample preparation are : alignment of the ends, sensitivity of the strain measurements to surface coatings, surface damage during cutting, hetero-

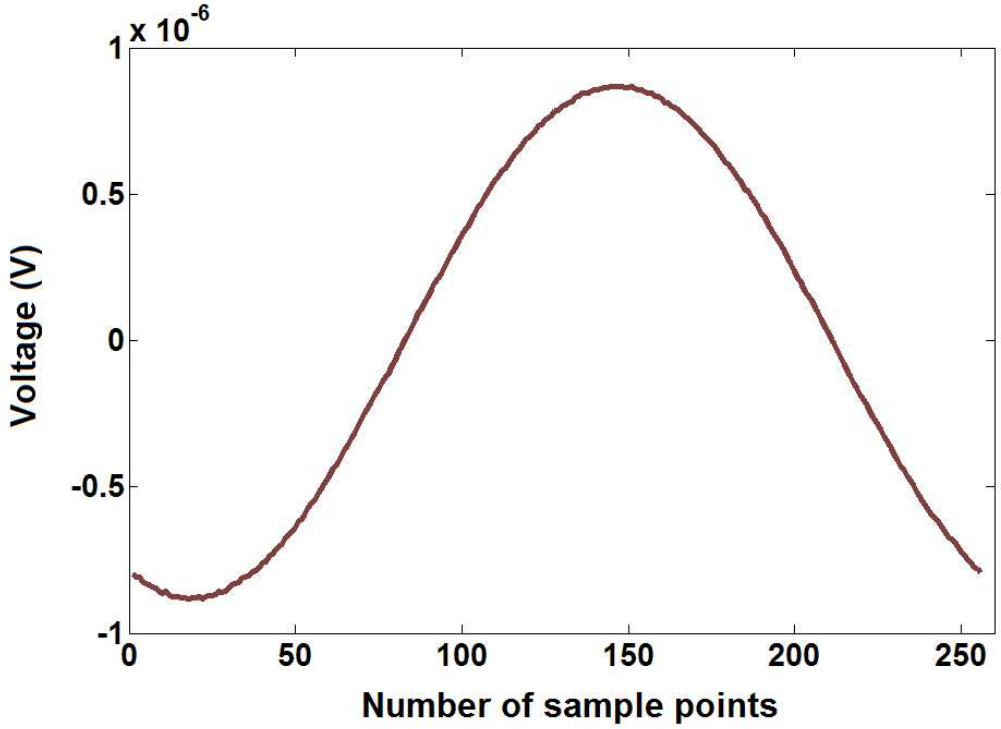

FIG. 3.10. Mean period after processing. Gain and factor constants are applied to the data.

geneity and diffusion of the confining gas through the jacket. If there is poor bonding between the sample and the standard then the assumption that the stress is homogeneous across the assembly is not valid. The strain amplitude could be affected due to this discontinuity. Also, bending of the sample is undesirable because we are trying to measure Young's deformation and not bending. In order to avoid the effect of discontinuity and bending, we have several gages on the surface and we average them.

Another source of error could be the thickness of the adhesive used to stick the

gages on the sample surface. For example a small air bubble trapped in the epoxy during this process can degrade the results. The Poisson's gage is either only tangentially in contact with the rock or has to be bend in order to glue it laterally on the rock surface. This partial bond or bending can affect the gage factor of the semiconductor gages. Changes in temperature and pressure can greatly influence the gage factor [Hofmann, 2001]. Semiconductor gages are more sensitive to changes in temperature ($0.26\%/c^0$) and pressure compared to foil gages. Thus gage factor and output voltage can be a source of error if they are contaminated. Input voltage does not change enough to cause any worry ($15 \pm .001$).

In all our measurements we assume a homogeneous sample. Strain gages occupy a very small area and it is an advantage as well as a disadvantage. The gages are representative of a very localized area of the sample and hence in case of a inhomogeneous sample the point measurement may not be representative of the whole sample. Figure 3.11 shows the porosity distribution obtained by CT scan of a rock sample: blue low porosity and purple high porosity [Hofmann, 2001]. It is clear that the porosity distribution is not uniform. Porosity can related to the strength (moduli) of the rock and has an inverse relation [Murphy et al., 1993]. Thus based on where we put the strain gages we will get different moduli of the rock. This change could be as high as 30%. In Chapter 4 it can be seen that most of the rocks have very inhomogeneous distribution of the grain size, pore size and geometry. Thus our measurements could just be giving us local effect.

Resonance is another source of error. Around 120 Hz and above 1000 Hz there is system resonance and the velocity and attenuation values are unstable. The sample along with the shaker resonates above 1000 Hz. The sample assembly along with

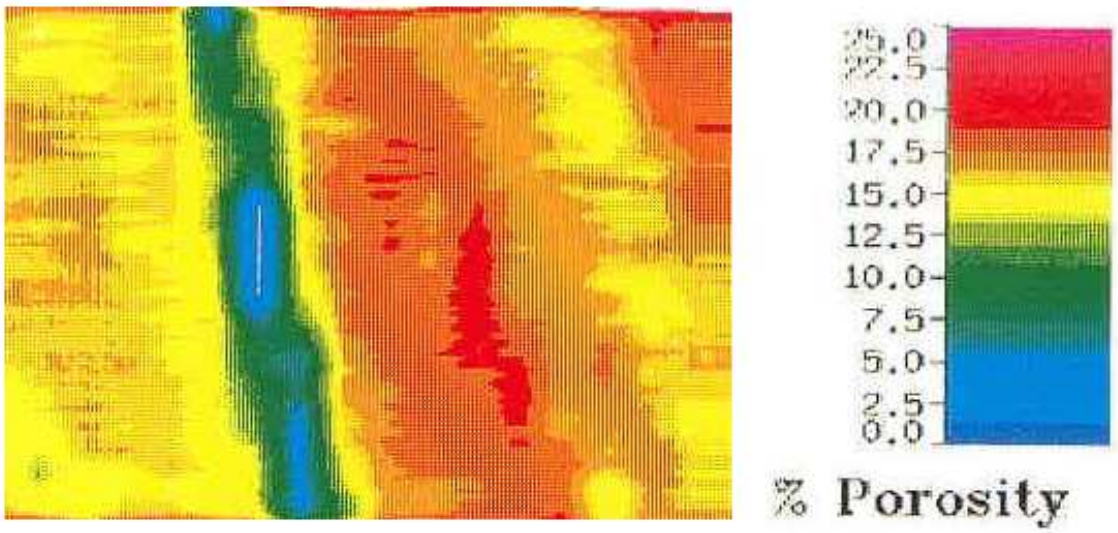

FIG. 3.11. Porosity distribution of a rock sample. Blue areas are low porosity (0%) and purple areas are high porosity (25%) [Hofmann, 2001].

the pressure vessel could be resonating around 120 Hz. Resonance effect is more pronounced in the open boundary condition when the fluids also start resonating within the pore fluid lines. We assume that the stress and strains are linear. At high strain levels ($> 10^{-5}$) the moduli and attenuation are dependent on the strain amplitudes (figure 3.12). This is the reason why we keep the strain amplitudes below 10^{-7}. This is also helpful because it overlaps the strain amplitudes observed in real seismic experiments [Wideman and Major, 1967].

As a result of these factors, any quantitative error analysis is an extremely difficult task for these systematic errors. In order to make sure that these systematic errors are not large we always compare the dry low-frequency velocity with the ultrasonic velocity. In most cases the velocities are comparable with a maximum of 5% difference.

Ultrasonic measrements are free of the systematic errors discussed above and thus if the ultrasonic and low-frequency velocities are comparable then we can be sure that the systematic errors have been taken care of. In order to compute the measurement error in velocity the error in gage factor was assumed to be Gaussian with a mean of zero and standard deviation of $\pm 5\%$. Propagating this error in the strain calculation gave the standard deviations in Young's, Poisson's and aluminum strains. The error was further propagated in the Young's, shear and bulk moduli and finally in the shear and compressional velocities. The result is shown in figure 3.13 where the shear velocity has 4% standard deviation and the compressional velocity has 3.5% standard deviation.

The main source of error in phase angle measurements stem from the weak signals. This is more pronounced for the Poisson's gage. Poisson's ratio can vary from 0 to 0.5 (liquid). Thus we can have a very good phase angle resolution at 0.5 Poisson's ratio value and no resolution at zero Poisson's ratio value. Young's gage has the strongest signal (around 0.3 Volts after amplification) and the signal strength of the aluminum gage is around 0.08 Volts (amplified). Poisson's gage signal strength varies anywhere from 0.04 Volts (dry rock) to 1.2 Volts (saturated rock). In order to compute the absolute error on the Young's gage the output of the lock-in amplifier was fed into the LAT-45 attenuator. The output from the attenuator was fed in the input of the lock-in amplifier. The signal was attenuated in steps of 5 dB and the RMS voltage and phase angles were noted. Due to attenuation of signal the phase angle values varied and the variation becomes large at very weak signal strength. The absolute change in phase angle from the unattenuated signal (1 Volt) to a value of around 0.3 (corresponding to Young's gage signal strength) gives the absolute phase angle error (standard deviation) in Young's gage phase angle. The

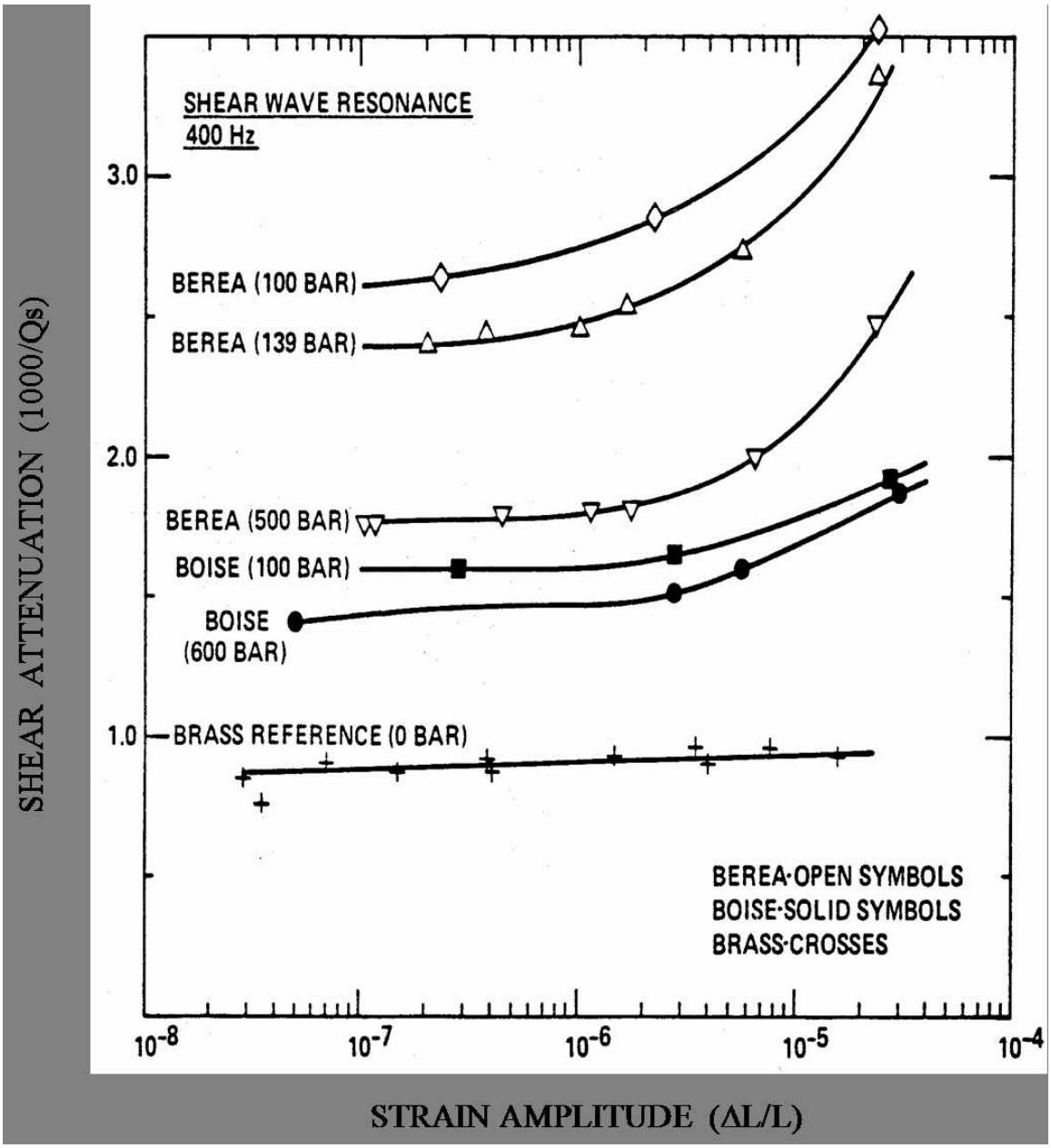

FIG. 3.12. Tittman et al. [1981] show amplitude dependent attenuation. Note that above 10^{-7} strain amplitudes the shear attenuation is non-linear.

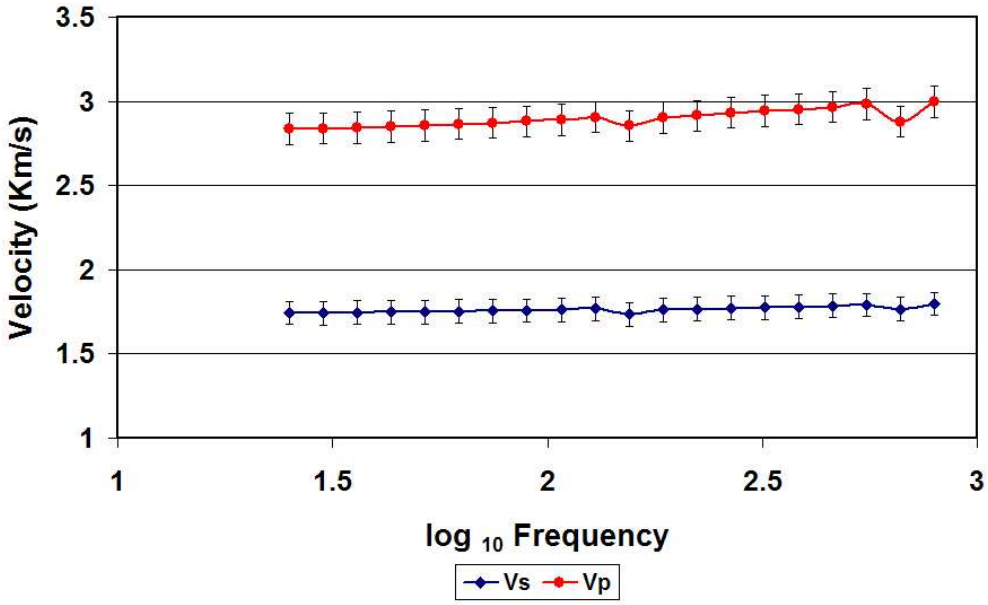

FIG. 3.13. Measurement error in velocity. Standard deviation in semiconductor gage 155 $\pm 5\%$ is propagated through various steps of computations to obtain the standard deviations in shear and compressional velocities.

next step was to find the absolute error in aluminum and Poisson's gage phase angle. Same procedure was applied but this time the Young's gage signal from a dry rock sample was analyzed. The input voltage of the Wheatstone Bridge was reduced in steps of a Volt from the initial value of 15 Volts to a minimum of 2 Volts. The change in phase angle was noted at each step. The absolute difference between the initial phase angel and that at every step was computed. The change in phase angle is due to the weakening of the Young's gage signal. To all of these phase angle differences the standard deviation of the Young's gage was added. The result is shown in figure 3.14. The whole analysis was performed for 10 Hz, 100 Hz and 1000 Hz.

Using these absolute errors as Gaussian noise with zero mean and known stan-

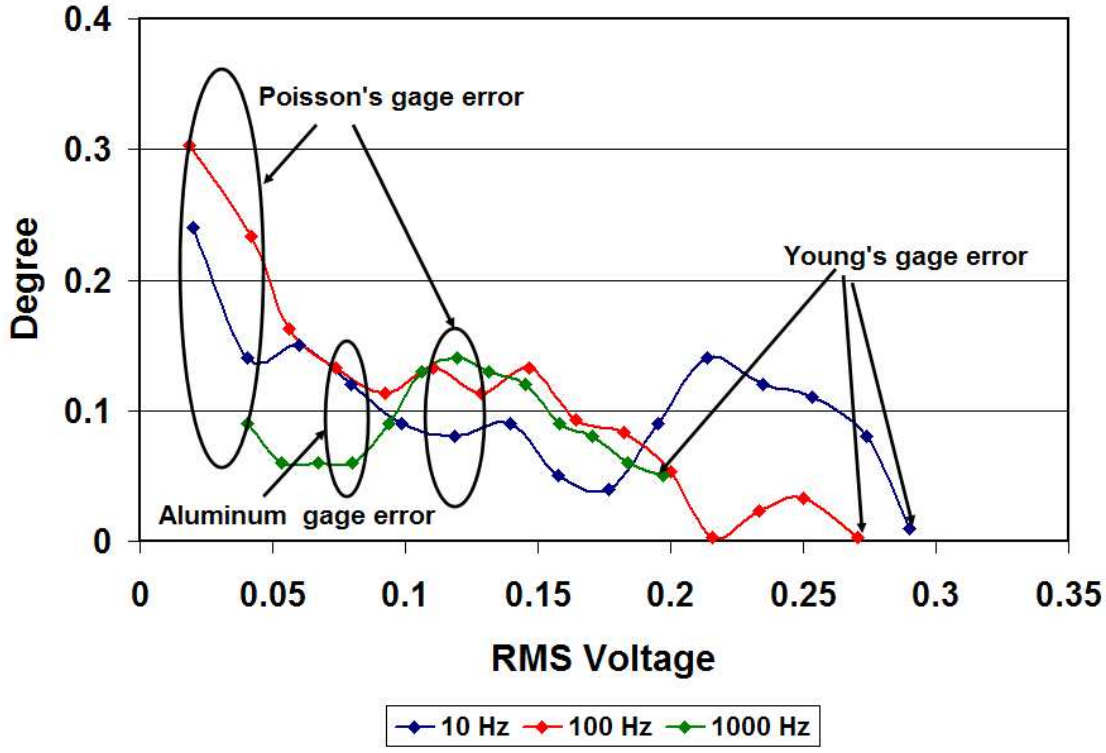

FIG. 3.14. Absolute error in phase angles for Young's, aluminum and Poisson's gage. For Poisson's gage the error drops as we move from dry/partial saturated rock to full saturated rock.

dard deviation the errors in 1/Qe, 1/Qs, 1/Qp and 1/Qk were computed. The standard deviation in Poisson's ratio was also included in the error analysis. For 50% brine saturated ITF-51 sample all the four modes of attenuation with their absolute error bars are shown in figure 3.15. It can be seen clearly that 1/Qk has the highest values and 1/Qs has the lowest values. The error bars do not overlap and this means that the measured values are within 67% confidence interval. As we go from partial brine saturation to full brine saturation the Poisson's ratio value increases. The absolute phase angle error in Poisson's gage changes but the absolute phase angle error

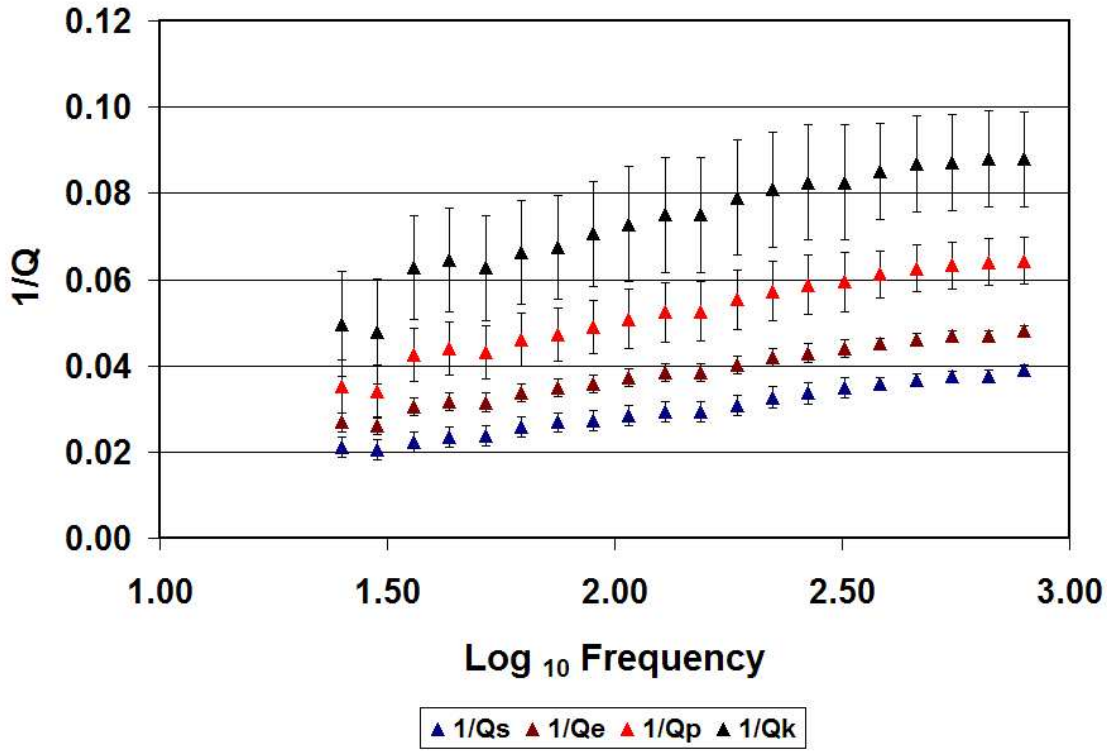

FIG. 3.15. ITF-51: Measurement error in the different modes of attenuation for 50% brine saturation. The error bars do not overlap.

in Young's and aluminum gage remain almost the same because their signal strength does not change much. The absolute values of 1/Qe and 1/Qs does not change much from partial saturated to full saturated case. The error bars on 1/Qe and 1/Qs are also small (5% error). The 1/Qp and 1/Qk values drop considerably compared to partial saturated case and become almost equal to zero. The error bars increase due to very small absolute values of 1/Qp and 1/Qk and start to overlap with the error bars in 1/Qe and 1/Qs. 1/Qp and 1/Qk values are computed from 1/Qe and 1/Qs values using the formula given in Chapter 2. From the formula it is clear that the

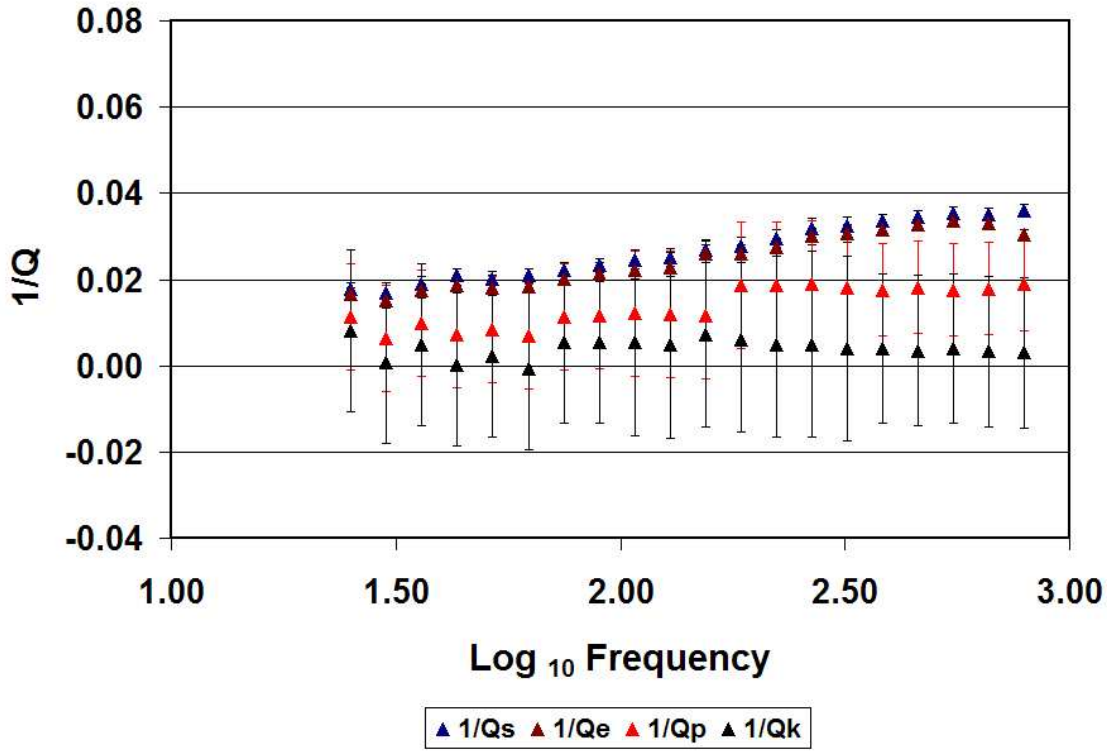

FIG. 3.16. ITF-51: Measurement error in the different modes of attenuation for full brine saturation. Error bars overlap in this case.

absolute value of 1/Qp and 1/Qk drop considerably as we go from partial saturated rock to full saturated. The huge error bars indicate that these absolute values can not be ascertained with high confidence which is clear in figure 3.16. Thus even if the absolute error is large the relative errors are small and with confidence we can say that the 1/Qs value is highest and 1/Qk is the lowest for a fully saturated rock. The mean and the standard deviations for all the four modes of attenuation at partial and full saturated cases are given in tables 3.1 and 3.2.

Log Frequency	1/Qe+δ1/Qe	1/Qs+δ1/Qs	1/Qp+δ1/Qp	1/Qk+δ1/Qk
1.40	0.027+0.0021	0.021+0.0023	0.035+0.0062	0.050+0.0121
1.48	0.026+0.0021	0.020+0.0023	0.034+0.0062	0.048+0.0121
1.56	0.031+0.0021	0.022+0.0023	0.042+0.0062	0.063+0.0121
1.64	0.032+0.0021	0.023+0.0023	0.044+0.0062	0.065+0.0121
1.72	0.032+0.0021	0.024+0.0023	0.043+0.0062	0.063+0.0121
1.79	0.034+0.0021	0.026+0.0023	0.046+0.0062	0.066+0.0121
1.87	0.035+0.0021	0.027+0.0023	0.047+0.0062	0.068+0.0121
1.95	0.036+0.0021	0.027+0.0023	0.049+0.0062	0.071+0.0121
2.03	0.037+0.0021	0.029+0.0024	0.051+0.0069	0.073+0.0134
2.11	0.038+0.0021	0.029+0.0024	0.053+0.0069	0.075+0.0134
2.19	0.040+0.0021	0.029+0.0024	0.053+0.0069	0.075+0.0134
2.27	0.042+0.0021	0.031+0.0024	0.055+0.0069	0.079+0.0134
2.35	0.043+0.0021	0.033+0.0024	0.057+0.0069	0.081+0.0134
2.43	0.044+0.0021	0.034+0.0024	0.059+0.0069	0.083+0.0134
2.51	0.045+0.0021	0.035+0.0024	0.059+0.0069	0.083+0.0134
2.58	0.046+0.0013	0.036+0.0014	0.061+0.0054	0.085+0.0111
2.66	0.047+0.0013	0.037+0.0014	0.063+0.0054	0.087+0.0111
2.74	0.047+0.0013	0.037+0.0014	0.063+0.0054	0.087+0.0111
2.82	0.047+0.0013	0.038+0.0014	0.064+0.0054	0.088+0.0111
2.90	0.048+0.0013	0.039+0.0014	0.064+0.0054	0.088+0.0111

Table 3.1. Mean and standard deviations of all the four modes of attenuation for 50% brine saturated ITF-51 sample.

3.2 Calibration

Before measuring rock samples it was important to calibrate our instrument against known measurements of modulus and attenuation. Figure 3.17 shows that the moduli and attenuation measurements done on an isotropic and homogeneous material by our equipment, show good agreement with measurements done by various other measurement techniques [Batzle, 2003]. Our system has also been calibrated against aluminum where zero phase angles were measured. Loss tangent measurements on plexiglass (*Polymethyl Meta*) also confirmed the consistency of our system.

Log Frequency	1/Qe+δ1/Qe	1/Qs+δ1/Qs	1/Qp+δ1/Qp	1/Qk+δ1/Qk
1.40	0.017+0.0016	0.018+0.0016	0.011+0.0123	0.008+0.0187
1.48	0.015+0.0016	0.017+0.0016	0.006+0.0123	0.001+0.0187
1.56	0.017+0.0016	0.019+0.0016	0.010+0.0123	0.005+0.0187
1.64	0.019+0.0016	0.021+0.0016	0.007+0.0123	0.000+0.0187
1.72	0.018+0.0016	0.020+0.0016	0.008+0.0123	0.002+0.0187
1.79	0.018+0.0016	0.021+0.0016	0.007+0.0123	-0.001+0.0187
1.87	0.020+0.0016	0.022+0.0016	0.011+0.0123	0.005+0.0187
1.95	0.021+0.0016	0.023+0.0016	0.012+0.0123	0.005+0.0187
2.03	0.022+0.002	0.025+0.0021	0.012+0.0146	0.005+0.0215
2.11	0.023+0.002	0.025+0.0021	0.012+0.0146	0.007+0.0215
2.19	0.026+0.002	0.027+0.0021	0.012+0.0146	0.006+0.0215
2.27	0.026+0.002	0.028+0.0021	0.019+0.0146	0.005+0.0215
2.35	0.027+0.002	0.029+0.0021	0.019+0.0146	0.005+0.0215
2.43	0.030+0.002	0.032+0.0021	0.019+0.0146	0.004+0.0215
2.51	0.031+0.002	0.032+0.0021	0.018+0.0146	0.004+0.0215
2.58	0.032+0.0013	0.034+0.0015	0.018+0.0108	0.004+0.0174
2.66	0.033+0.0013	0.034+0.0015	0.018+0.0108	0.004+0.0174
2.74	0.034+0.0013	0.035+0.0015	0.018+0.0108	0.004+0.0174
2.82	0.033+0.0013	0.035+0.0015	0.018+0.0108	0.003+0.0174
2.90	0.030+0.0013	0.036+0.0015	0.019+0.0108	0.003+0.0174

Table 3.2. Mean and standard deviations of all the four modes of attenuation for full brine saturated ITF-51 sample.

Two measurements were made-one at room temperature and one at 40^0 C. The results is shown in Figure 3.18.

The loss tangent data can be described by Colo-Cole distribution of relaxation times. The shift in the relaxation time (loss tangent peak) with increasing temperature is due to the change in viscosity of the plexiglass fibres [Nowick and Berry, 1972]. These values match very closely to the measurements done by James Spencer [Spencer, 1981].

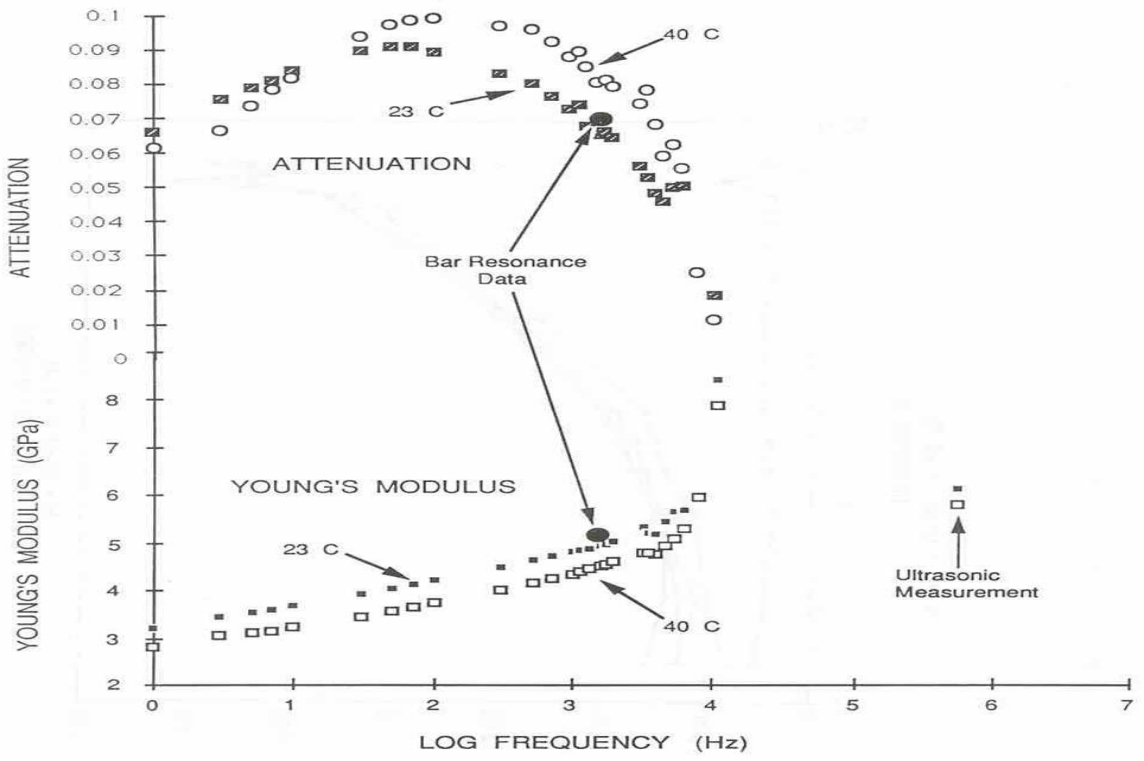

FIG. 3.17. When measurements are made on an isotropic, homogeneous material, the results of the various measurement techniques are in good agreement [Batzle, 2003].

3.3 Ultrasonic measurements

3.3.1 Technique

Pulse transmission technique is used to measure velocities in megahertz frequency range. A generator produces a high voltage pulse (see figure 3.8), which is transformed by the piezoelectric transducer (see figure 3.7) into a high frequency mechanical deformation. This pulse is transmitted along the axis of the cylindrical rock sample. At the receiver end the deformation is converted into an electrical pulse, which is captured by an oscilloscope.

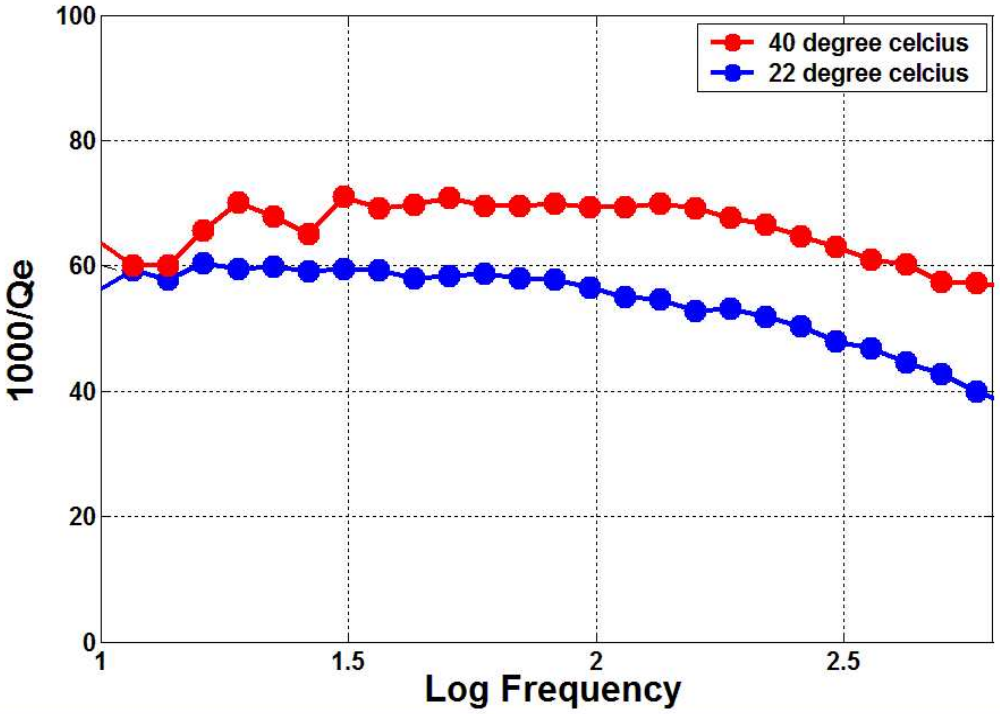

FIG. 3.18. Relaxation peak shift in plexiglass due to change in the viscosity. The $\frac{1}{Q_E}$ values are very close to Spencer's [1981] measurements.

Figure 3.19 shows the recorded ultrasonic signal for compressional and shear waves for a glass sample under 13.8 MPa confining pressure. The travel time is the time difference between the trigger and the first arrival of either the P or the S wave. Recorded S wave also shows the P-wave arrival. The velocity of either mode is the ratio of the length of the sample and the travel time :

$$v = \frac{L}{t} \tag{3.11}$$

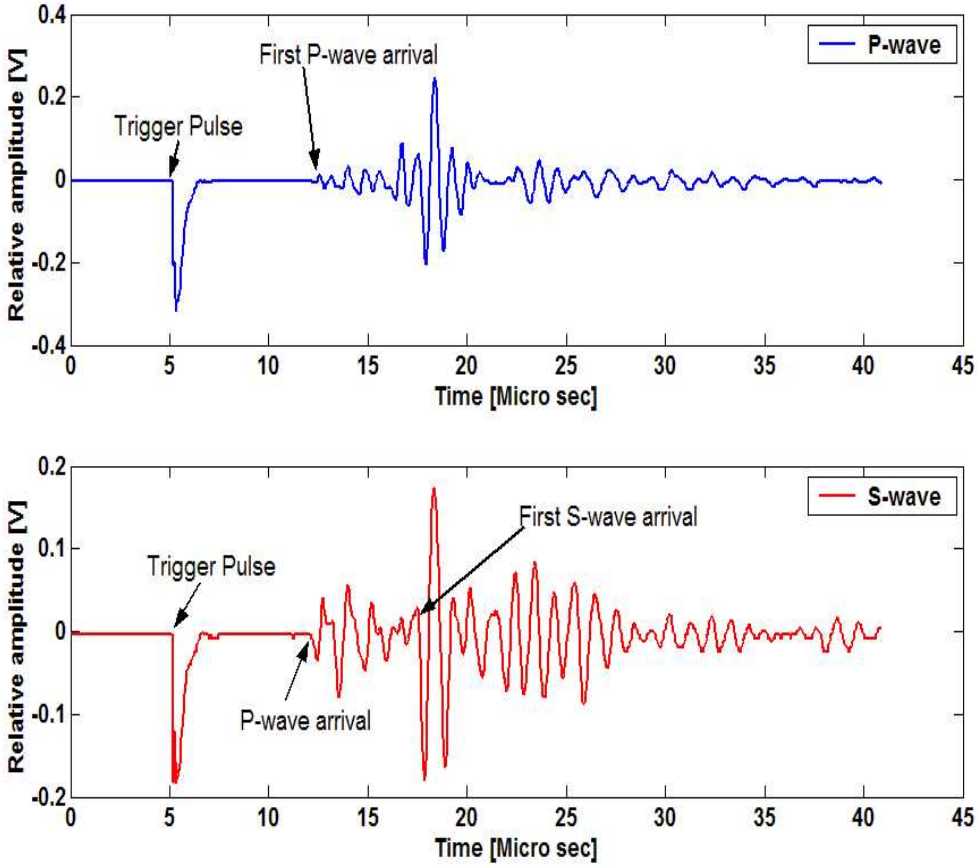

FIG. 3.19. Recorded ultrasonic signal for a glass sample. Top: P-wave arrival. Bottom: S-wave arrival with suppressed P-wave.

The travel path in the aluminum standard is removed from the computation of rock velocity. The dominant frequency of these waves are around 500 kHz. No attenuation was extracted from these ultrasonic measurements.

3.3.2 Assumptions and sources of error

The ultrasonic measurements are based on travel time and length of the sample. length is measured accurately to ± 0.05 mm. The length and volume of the sample can change with changing effective pressure but it is not very significant. The major source of error is the ability to pick the travel time correctly. Also the resolution of signal digitization plays an important role. Both these factors produce a travel time error of around ± 0.05 μs. The maximum absolute error in velocity can be computed by:

$\Delta V = \left\| \frac{\delta v}{\delta t} \right\| \Delta t + \left\| \frac{\delta v}{\delta s} \right\| \Delta s = \left\| -\frac{s}{t^2} \right\| + \left\| \frac{1}{t} \right\| \Delta s$

where Δs is error in length and Δt is error in time. For a 7 cm rock with a velocity of 3500 m/s this results in a velocity error of ± 23 m/s. This error of around 1% is far less than compared to the error in the low-frequency measurements.

For poorly consolidated rocks bad coupling between transducers and the rock, specially at low confining pressures can be a source of error. Bad coupling causes attenuation in the waveform and the amplitudes are poor causing great difficulty in picking the arrival times. Increasing confining pressure usually improves the signal. Picking up the S-wave arrival becomes difficult due to the presence of P-wave interference (see bottom figure 3.19)

3.3.3 Low-frequency versus ultrasonic measurements

Both the measurements are done independently. The low-frequency measurements are in the range of 20-1000 Hz and the ultrasonic measurement is done at 500 kHz. In the results both the set of measurements are plotted where ever it is necessary to compare them. In most cases it is important to measure the velocity dispersion.

Since the attenuation measurement is only done using the low-frequency technique there are no data points for the ultrasonic range.

Inhomogeneity plays an important role in these measurements. While the ultrasonic measurements average the rock properties between the source and the receiver transducer, the low-frequency measurements are point measurements covered by the strain gages.

Chapter 4

SAMPLE CHARACTERIZATION

Sample characterization is very important since it gives the idea about the kind of material we are measuring. First, petrophysical properties were obtained from Geosystems' laboratory. The samples were subjected to analysis by detailed petrographic description and thin section point count technique. Porosity and air permeability are also measured partially by Dr. Han (University of Houston) and by a service lab. Scanning electron microscope (SEM) pictures were taken to have a qualitative measure of the mineral and pore geometry. Clay content is also very important and SEM images are used to identify the presence of clays.

4.1 Plug porosity and permeability

Plug porosity and permeability were measured for the rock samples by Dr. Han (Houston Advanced Research Center (HARC), University of Houston) and service company. The porosity and permeability and grain density are shown in table 4.1.

All the ITF samples come from different depths and the range of porosity is very tight. The reason for this selection was because I needed sandstone samples with similar porosity but, with a wide range of permeability. The measured grain density is a very good indicator of the mineral composition. Pure quartz has a density of 2.65 gm/cc. ITF, Rim, Foxhill's and Merced rock samples are sandstones. Tubb-B and Uvalde are carbonates.

Rock Sample	Porosity	Permeability	Grain Density
Foxhill	22.0%	100 mD	2.48 gm/cc
ITF-11	21.1%	1.8 D	2.64 gm/cc
ITF-43	21.8%	38.2 mD	2.68 gm/cc
ITF-51	22.8%	9.47 mD	2.66 gm/cc
ITF-79	17.2%	178 mD	2.69 gm/cc
Merced Formation	38.0%	8.2 D	2.65 gm/cc
Rim Sandstone	19.0%	348 mD	2.56 gm/cc
Tubb-B	26.3%	92 mD	2.86 gm/cc
Uvalde Carbonate	24.0%	549 mD	2.8 gm/cc

Table 4.1. Plug porosity, air permeability and grain density measured in the laboratory (HARC, Univ of Houston). (mD=$0.987 * 10^{-11} cm^2$)

4.2 Petrographic analysis

A portion of each sample was vacuum impregnated with luminescent blue epoxy resin, mounted on a glass and polished to a thickness of approximately 30 μ m. The sections were stained with a combination of alizarin red S to aid in identification of carbonate minerals. These sections were point counted (250 points) using a petrographic microscope. The point count gives a quantitative information about the texture, composition, cementation and pore geometry. The detailed petrographic description is given below in subsections.

4.2.1 Foxhill's formation

This sandstone is fine to medium grained and has a mean grain size of 0.21 mm (upper fine sand). Grains are subangular to rounded in shape and moderately well sorted. Burial compaction has caused some rotation of grains into a close packing arrangement and resulted in the loss of intergranular porosity. This sandstone sample is moderately quartzose. Monocrystalline quartz is the dominant framework con-

stituent. Small amounts of polycrystalline quartz are also present. Rock fragments are a mixture of chert and gneissic and schistose metamorphic grains. Small amounts sandstone, siltstone, and shale sedimentary rock fragments were also observed. The sample contains 13.2% total cement by volume. Authigenic clay is the dominant clay and is a mixture of kaolinite, chlorite and smectite. Modest amounts of tridymite (a polymorph of SiO2) are also present. Examination using a scanning electron microscope reveals that tridymite is microcrystalline and lines or fills intergranular pores. Tridymite appears similar to clay in thin section and was included with clays in the point count analysis. Clay cements exhibit pore lining and pore filling morphologies. Total porosity from thin section is 24.8% and is dominated by intergranular porosity. Intergranular pores appear moderately well interconnected. Modest amounts of microporosity (8%) are associated with clay minerals and tridyminte. Two color thin section photomicrographs (low and high resolution) for the Foxhill sandstone sample are shown in figures 4.1(a), 4.1(b). This sample was used to study the effect of pore lining/filling clays on velocity dispersion and attenuation.

4.2.2 ITF samples

This group of samples are all sandstones. They exhibit significant variation in grain size and sorting. Mean grain size ranges from 0.13 mm (lower fine sand) to 0.4 mm (upper medium sand). ITF-11 sample exhibits moderate to poor sorting and contains very fine to coarse grain sand. Compaction has caused the loss of intergranular porosity in all the samples. Sandstones are moderately quartzose. There is an abundance of polycrystalline quartz in coarse grained samples (ITF-11 and ITF-79). Small amount of chert and shale rock fragments are also present. These samples contain from 8.8% to 22% total cement volume. There is an abundant silica

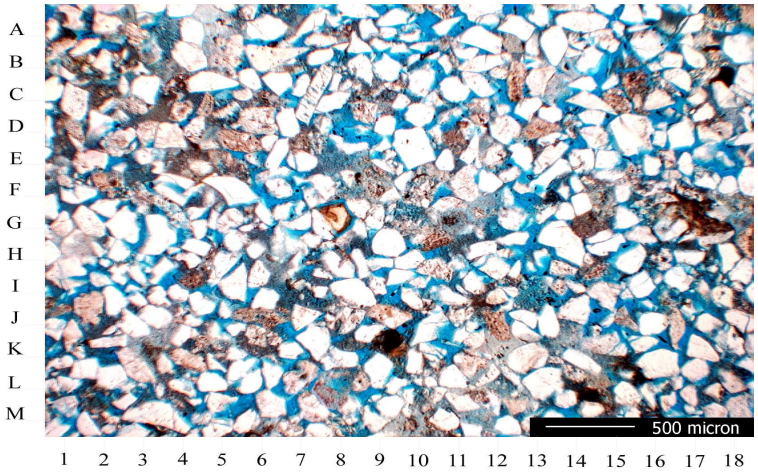

(a) Low magnification survey of a medium grained sandstone. Monocrystalline quartz (H-10) is the most abundant framework component.Some pores are lined to filled by clay minerals (F-12) and tridymite.

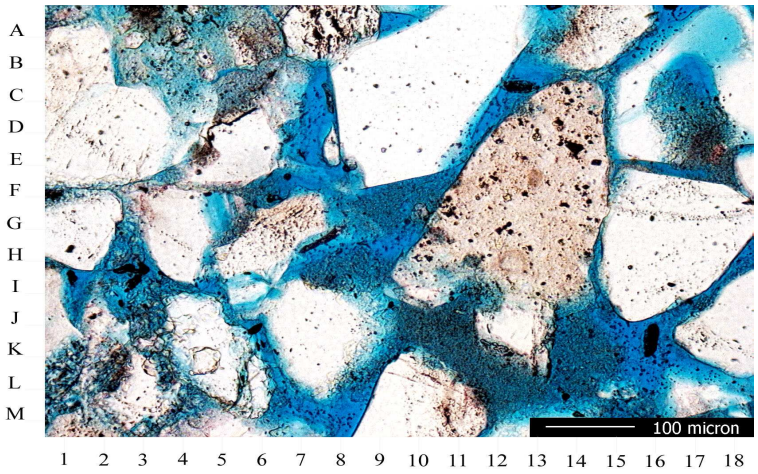

(b) High magnification view of the rock fabric showing well developed intergranular porosity (C-7).

FIG. 4.1. Foxhill's formation: Total thin section porosity is 24.8% which is more than the core plug porosity of 22%.

overgrowths on quartz grains. Dolomite is abundant in three samples (ITF-43, ITF-51, ITF-79). Clay cement is also common and they exist in the form of pore lining chlorite and illite. Small amount of pore filling kaolinite is also present. These sandstones contain 1.6 to 9.6% shale. The shale is in the form of pore lining and pore filling clay and detrital shale/clay. Intergranular porosity is the dominant porosity type in all samples except ITF-51 sample which is dominated by moldic porosity (formed by complete dissolution of unstable framework grains). All samples contain microporosity associated with pore lining and pore filling clays. Two color thin section photomicrographs (low and high resolution) for the ITF samples are shown in figures 4.2(a), 4.2(b), 4.4(a), 4.4(b), 4.5(a), 4.5(b), 4.3(a) and 4.3(b). All the rock samples have similar porosity of around 21% except for ITF-79 which has 17% porosity. The reason why they have different permeability is due to the presence of clay in the pore spaces. These samples were used to understand the effect of permeability on velocity dispersion and attenuation specifically the shift in peak attenuation frequency with change in permeability.

4.2.3 Merced formation

This sample is medium grained sandstone. Average grain size is 0.37 mm (upper medium sand). Grains are angular to subround in shape and moderately well sorted. This sample has experienced very less compaction and is fairly loose sandstone.
This sandstone is mineralogically immature and has unstable mineral grains. Rock fragments include igneous volcanic, igneous, and schistose and gneissic metamorphic grains. Small amount of mica is also present. feldspar is dominated by plagioclase. Heavy mineral grains are also abundant. Quartz is the least abundant of the three major grain types. Thin section porosity is 28% and is dominated by primary in-

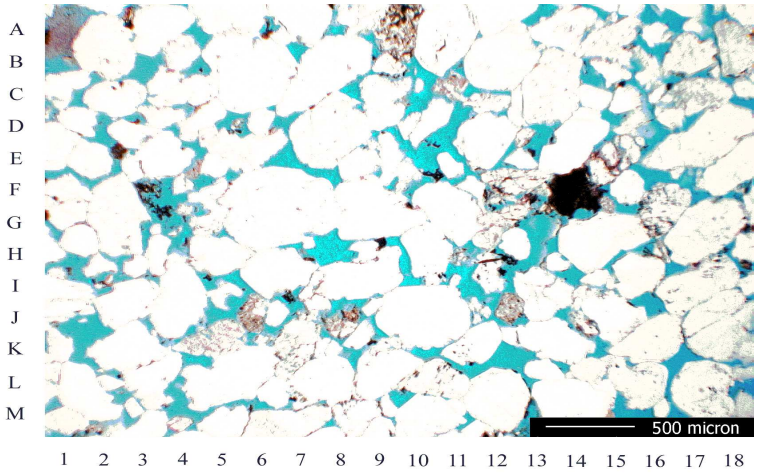

(a) Low magnification survey of a medium grained sandstone. Grains are subangular to round with large variation in grain size and presence of silt sized material.

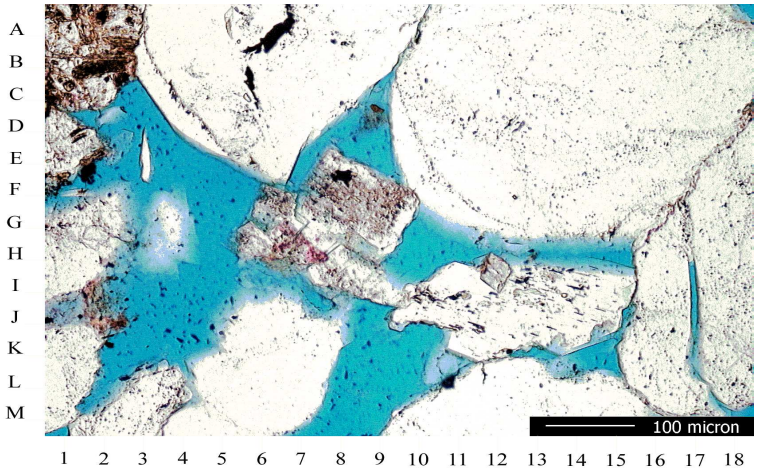

(b) High magnification view of the rock fabric showing well developed intergranular porosity. Small quartz overgrowth (C-4,G-11) partially occlude porosity.

FIG. 4.2. ITF-11 sample: Total thin section porosity=21.1% which is exactly equal to the core plug porosity. Burial depth is 18042 feet.

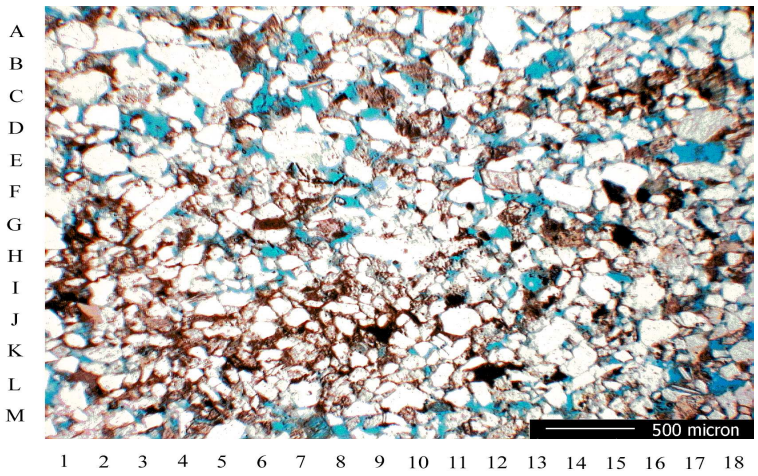

(a) Low magnification view of a fine grained sandstone. Grains are subangular to subround and moderately sorted with a large variation in grain size.

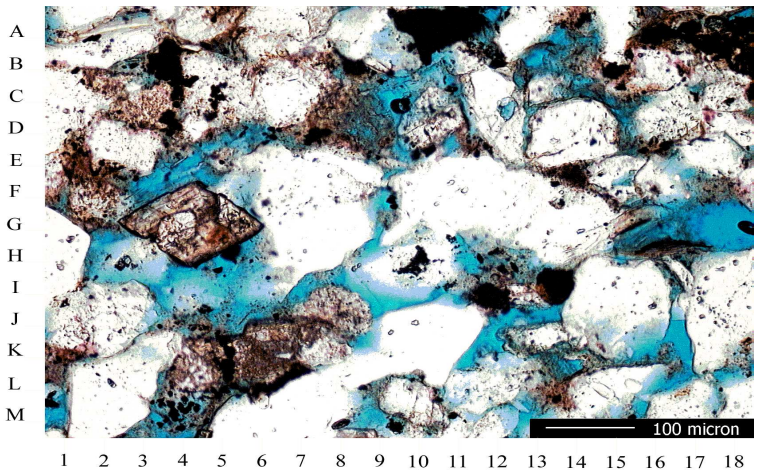

(b) Detailed view of the rock fabric showing the distribution of the framework grains, porosity and cements. Intergranular porosity (I-9) is partially occluded by pore lining clays (C-11).

FIG. 4.3. ITF-43 sample: Total thin section porosity=20% which is less than the core plug porosity. Burial depth is 18257 feet.

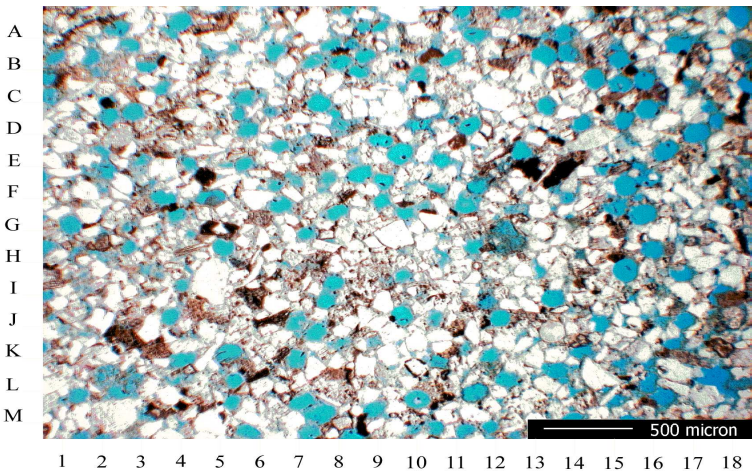

(a) Low magnification view of a very fine to fine grained sandstone. Grains are subangular to round and well sorted. Secondary moldic porosity is the dominant porosity type. This is the reason for very low permeability of this sample.

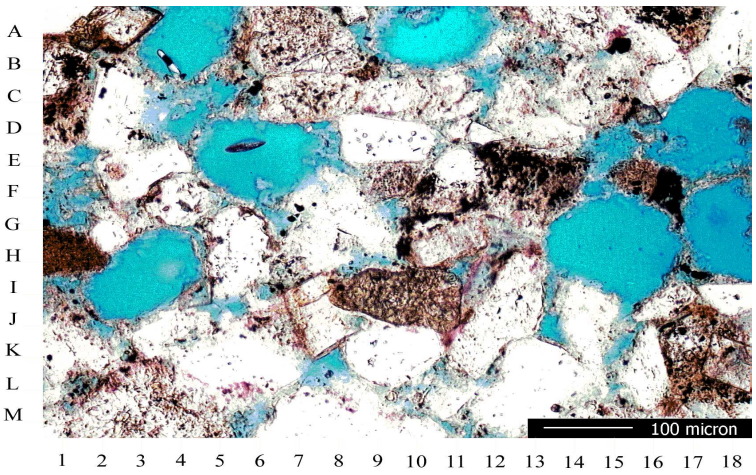

(b) Detailed view of the rock fabric showing framework grains and moldic porosity. Moldic pores (E-6) are poorly interconnected. Clay minerals line moldic and intergranular pores.

FIG. 4.4. ITF-51 sample: Total thin section porosity of 22.8% which is exactly the core plug porosity. Burial depth is 18337 feet.

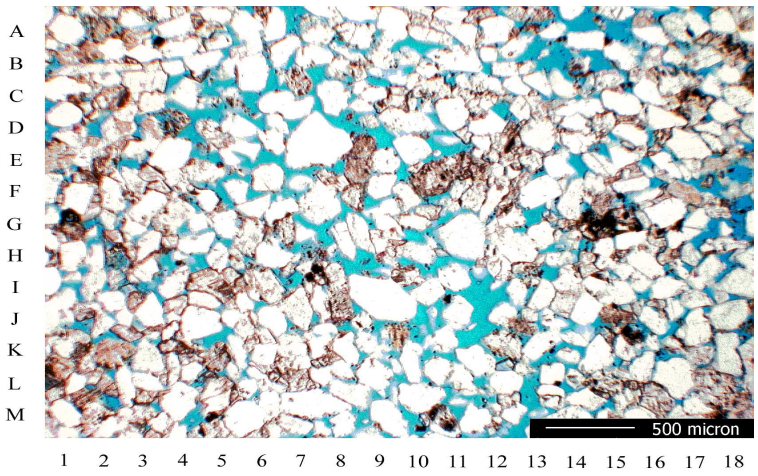

(a) Low magnification view of a fine to medium grained sandstone. Some pores are filled with authegenic dolomite cement (I-5). Pores are well interconnected.

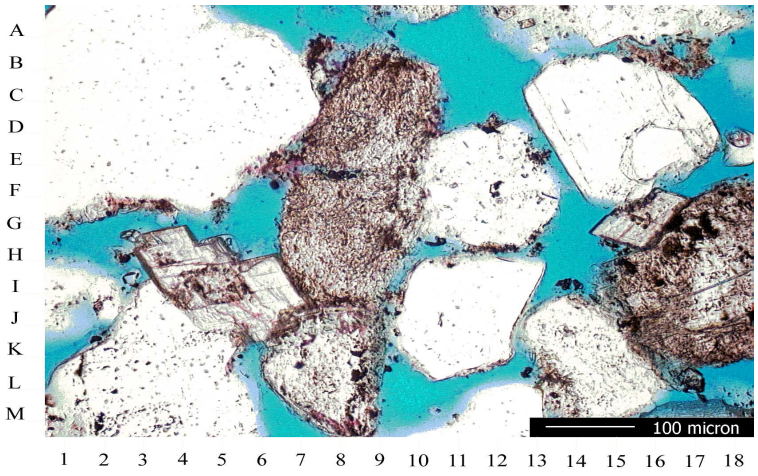

(b) Detailed view of the rock fabric showing grains, porosity and cements. Dolomite occurs as scattered euhedral crystals filling intergranular pore spaces (H-4,H-16).

FIG. 4.5. ITF-79 sample: Total thin section porosity is 22% which is large compared to plug porosity of 17%. Burial depth is 18525 feet.

tergranular porosity type. Two color thin section photomicrographs (low and high resolution) for the Merced sample are shown in figures 4.6(a), 4.6(b). Because the sample is fairly unconsolidated it has very high permeability and the peak relaxation frequency was observed withing the seismic frequency band.

4.2.4 Rim sandstone

The Rim sandstone is medium grained and has a mean grain size of 0.35 mm (upper medium sand). Grains are subangular to subround in shape and moderately sorted. Burial compaction has caused some rotation of grains into a close packing arrangement, resulting in the loss of intergranular porosity and deformation of ductile lithic grains. Monocrystalline quartz is the most abundant framework constituent. Small amounts of polycrystalline quartz are also present. Rock fragments are second in abundance to quartz and are dominated by a mixture of chert and metamorphic rock fragments (gneissic and schistose grains). Small amounts sandstone, siltstone, and limestone sedimentary rock fragments were are also observed. Muscovite and biotite mica are common and relatively abundant. The sample contains 12.4% total cement by volume. Pore lining authigenic clay is common and is dominantly smectite. Calcite cement is also relatively abundant. Calcite fills intergranular pores and also partially replaces framework grains. Two color thin section photomicrographs (low and high resolution) for the Rim sample are shown in figures 4.7(a), 4.7(b). Because of the presence of clays brine was used instead of water to minimize the effect of clays.

4.2.5 Tubb-B carbonate

Tubb-B carbonate belongs to the Smackover formation and it is a dolomite. No detail petrographic analysis has been done for this sample. It has a porosity of 26.3%

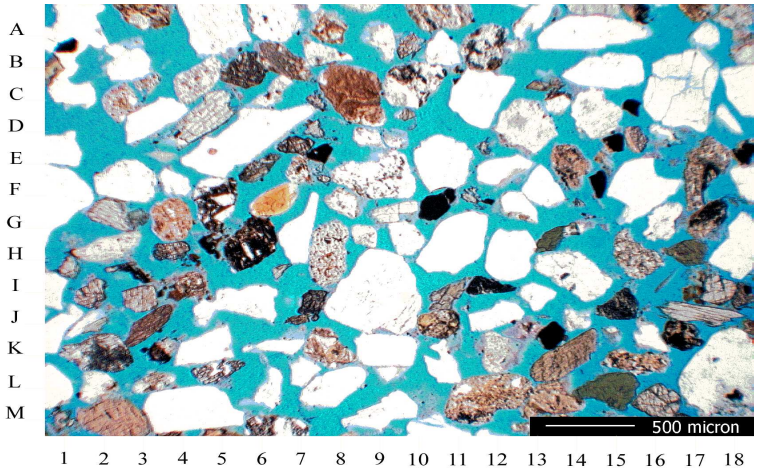

(a) Low magnification view of a fine to medium grained sandstone. Pore lining clay (H-16) is the dominant cement.

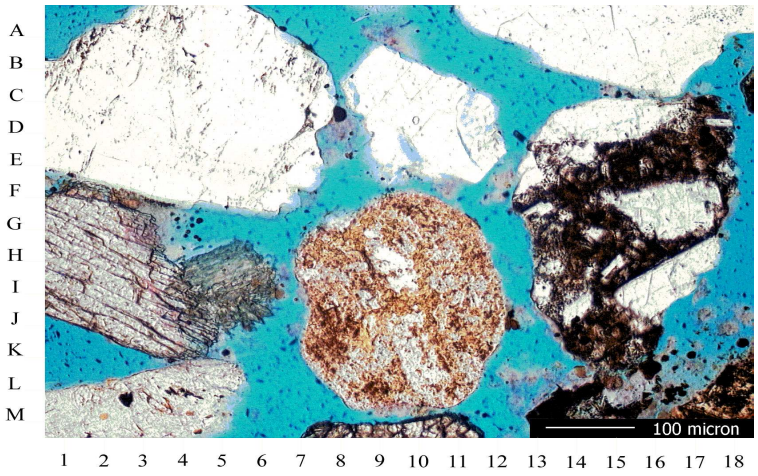

(b) Detailed view of the rock fabric showing well developed intergranular porosity. Heavy mineral grains (H-2) are also relatively abundant.

FIG. 4.6. Merced formation: Total thin section porosity is 28% which is very less compared to plug porosity of 38%.

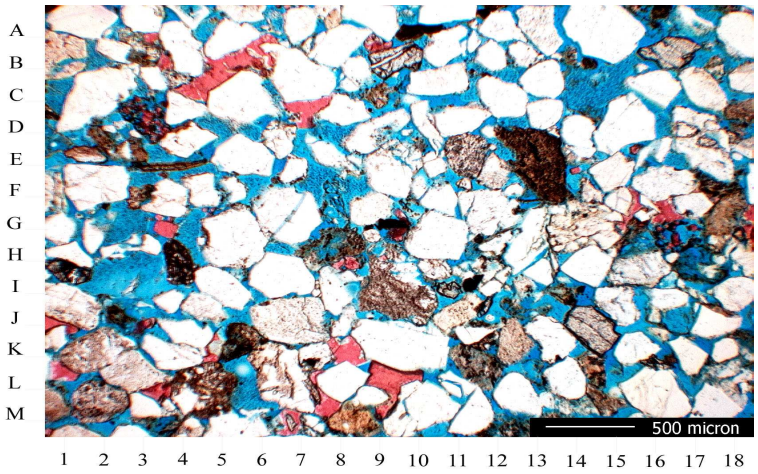

(a) Low magnification view of a medium grained sandstone. This rock is composed of monocrystalline quartz (C-6), Plagioclase and potassium feldspar (D-11, I-1) and modest amounts of rock fragments (C-3, E-13, L-4).

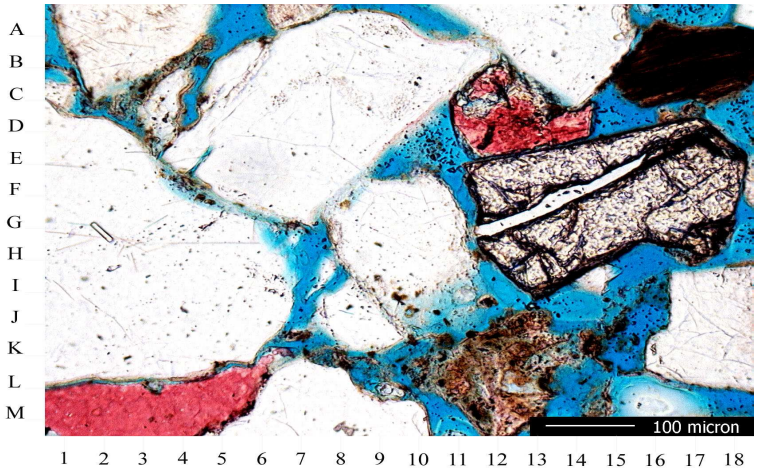

(b) Detailed view of the rock fabric showing framework grains, cements and porosity. Intergranular pores are typically lined by a thin rim of smectite clay (C-3, L-15).

FIG. 4.7. Rim sandstone: Total thin section porosity is 24.4% which is much higher than compared to plug porosity of 19%.

FIG. 4.8. Tubb-B carbonate: Optical thins section. Blue colored areas are the pore spaces.

and air permeability of 92 mD. This rock has large inetrparticle pore spaces which are spherical in shape and non-compliant. Small amount of compliant pores may be present. Figure 4.8 shows the optical thin section image of this sample. Grains are angular to round and the pore shape vary from small intercrack spaces to round vuggy pores. Because of the presence of large percentage of non-compliant pores the sample was used to understand the effect of pressure and saturation on velocity dispersion and attenuation.

4.2.6 Uvalde carbonate

This is a limestone. It is charazterized as a skeletal grainstone to packstone. Skeletal grains are dominated by a mixture of large benthic foraminifera and mollusk fragments. Algal fragments are also present. Interclasts are the only nonskeletal type grains present. Small amount of muddy matrix are scattered throughout the rock fabric. Calcite is the dominant cement. Thin section porosity is 24% and is dominated by interparticle porosity. Lesser amount of intraparticle porosity is present in the form of dissolution pores (voids within skeletal grains). Small amount of moldic porosity is also present. The pores contain very heavy oil which has been extracted and it looks almost like plastic with no flow at room temperature. The viscosity will be measured as a function of temperature. Two color thin section photomicrographs (low and high resolution) for the cleaned Uvalde carbonate sample are shown in figures 4.9(a), 4.9(b). The measurements done on this sample were specially interesting because of the presence of heavy oil present in the pore spaces.

4.3 Scanning Electron Microscopy

Micro structures, grain contact areas, pore geometry and clay structures can be examined in detail using scanning electron microscopy (SEM). Size of an electron beam is very small and this allows better imaging of smaller features. This tool is useful in understanding the influence of microstructure on elastic and viscoelastic properties.

Polished surfaces of rock thin sections were examined. The sections were coated with gold to enhance the conductivity of the sample and reduce charging. Dark areas in the SEM images are the pore spaces where there is high electron absorption, while gray areas are the mineral surfaces. Figure 4.10 shows the SEM image of Foxhill's

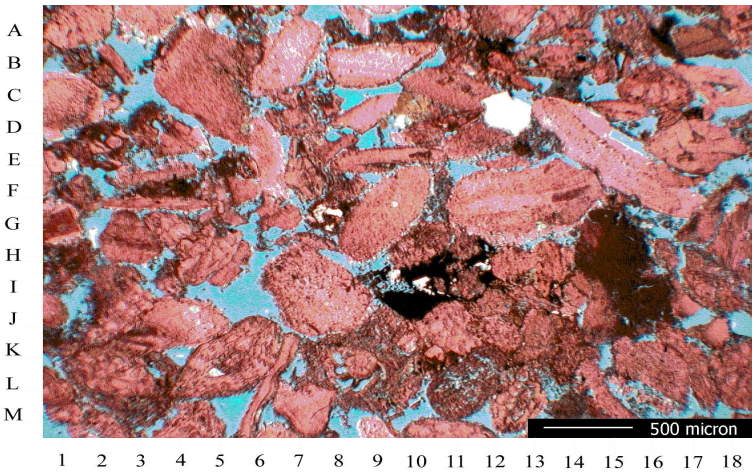

(a) Low magnification view of a skeletal grainstone/packstone. Small amounts of lime mud (F-11) are present within the rock fabric. Interparticle porosity (I-6) is well developed.

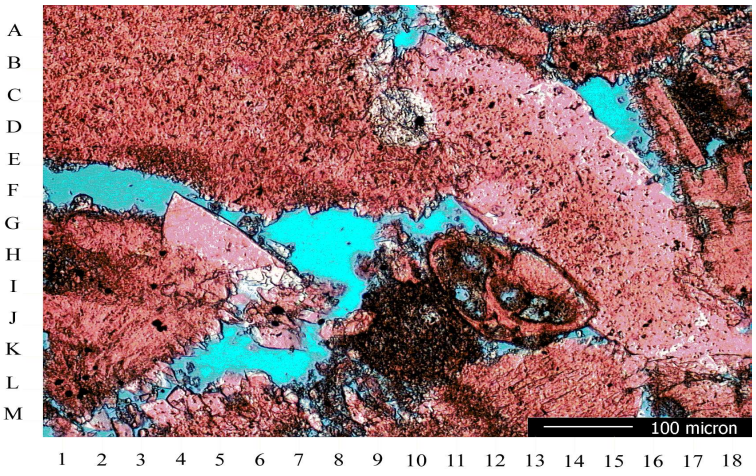

(b) Detailed view of the rock fabric showing skeletal grains, porosity and cement. Foraminifera (I-13), echinoderm fragments (E-14) and mollusk fragments (I-2) are most abundant skeletal grains.

FIG. 4.9. Uvalde Carbonate: Total thin section porosity is 24% which is comparable to plug porosity of 25%. Small amount of microporosity is present within mud matrix.

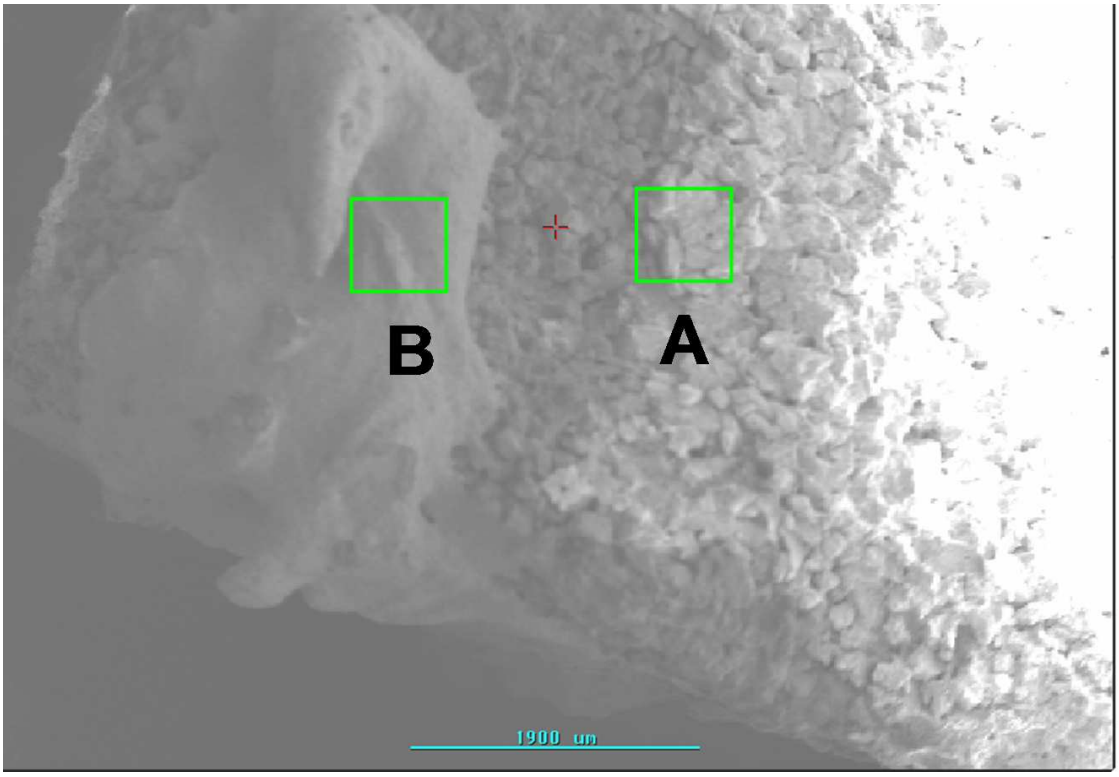

FIG. 4.10. SEM image of Foxhill's formation rock: (A) quartz grains covered with (B) authigenic clays.

formation rock. It can be seen that the quartz grains are covered with authigenic clays. The grains are round to subangular and well sorted.

Figures 4.11(a), 4.11(b), 4.12(a), and 4.12(b) show the SEM images of the ITF samples all with a magnification of 50x. ITF-11 sample has very large pores with coarse quartz grains having very low clay cover. ITF-43 sample has small pores with angular quartz grains. The size of the grains vary a lot and they are covered with clay. ITF-51 sample has very small pores and the quartz grains are covered with clay cement. Most of the pores are plugged with clay. The pore type is moldic and not intergranular. ITF-79 sample has larger intergranular pores compared to ITF-43

sample. The quartz grains are round and clay coated. Pores look very well connected. We know that for a bundle of tubes the permeability is proportional to fourth power of radius of the tubes (K=$\propto r^4$,k=permeability and r=radius). If we consider the pores in the ITF samples as circular pores then the size of the pores causes a large change in the permeability of these rocks even when they have almost the same porosity.

Figures 4.13(a) and 4.13(b) show the SEM images of Merced formation and Rim sandstone respectively. Merced formation has large amount of volcanic inclusions. Rim sandstone has lot of volcanic inclusions with abundant feldspar grains. Quartz is the least abundant of all the mineral. Rim sandstone sample has round to angular quartz grains. The grains are well compacted and this has caused a reduction in intergranular porosity. Altering grains are present where a feldspar grain changes to clay. This sample has significant amount of clay and most of them are smectite. Significant amount of mica is present in this sample. Also, large amount of rock fragments can be seen in the SEM image.

Figures 4.14(a) and 4.14(b) show the SEM images of Tubb-B carbonate and Uvalde carbonate. The pores in Tubb-B sample vary from small cracks to vuggy rounded stiff pores. Dolomite grains are round to angular with a large variation in grain size. Most of the pore spaces are cemented. Uvalde carbonate has skeletal grains which are mainly foraminifera and mollusk. Interclasts are the only non skeletal grains present. Heavy oil is present in the pore spaces and plays a very important role in the velocity and attenuation measurements.

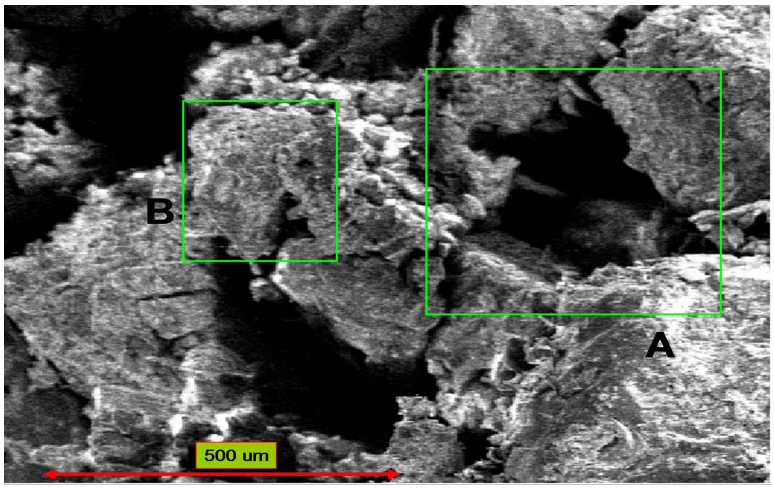

(a) ITF-11 sample: Large pores (A) and low clay covered coarse quartz grains (B) are prominent features of this sample.

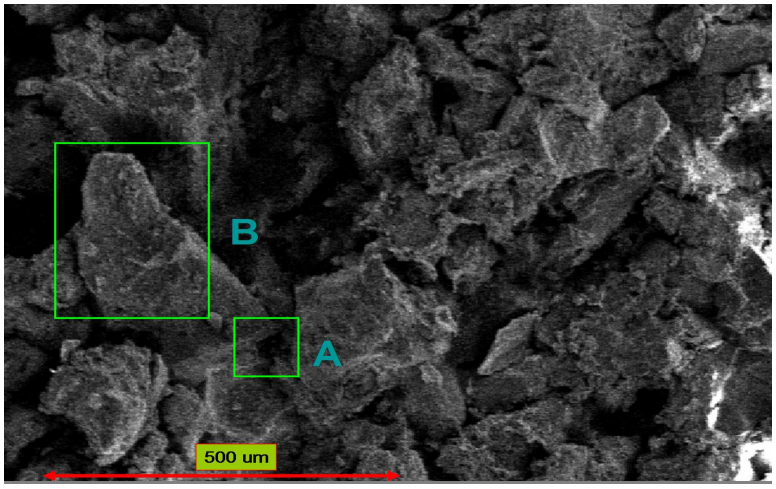

(b) ITF-43 sample: Small pores (A) with angular quartz grains (B) are prominent features of this sample. The grains are coated with clay.

FIG. 4.11. SEM images of ITF-11 and ITF-43 samples.

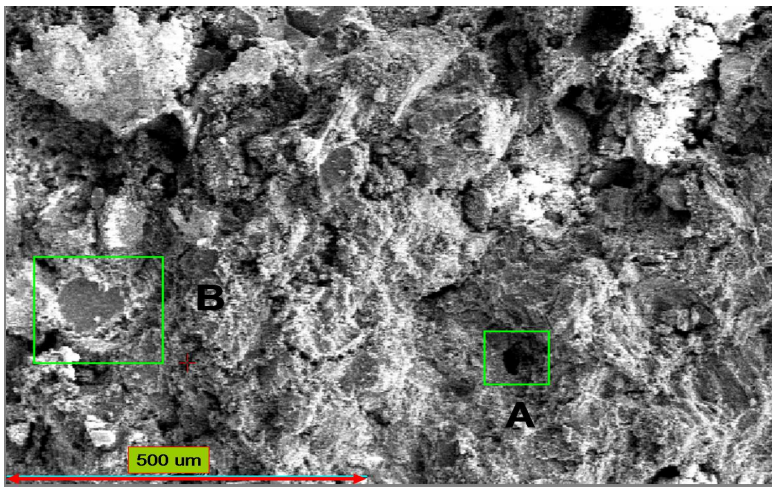

(a) ITF-51 sample: Small moldic pores (A) with clay coated round quartz grains (B)are the prominent features of this sample.

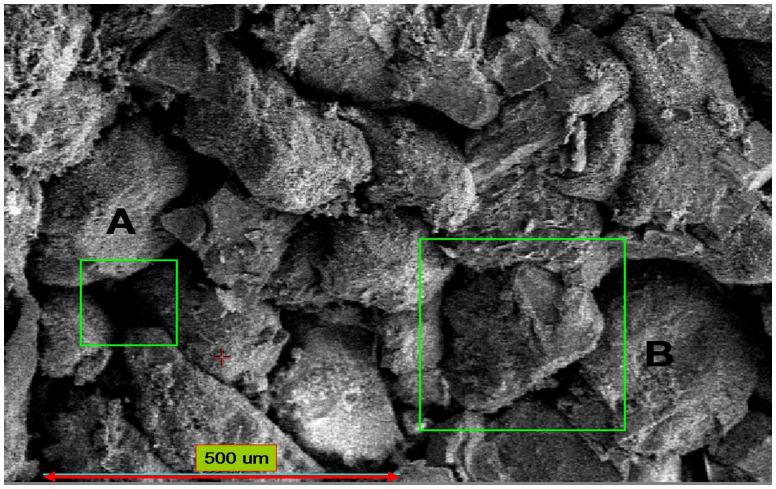

(b) ITF-79 sample: Large intergranular pores (A) and round clay covered quartz grains (B) are the prominent features of this sample.

FIG. 4.12. SEM images of ITF-51 and ITF-79 samples.

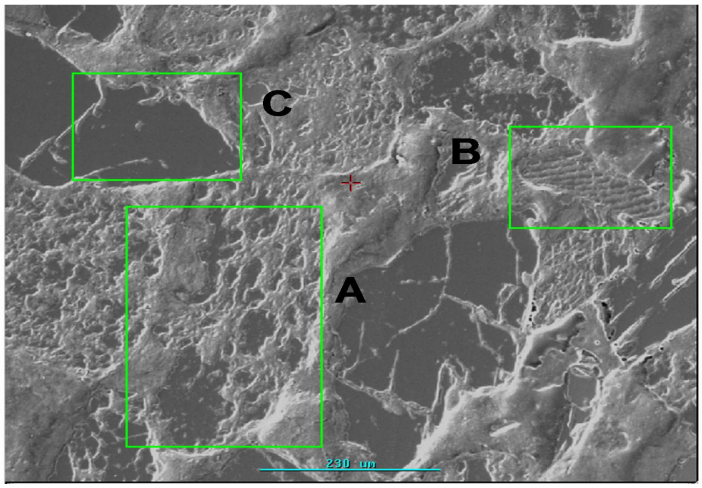

(a) Merced formation: Volcanic inclusions (A), feldspar grains (B) and clean quartz grains (C) are the prominent features of this sample.

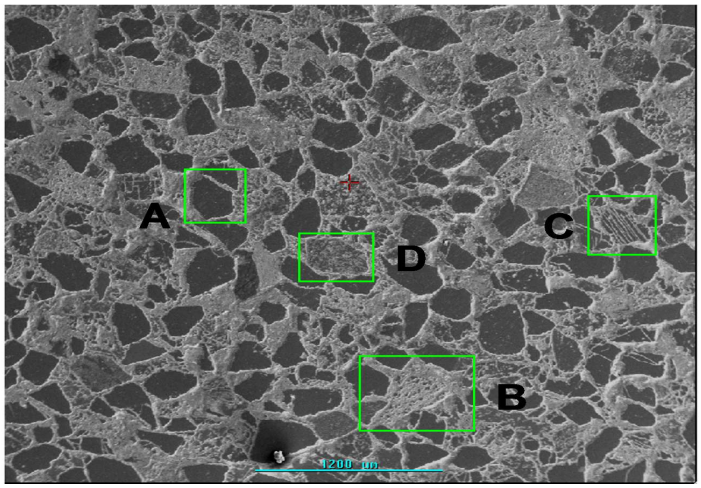

(b) Rim sandstone: Round to angular quartz grain (A). Altering grains which change from feldspar to clay (B). Relatively abundant amount of mica is present (C). Large amount of rock fragments are present (D) and they are second to quartz grains.

FIG. 4.13. SEM images of Merced formation and Rim sandstone samples.

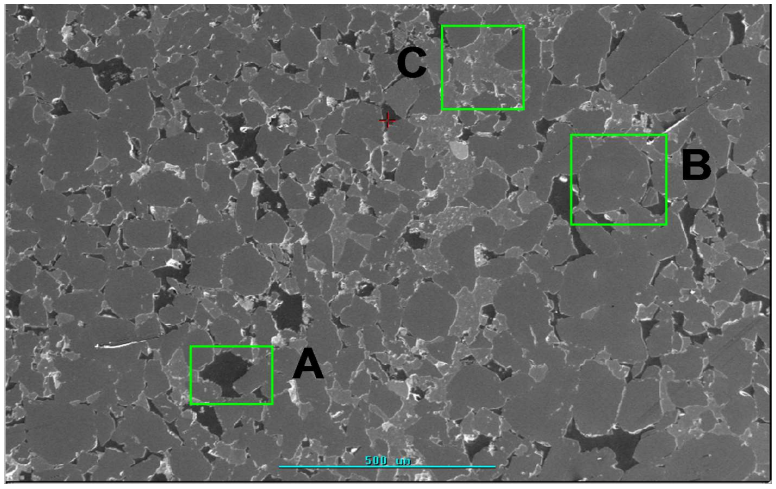

(a) Tubb-B carbonate: Round vuggy (stiff) pores (A). Dolomite grains are round to angular (B). cemented pore spaces (C).

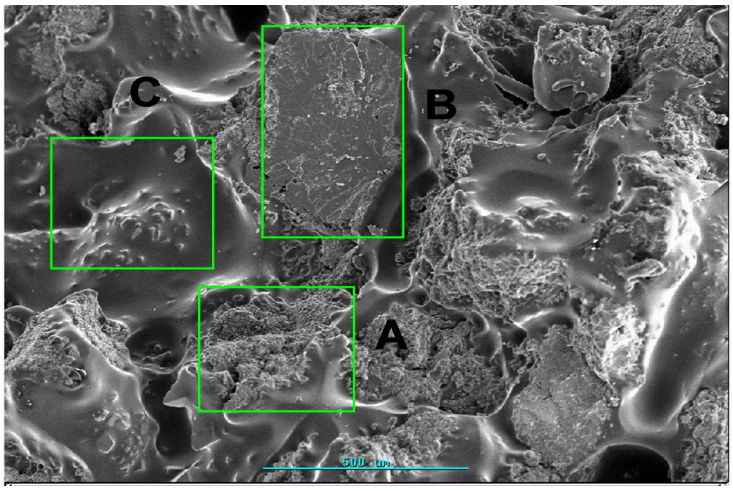

(b) Uvalde carbonate: Skeletal grains (A), mainly foraminifera and mollusk. Interclasts are also present (B). heavy oil is present in the pore spaces (C).

FIG. 4.14. SEM images of Tubb-B and Uvalde carbonate samples.

Chapter 5

MEASUREMENT RESULTS

In this chapter the results of the measurements are presented. This chapter is divided into sections and in each section a particular effect on the velocity dispersion and attenuation is examined with results from some or all of the measured rock samples.

- In the first section the effect of pressure on velocity and attenuation is discussed.
- In the second section effect of saturation is discussed with the idea that the change in saturation state can be detected by attenuation measurements.
- In the third section the effect of fluid mobility on attenuation and velocity dispersion is discussed. The main idea is to understand the dependence on viscosity and rock permeability. For viscosity effect *Uvalde* carbonate rock was measured and for understanding the permeability effect ITF samples were measured which have nearly the same porosity but different permeability.
- In the fourth section the effect of fluid distribution is examined.
- In the fifth section the effect of fluid substitution is discussed.
- In the last section there is a discussion about the effect of clay on velocity and attenuation measurements. Clays play a very important role in these measurements and can alter them to the extent that the expected trends are reversed.

5.1 Effect of pressure

The pressure types used in our experiments are defined as follows:

- Confining pressure, Pc, applied to the exterior of the sample.
- Pore pressure, Pp, controlled independently.
- Differential pressure, Pd= Pc-Pp.
- Effective pressure, Pe=Pc-a*Pp.

Normally, confining pressure increases at about 22.6 KPa/m (1 psi/ft) and pore pressure at about 10.4 KPa/m (0.46 psi/ft). Rock properties are controlled by the effective pressure. If 'a' term is close to unity, which it often is [Wyllie, 1958] then Pe=Pd. for simplicity, we use Pd as the controlling pressure.

With increasing differential pressure the cracks and the compliant pore spaces start to close or grain contacts are made stiffer. The rock becomes stiffer and this results in an increase in moduli and velocities. For the Rim sandstone, figures 5.1(a) and 5.1(b) show the systematic change with frequency in velocity for both the dry and brine saturated cases at different Pd. As expected both the *compressional* and *shear* velocities increase with an increase in differential pressure. Similar effect is seen for ITF-11 sample. Figure 5.2(a) and 5.2(b) show the change in Vp and Vs with increasing differential pressure. The results are shown for various saturation conditions (at 222 Hz) and follow the same trend as with Rim sandstone. The rate of increase is high for lower differential pressures and reduces with increased differential pressure. At very high differential pressure the velocity is almost constant. Similar effect is seen for all other frequencies.

The closure of cracks or compliant pores with pressure causes reduction in intergranular friction. Due to this reason the dry-attenuation decreases with increasing

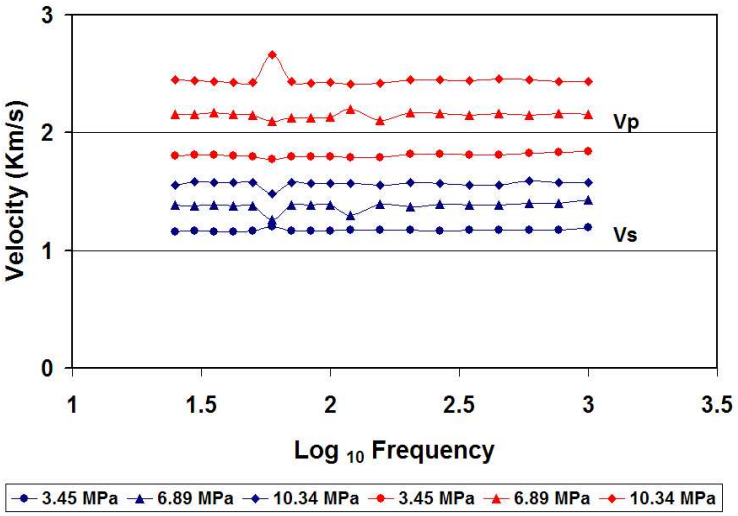

(a) Dry velocities.

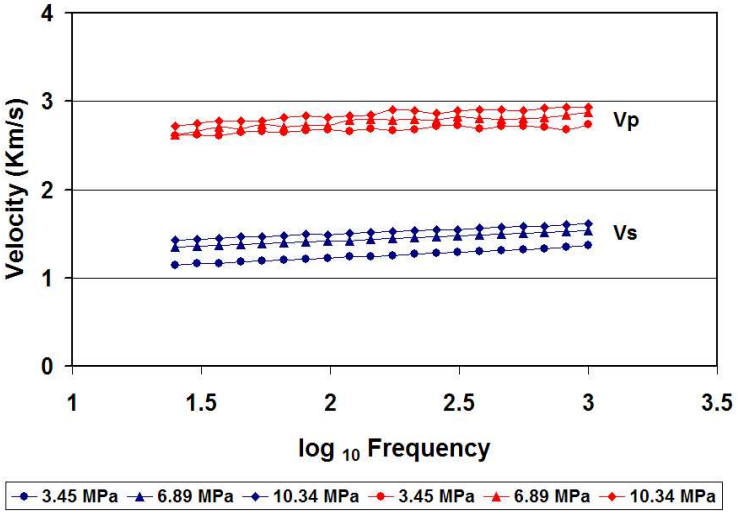

(b) Brine saturated velocities.

FIG. 5.1. Rim Sandstone: Increase in velocity with increasing differential pressure.

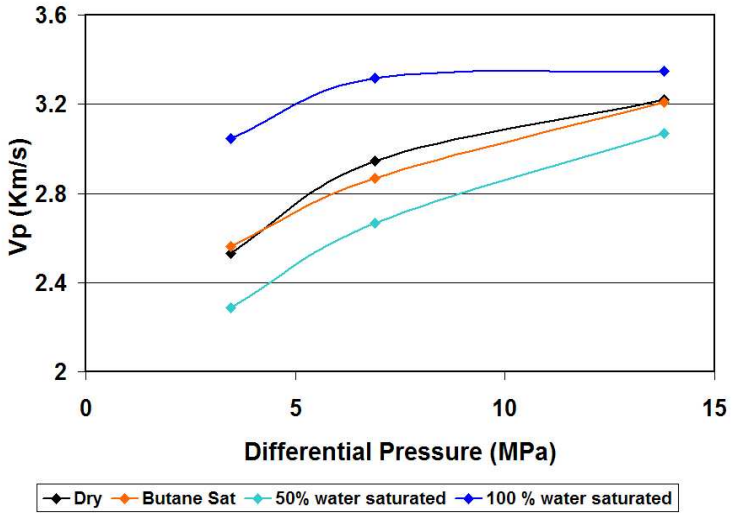

(a) Compressional velocity.

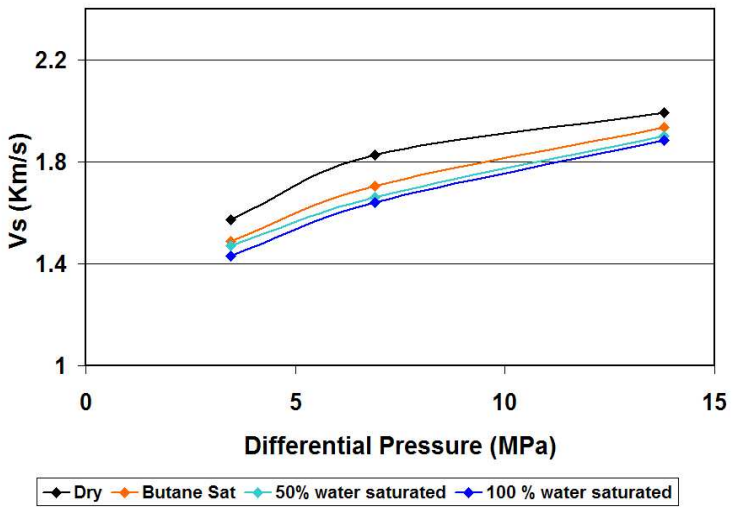

(b) Shear velocity.

FIG. 5.2. ITF-11: Increase in velocity with increasing differential pressure. The driving frequency is 222 Hz.

confining pressure. Also, for saturated rocks attenuation decreases with increasing differential pressure. This has been reported earlier [Gordon and Davis, 1968; Gardner et al., 1964; Winkler and Nur, 1979]. The rate of decrease in attenuation ($\frac{1}{Q}$) is high for lower differential pressures. At higher differential pressures this rate becomes almost constant. Also, the rate of change is different for different saturation conditions. For dry rock it is smaller compared to saturated rock. Figures 5.3(a) and 5.3(b) show the effect of pressure on attenuation for Rim sandstone under different saturation conditions. The driving frequency is 100 Hz but similar effect is seen for all other frequencies measured. Figures (5.4(a), 5.4(b)) show the effect of differential pressure on attenuation for ITF-51 sample under different saturation conditions. The driving frequency is 222 Hz but again similar effect is seen for all other frequencies.

An apparently contradicting influence of differential pressure on velocity is demonstrated by the *Uvalde* carbonate sample. Figures 5.5(a) and 5.5(b) show the effect of confining pressure on compressional and shear velocities for this sample at a low-frequency (25 Hz) and ultrasonic frequency (500 KHz). The velocities decrease with increasing confining pressure and this is contrary to all the results shown before. The reason for this behavior is likely to be a result of the coupling of pore pressure with confining pressure in this particular case. Heavy oil is present in the pore spaces of this carbonate rock. With an increase in confining pressure the pore pressure increases (pore fluid line is kept closed for these measurements). This results in a decrease in differential pressure causing a drop in the velocities. Also when the temperature is increased from 22^0C to 60^0 C the velocity drops significantly. This is because of the drop in the modulus of the heavy oil with an increase in temperature and also increase in pore pressure with the temperature increase due to the expansion of the oil. It should also be mentioned that the rate of change is very small compared to the

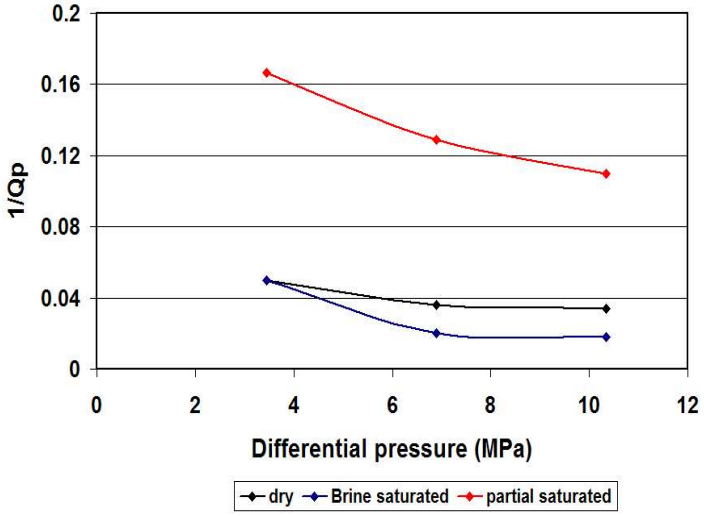

(a) Compressional attenuation coefficient.

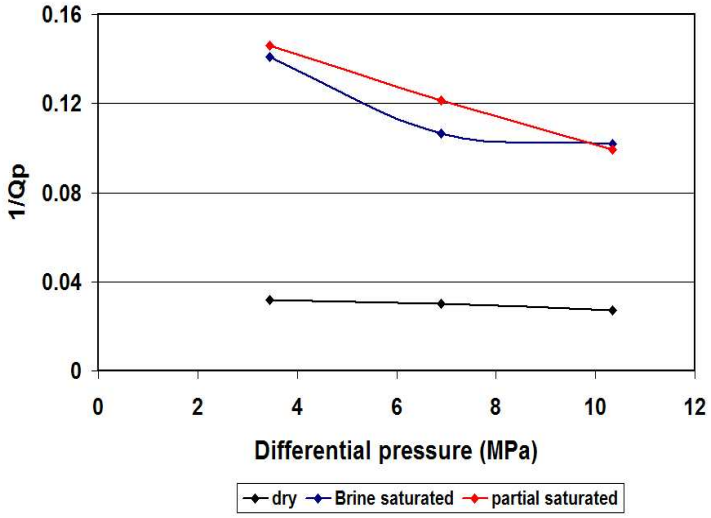

(b) Shear attenuation coefficient.

FIG. 5.3. Rim Sandstone: Decrease in attenuation with increasing differential pressure. The driving frequency is 100Hz.

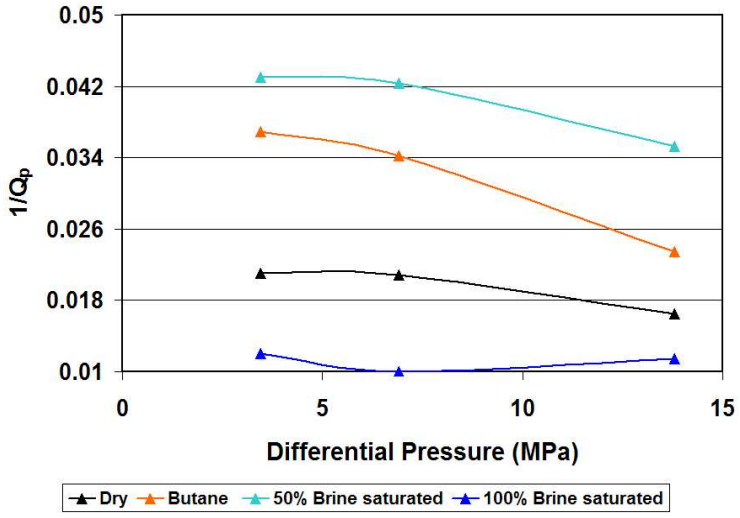

(a) Compressional attenuation coefficient.

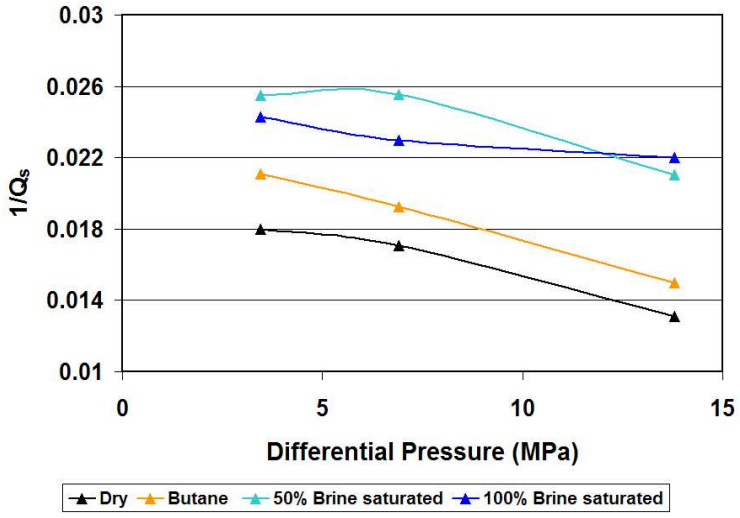

(b) Shear attenuation coefficient.

FIG. 5.4. ITF-51: Decrease in attenuation with increasing differential pressure. The driving frequency is 222Hz.

sandstone samples. The attenuation values show the expected result as they decrease with increasing confining pressure (figures 5.6(a) and 5.6(b)). The rate of change is higher for high temperature measurements. Increase in temperature causes drop in viscosity, resulting in higher fluid mobility and high attenuation values.

The effect of differential pressure on velocity and attenuation for *Tubb-B* carbonate sample showed the result of stiff pore space. Figure 5.7(a) and 5.7(b) show the effect of varying differential pressure on velocity and attenuation respectively. It can be seen from these two plots that pressure has very little effect on both velocity and attenuation for dry condition. This is because majority of the pores in this rock are incompressible (round noncompliant pores, see Chapter 4). Pressure can not close these pores with the result that there is no significant increase in bulk modulus or velocity. Alternatively, one could consider this due to stiff grain contacts. These contacts are not affected very much by pressure increase as they are very well cemented due to which there is no significant decrease in friction related attenuation (see the SEM image of Tubb-B in Chapter 4).

5.2 Effect of saturation

The saturation conditions discussed in this section can be defined as follows:

- Dry= room dry i.e. pores are empty except for water coating due to humidity.
- Partial saturation= usually the fraction refers to the portion of the pores filled with liquid. Unless otherwise specified, the remainder is filled with vapor.
- Fully saturated= the entire pore volume is filled with a fluid and the pore fluid lines are closed.

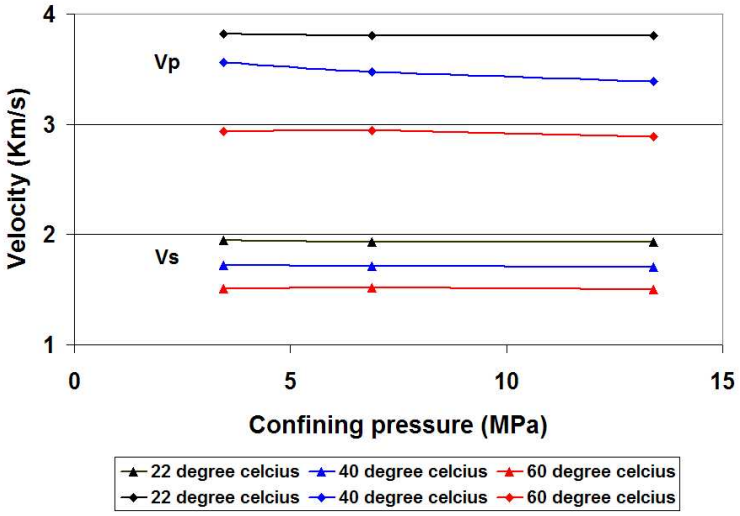

(a) Low-frequency (25 Hz).

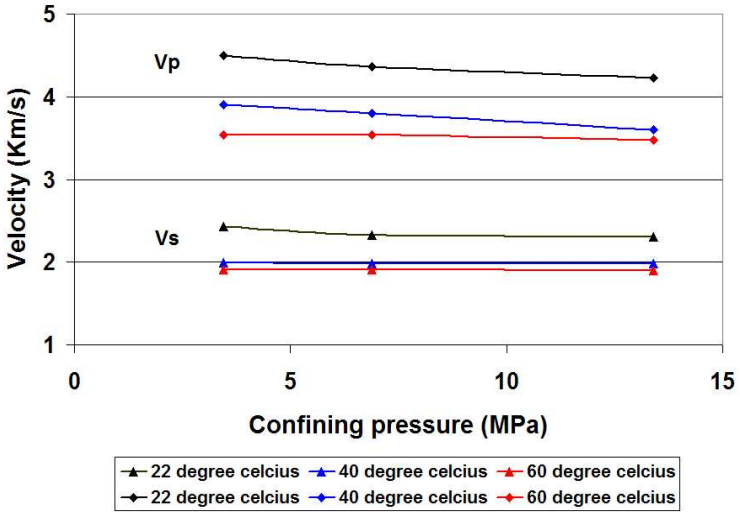

(b) Ultrasonic (500 KHz).

FIG. 5.5. Uvalde carbonate saturated with heavy oil: Decrease in velocity with increasing confining pressure due to the coupling of the pore pressure to the confining pressure (decreasing differential pressure).

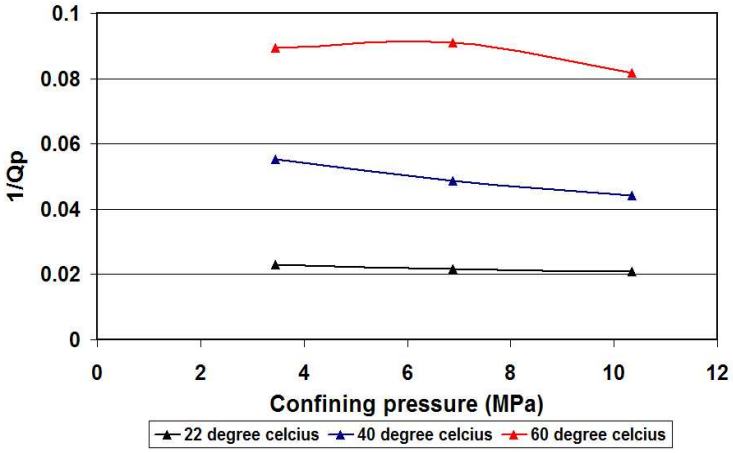

(a) Compressional attenuation coefficient.

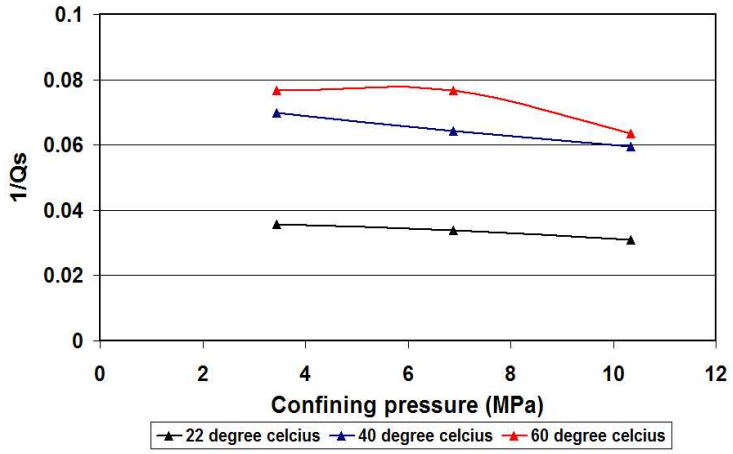

(b) Shear attenuation coefficient.

FIG. 5.6. Uvalde carbonate saturated with heavy oil: Decrease in attenuation with increasing confining pressure. The driving frequency is 25 Hz.

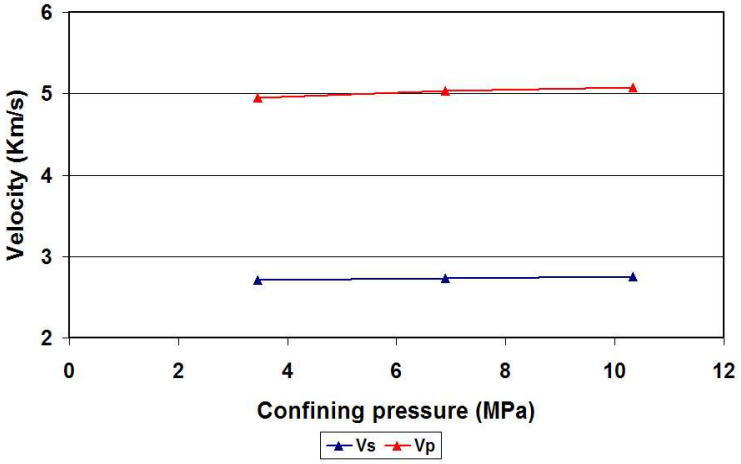

(a) Compressional and shear velocity.

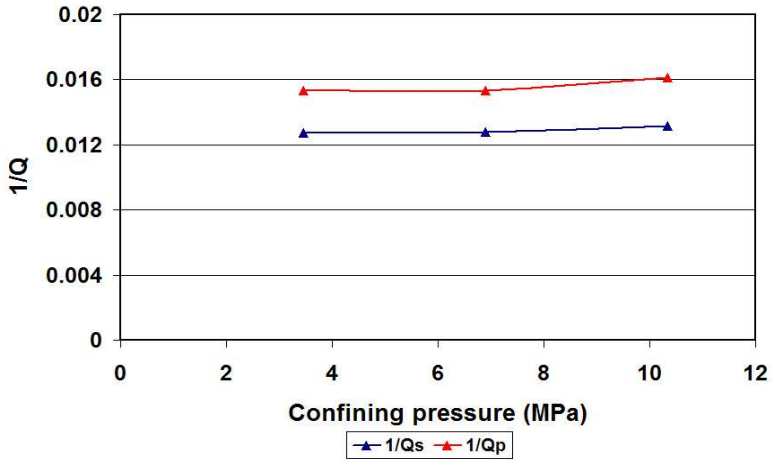

(b) Compressional and shear attenuation coefficient.

FIG. 5.7. Tubb-B carbonate: A small effect of differential pressure on velocity and attenuation coefficient probably due to non-compliant pores. Driving frequency is 25 Hz.

Partial and full saturation attenuation measurements become very important because they can help in estimating the saturation state of a rock. It is also important to distinguish between different fluid types and also between economic and non-economic gas. There are several theories that propose attenuation mechanisms at partial and full saturation. Mavko and Nur [1979] use a model where liquids move in response to compression in cracks as waves pass through the rock. Kjartansson and Delinger [1977] use adiabatic heating of the gaseous phase of the liquid due to compression, which causes irreversible flow of heat into the rock and pore fluid. These mechanisms predict that attenuation should increase with saturation. Higher saturation means more bulk flow of fluid inside pore spaces requiring more energy to be supplied by the propagating wave resulting in increased attenuation values.

The different modes of attenuation are constrained to follow any one of three inequalities given below [Winkler and Nur, 1979], which are derived from the mathematical relations between different inelastic moduli.

$$\frac{1}{Q_S} < \frac{1}{Q_E} < \frac{1}{Q_P} < \frac{1}{Q_K} \; (low \; \frac{V_P}{V_S} \; ratio) \tag{5.1}$$

$$\frac{1}{Q_S} = \frac{1}{Q_E} = \frac{1}{Q_P} = \frac{1}{Q_K} \tag{5.2}$$

$$\frac{1}{Q_S} > \frac{1}{Q_E} > \frac{1}{Q_P} > \frac{1}{Q_K} \; (high \; \frac{V_P}{V_S} \; ratio) \tag{5.3}$$

The relation are general, but the relevant one will change depending on the state of saturation. For partial saturation (low $low\frac{V_P}{V_S}ratio$ or small Poisson's ratio) the modes follow the first inequality (equation 5.1) which means higher compressional attenuation than shear. Compressional loss is almost twice as much as shear loss for

partial saturated rocks. At full saturation (high $\frac{V_P}{V_S}$ ratio or large Poisson's ratio) the *bulk* and *compressional* attenuation drop considerably because there is no compliant space where the fluid can move. Shear attenuation continues to increase, and at full saturation it is three times as large as *compressional*. In this case the different modes follow the third inequality (equation 5.3). Thus, depending on the saturation state of the rock, the relationship between different modes of attenuation changes. This change can be seen in the results from Rim sandstone and ITF-51 samples shown in figures 5.8(a), 5.8(b), 5.9(a) and 5.9(b).

The boundary condition of the pore fluid system plays an important role (see fig 3.3). By opening and closing the micro valve we can simulate open and close boundary conditions respectively. Figure 5.10(a) and 5.10(b) show the relation between different modes of attenuation for saturated open boundary measurements done on Rim sandstone and ITF-51 sample. With open valves, for both Rim sandstone and ITF-51 sample the low-frequencies ($\leq$ 100 Hz) behave as if the rock is partially saturated even when the rock is completely filled with brine (modes of attenuation follow the first inequality (equation 5.1)). The specific range of low-frequency depends on the rock and fluid properties. The reason for this behavior is that at low frequencies the open boundary allows fluid to move in and out of the sample and equilibrate with the surrounding pressure. This can only happen at low-frequencies, which allow enough time for the fluid to equilibrate with the surrounding pressure. At high frequencies, there is not enough time for the fluid to come into equilibrium with the external pore fluid system.

Open versus closed boundaries have an effect on compressional velocity too. Figure 5.11(a) compares the open versus close boundary velocities for Foxhill's sandstone. For low-frequencies ($\leq$ 100 Hz) the open boundary velocity is less than close bound-

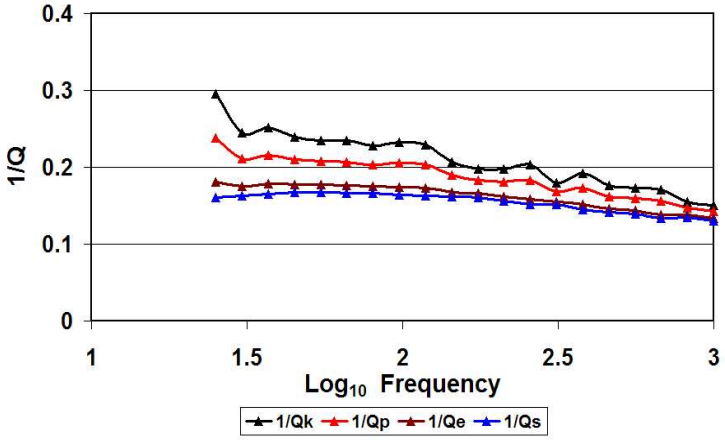

(a) 1/Q at partial brine saturation (50%).

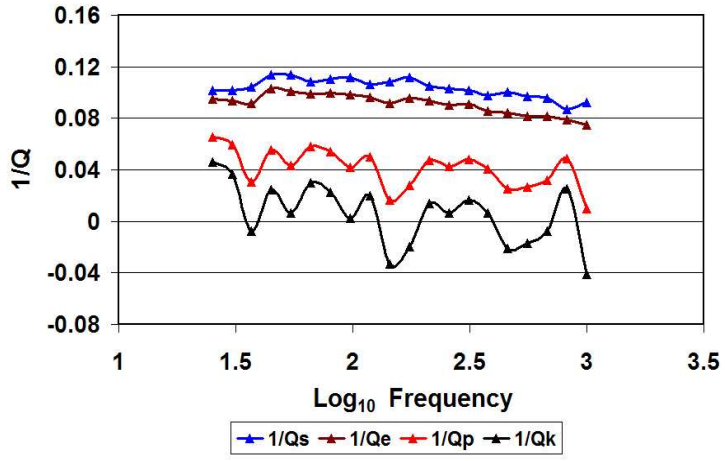

(b) 1/Q at full brine saturation (valve is closed).

FIG. 5.8. Rim sandstone: Relation between different modes of attenuation for partially(50%)and fully brine saturated case. Differential pressure=6.89 MPa.

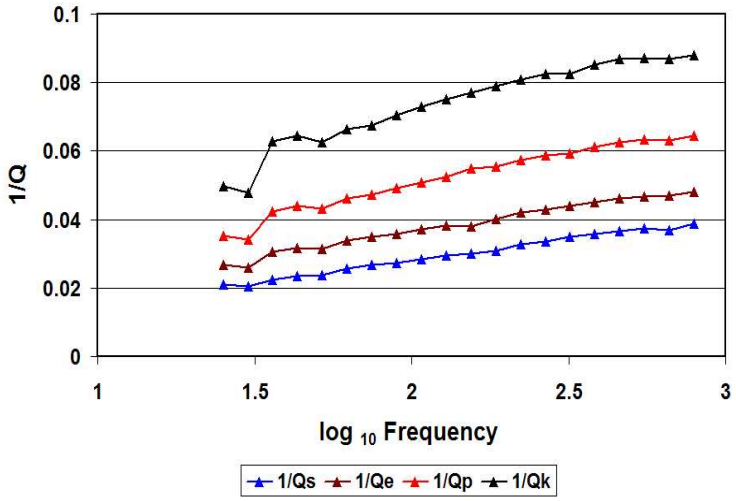

(a) 1/Q at partial brine saturation (50%).

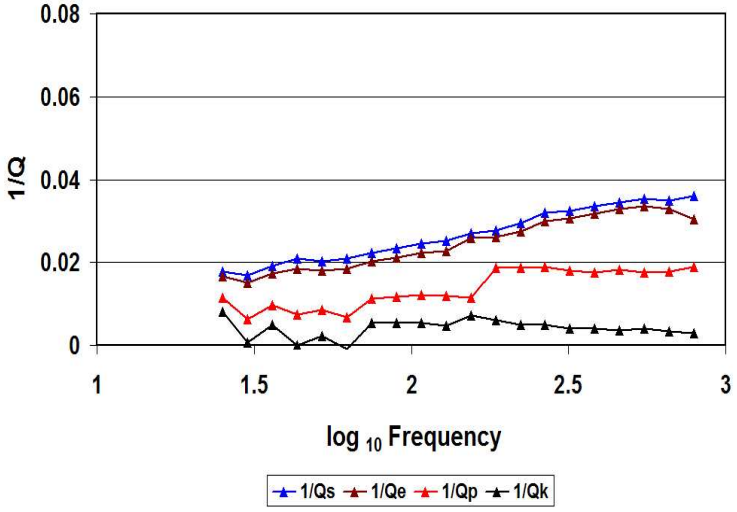

(b) 1/Q at full brine saturation (valve is closed).

FIG. 5.9. ITF-51: Relation between different modes of attenuation for partially(50%) and fully brine saturated case. Differential pressure=6.89 MPa.

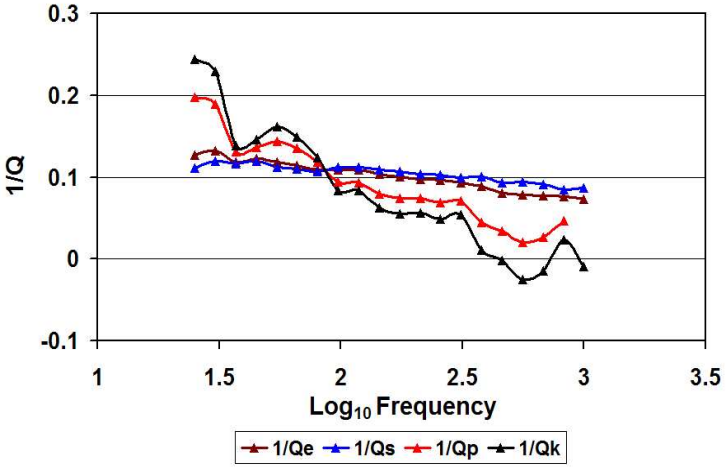

(a) Rim sandstone: 1/Q at full brine saturation (valve open).

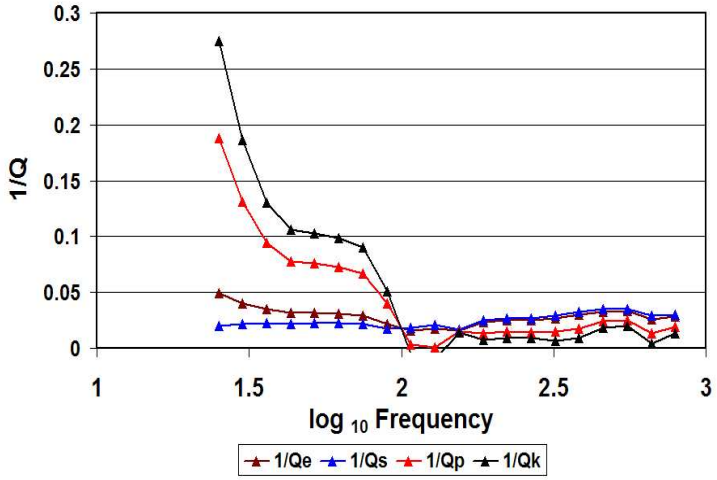

(b) ITF-51: 1/Q at full brine saturation (valve open).

FIG. 5.10. Relation between different modes of attenuation for full brine saturated rocks (valve open). Differential pressure=6.89 MPa.

ary velocity. This is again due to the flow of fluid and pressure equilibration. This is similar to the drained condition where the effective fluid bulk modulus becomes zero and does not contribute to the saturated rock bulk modulus. In fact, due to the density effect, the open boundary velocity at low frequencies is less than the dry velocity (modulus remains the same as dry rock but density increases [Hofmann,2001]). This is shown in figure 5.11(b).

The effect of open or close boundary conditions on attenuation is opposite to that of velocity. For open boundary case the fluid flow across the boundary causes an increase in attenuation for low-frequencies. For higher frequencies, there is not enough time for the fluid to to move across the boundary and this effect is not always visible. In figure 5.12(a) the difference between open and close boundary Young's attenuation is shown for Foxhill's sandstone. At 3.15 Hz both the open and close attenuation values are the same. The reason for this can not be explained at this point. In figure 5.12(b) the effect of open versus close boundary on Young's and shear attenuation for Rim sandstone sample is compared. Shear attenuation is not affected by fluid flow and thus the values for open and close boundaries are identical within the limits of experimental error.

The *compressional* velocities at different saturations are often estimated using *effective fluid model* [Domenico, 1977; Mochizuki, 1982] which is given as:

$$\frac{1}{K_{eff}} = \frac{x}{K_A} + \frac{(1-x)}{K_B} \tag{5.4}$$

where K_{eff} is the effective fluid modulus of a mixture of two fluids A and B with bulk moduli K_A and K_B respectively. The volume fraction of fluid A is x and B is (1-x). These velocities usually are not consistent with the ultrasonic measurements done in the laboratory. So, if we use measured ultrasonic laboratory velocity to predict the

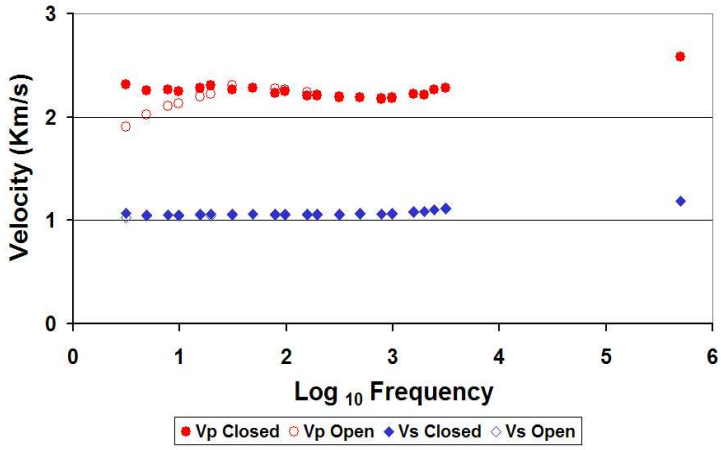

(a) Foxhill's sandstone: Velocity comparison for open versus close boundary conditions. Differential pressure=10.34 MPa.

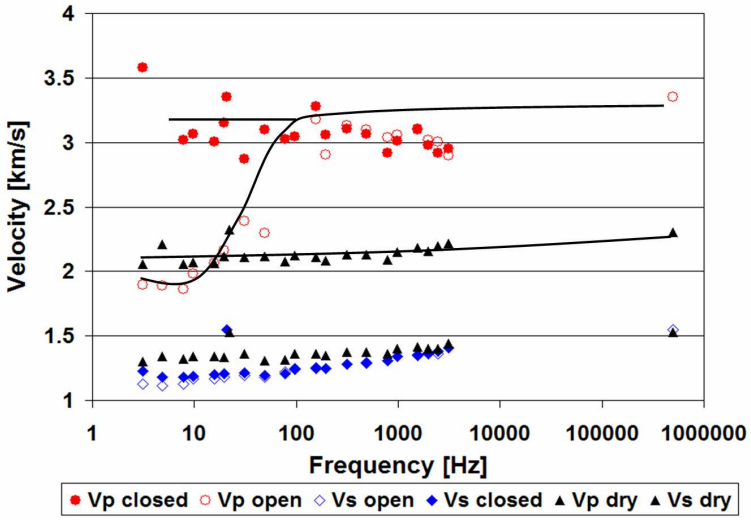

(b) Rim sandstone: Velocity comparison for open versus close boundary conditions. Differential pressure=6.89 MPa.(Courtesy: Hofmann, 2003).

FIG. 5.11. Velocity comparison for open versus close boundary conditions.

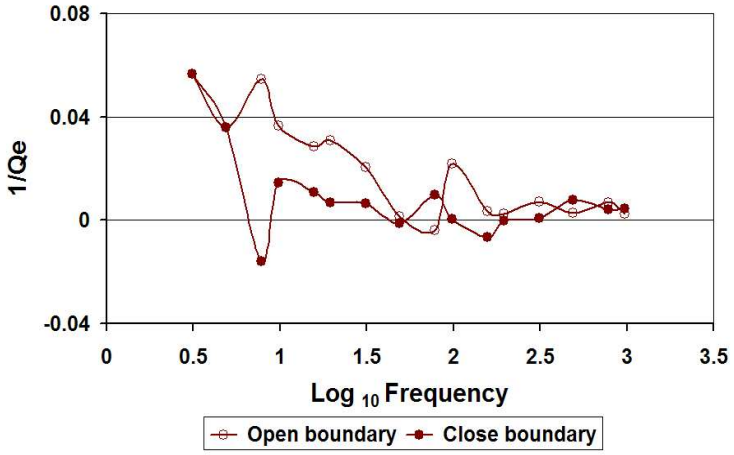

(a) Foxhill's sandstone: Attenuation comparison for open versus close boundary conditions. Differential pressure=10.34 MPa.

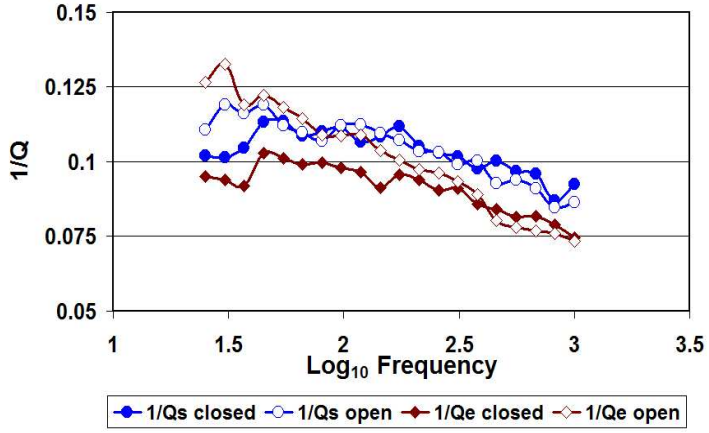

(b) Rim sandstone: 1/Qe and 1/Qs comparison for open versus close boundary conditions. Differential pressure=6.89 MPa.

FIG. 5.12. Attenuation comparison for open versus close boundary conditions.

effect of partial saturation in seismic data there will be errors. Figure 5.13 shows the ultrasonic ($\sim 10^5$ Hz) and low-frequency velocities for ITF-51 sample. We see a 21% maximum error between ultrasonic and seismic velocity.

The difference can be explained using the *gas pocket model* [White, 1975] and the *squirt flow model* [Mavko and Jizba, 1991]. In the *gas pocket model* separate gas and liquid phases are present in regular cubic lattice geometry. In the *squirt/local flow* there is flow of liquid from region of high pressure to low-pressure (gas). Both these models allow liquid movement and pressure equilibration between the liquid and the gas phase as waves propagate through the rock. At low-frequencies the liquid has enough time to equilibrate with the gas phase and thus the compressional velocity drops as compared with the dry velocity due to density effect. At ultrasonic frequencies, there is no equilibration due to lack of time, which results in stiffening of the rock-fluid matrix due to unrelaxed fluid pressure.

Gassmann substitution is used (figure 5.13) to compute the fully saturated velocity given the dry velocity and brine property. If we use *effective fluid modulus* (equation 5.1) then according to Gassmann [1951] the partial saturated rock should have same bulk modulus as a dry rock. Only at full saturation the effective fluid bulk modulus increases in turn increasing the effective modulus of the saturated rock. Thus, at partial saturations, the rock compressional velocity drops with increase in saturation due to density effect and at 100% saturation it increases due to increase in effective bulk modulus. The shear velocity monotonically decreases due to density effect as fluids do not affect the shear modulus [Gassmann, 1951; Biot, 1956].

The change in attenuation with increasing brine saturation is shown in figures 5.14(a) and 5.14(b) for the ITF-51 sample. With a slight amount of brine added both the compressional and shear attenuation increases. As brine is injected a few mono-

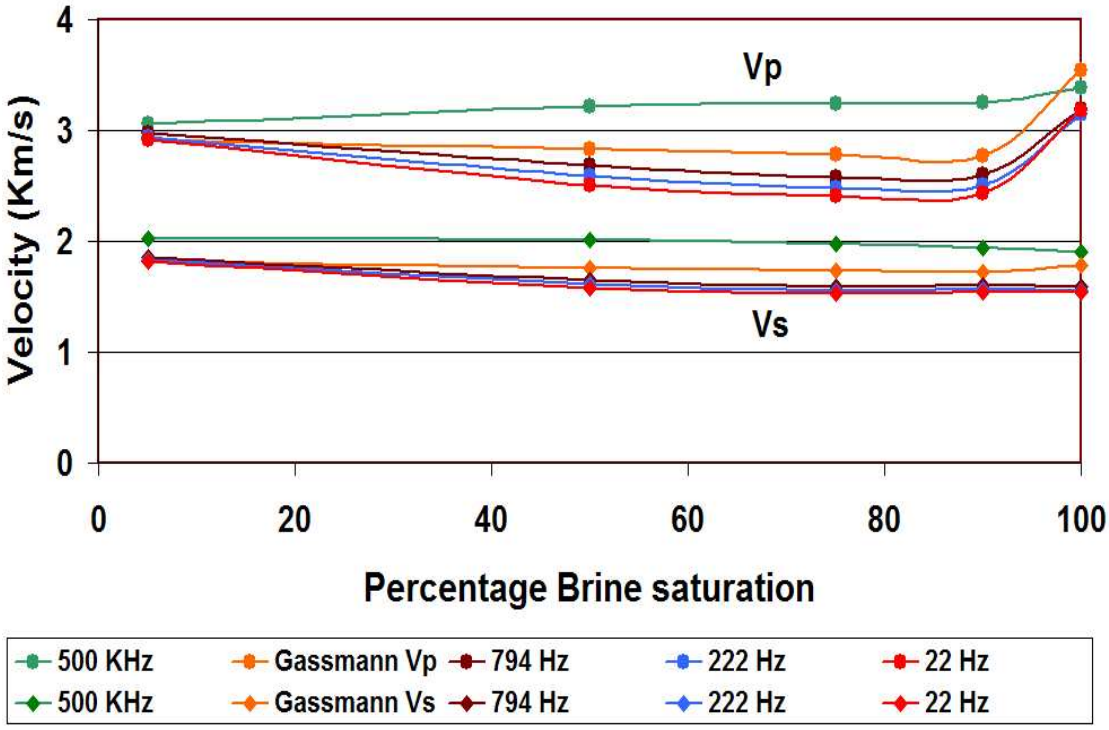

FIG. 5.13. ITF-51: Low-frequency and ultrasonic velocity versus brine saturation. Gassmann calculated velocities are plotted for comparison and it assumes relaxed fluid pressure.

layers wets the grain contacts and softens the rock causing an increase in attenuation [Clark et al., 1980]. At residual gas saturation ($\sim$ 90% brine saturation), 1/Qp shows a jump in attenuation and is very significant. Compressional attenuation is due to bulk liquid flow and at near full saturation it requires zones of high compressibility for the liquid to move and equilibrate. At residual gas saturation (90% brine) the amount of liquid is maximum and also there is small amount of gas present promoting liquid flow resulting in very high values of compressional attenuation. At full saturation the values drop and become almost equal to the dry attenuation values. The

attenuation at full saturated condition can be explained using *Mavko and Nur* [1975] squirt flow theory and by *O'Connell and Budiansky* [1977] intercrack flow mechanism. Their mechanism predict both a drop in compressional attnuation as can be seen in our data and also a significant shear attenuation at full saturation as can be seen in figure 5.14(b). Shear attenuation increases from dry to partial saturation and around 40% brine saturation it reaches a maximum. At 40% saturation the meniscus between the grain contacts are filled with brine and they significantly reduce the shear strength of the rock causing an increase in shear attenuation. 1/Qs then becomes almost constant to full saturation.

Thus with the help of different theories (discussed in Chapter 2) we can explain the effect of saturation on velocity and attenuation. These theories predict that for a particular attenuation or dispersion mechanism there is a corresponding attenuation/relaxation peak frequency. Thus, in theory, attenuation is a relaxation type mechanism [Cole-Cole, 1941] with a characteristic frequency (peak attenuation) corresponding to a particular relaxation mechanism.

Figure 5.15 shows the relaxation/attenuation peak for Merced formation sandstone. The attenuation values increase and peak at around 110 Hz and then decrease. Also, for dry measurements there is low attenuation with little change with frequency. This corresponds to no significant velocity dispersion. Due to system resonance around 120 and 1000 Hz the attenuation values become unreasonable.

It is clear that there are differences between ultrasonic velocity and low-frequency velocity when it comes to partial saturation. Also the open/close boundary conditions effects the measurements of velocity and attenuation only for low-frequency measurements. It is important to mention here that the dry condition refers to vacuum dry and the saturation may not be uniform and I will discuss the effect of fluid

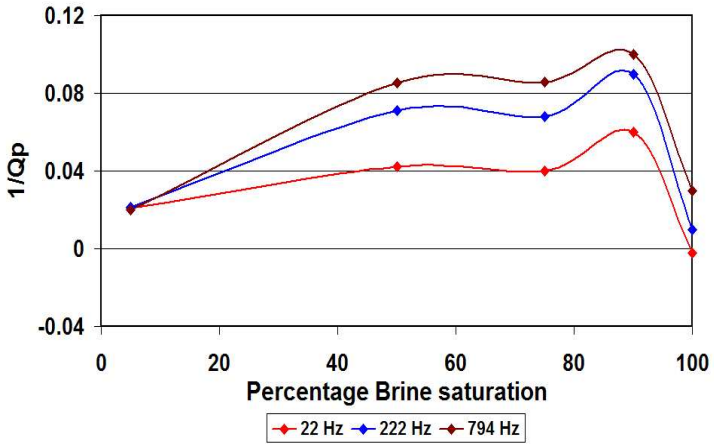

(a) ITF-51: Compressional attenuation with changing brine saturation. Differential pressure=6.89 MPa.

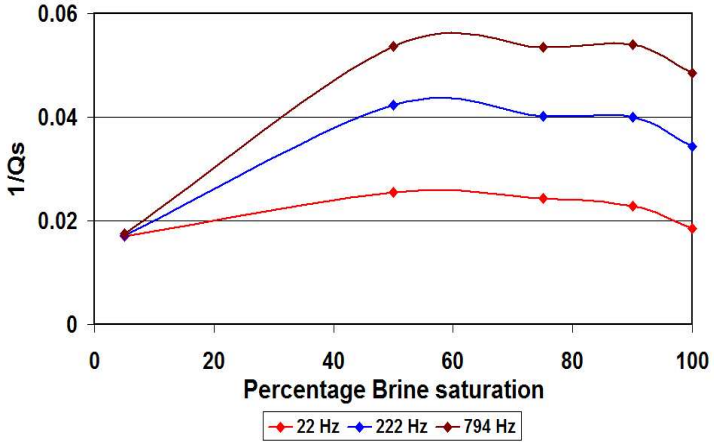

(b) ITF-51: Shear attenuation with changing brine saturation. Differential pressure=6.89 MPa.

FIG. 5.14. Attenuation versus percentage brine saturation.

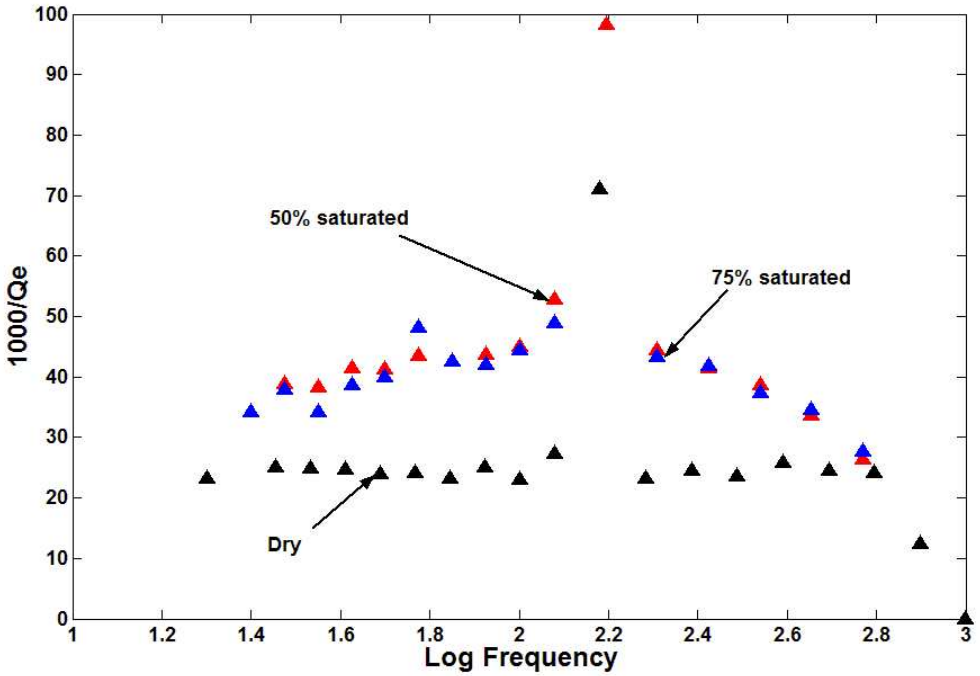

FIG. 5.15. Merced sandstone: Young's attenuation curve at different brine saturations. Notice the effect of system resonance at 120Hz and 1000 Hz.

distribution on these measurements in section 5.4.

5.3 Effect of fluid mobility

Fluid viscosity and permeability are two important parameters that describe the fluid mobility inside a rock. Increase in viscosity (η) decreases the mobility and an increase in permeability (κ) increases the mobility of the fluid. Viscosity of fluid can be changed with changing temperature as in thermal enhanced oil recovery processes (EOR). The effect of fluid viscosity has been discussed in detail by Wyllie et al. [1962] and Nur and Simmons [1969a]. Their results suggest that high viscosity fluids do not

contribute much to attenuation because they reduce the effective permeability of the rock. But Nur and Simmons [1969a] have shown that the viscosity effect is frequency dependent and is related to some relaxation type mechanism.

The peak attenuation frequency (relaxation frequency, ω_c) depends on the fluid mobility. According to Biot theory [Biot, 1956a,b] the peak should move toward higher frequencies with decrease in mobility ($\omega_c \propto \frac{\eta}{\kappa}$). This is in contrast to the other mechanisms (like squirt where $\omega_c \propto \frac{\kappa}{\eta}$) that predict that the peak should move toward lower frequencies as the mobility is decreased [O'Connell and Budiansky, 1977]. This decrease is because the fluid will require more time to come to a relaxed state, which corresponds to a lower frequency of the propagating wave. To test these two theories, I made measurements on Uvalde carbonate. This rock is filled with very heavy oil. Measurements were made at temperatures of 25^0 C, 40^0 C and 60^0 C. The results are shown in figures 5.16(a)and 5.16(b). It is clear that as the temperature is increased the attenuation increases and that also lower frequencies have higher attenuation. Thus peak attenuation shifts toward lower frequencies as the viscosity is increased (temperature is lowered). I need to measure the properties of the heavy oil in order to confirm our result. Preliminary studies have shown that it is a very viscous oil and does not flow at room temperature. Thus Biot's mechanism is not applicable.

Permeability of the rock is another factor that influences fluid mobility. An increase in permeability would cause an increase in mobility. To test this hypothesis I measured the ITF samples which have similar porosity (except ITF-79 sample) but different permeability. This would eliminate the effect of porosity. Figures 5.17(a) and 5.17(b) show the results for these measurements. It is clear from the figures that low-permeability rocks experience higher attenuation compared to high permeability samples. If we measure the entire frequency spectrum we would observe that with

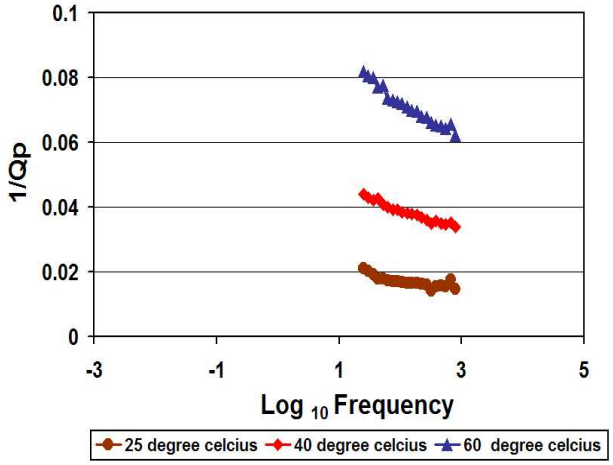

(a) Shift in 1/Qp peak with temperature. Differential pressure=10.35 MPa.

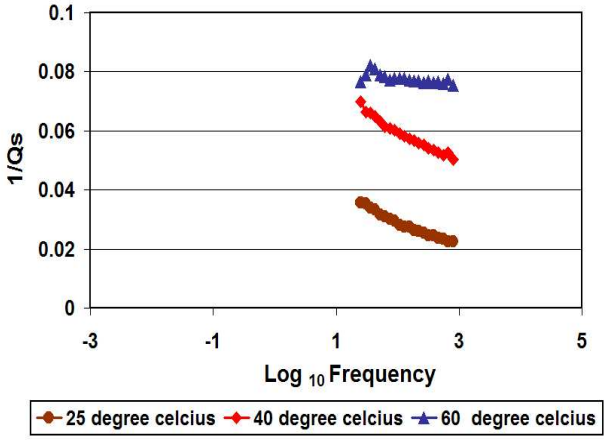

(b) Shift in 1/Qs peak with temperature.Differential pressure=3.45 MPa.

FIG. 5.16. Uvalde carbonate: Shift in peak frequency with change in viscosity.

an increase in permeability the relaxation peak shifts toward higher frequency. One can then argue that the change in permeability only causes an amplification in peak attenuation (relaxation peak) and there is no shift in peak attenuation frequency. To counter this argument I make use of the relationship between the maximum attenuation and *modulus defect*. The relationship is given as:

$$\left(\frac{1}{Q}\right)_{max} = \frac{1}{2}\frac{\Delta M}{\overline{M}} \tag{5.5}$$

$$\Delta M = M_\infty - M_0 \tag{5.6}$$

$$\overline{M} = \sqrt{M_\infty M_0} \tag{5.7}$$

where $\frac{\Delta M}{\overline{M}}$ is the modulus defect, M_∞ is the high-frequency limiting modulus and M_0 is the low-frequency limiting modulus. Using the low-frequency and ultrasonic velocities of the ITF-samples I computed the maximum attenuation and they ranged from a value of .09 to .12 which are very close to each other within the limits of experimental error. Thus, it is sure that there is no amplification in the attenuation peak and the change in permeability causes a shift in peak attenuation frequency.

In 5.17(b) the 178 mD rock has lowest 1/Qs. This is contrary to our expectation and one of the possible explanation for this behavior could be because of difference in the porosity ($\sim$ 17%) of this rock compared to the other ITF samples ($\sim$ 21%).

Figure 5.18 compares the open versus close valve velocity for different permeability rocks (ITF samples). Sample-51 does not show any difference between and close velocity because of the very low-permeability. As we increase the permeability we can see the difference between open and close valve compressional velocity, and the range of frequency in which this difference is observed increases with increase in rock permeability. If we run our measurements at lowest frequencies ($\leq$ 3 Hz) then we expect to see some difference in compressional velocity for ITF-51 sample because

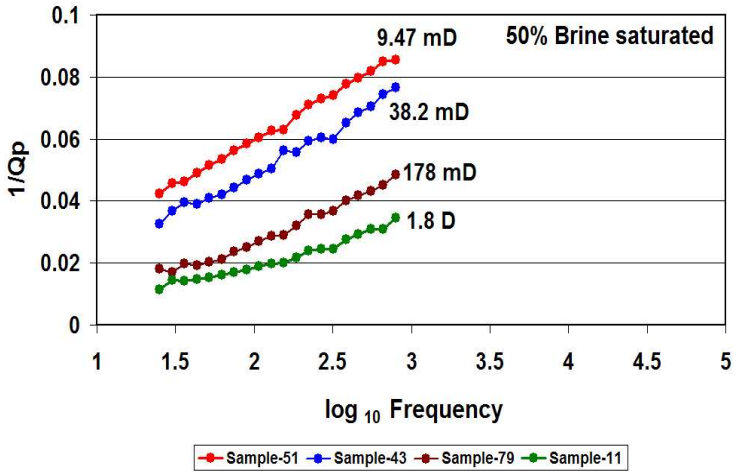

(a) Dependence of compressional attenuation on permeability. Differential pressure=6.89 MPa.

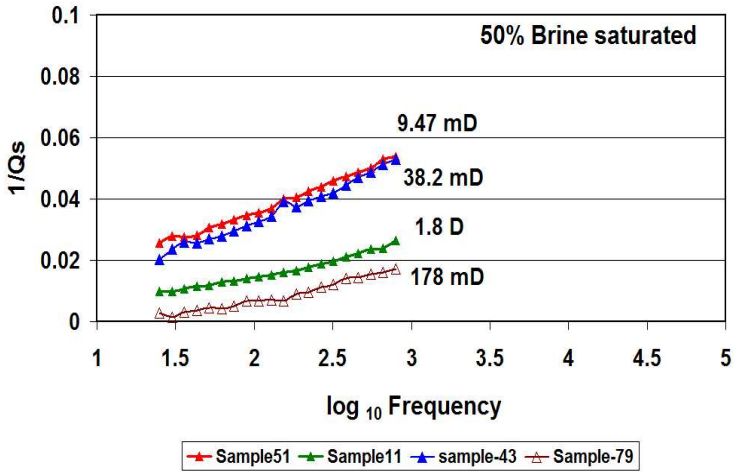

(b) Dependence of shear attenuation on permeability. Differential pressure=6.89 MPa.

FIG. 5.17. ITF samples: Dependence of attenuation on rock permeability.

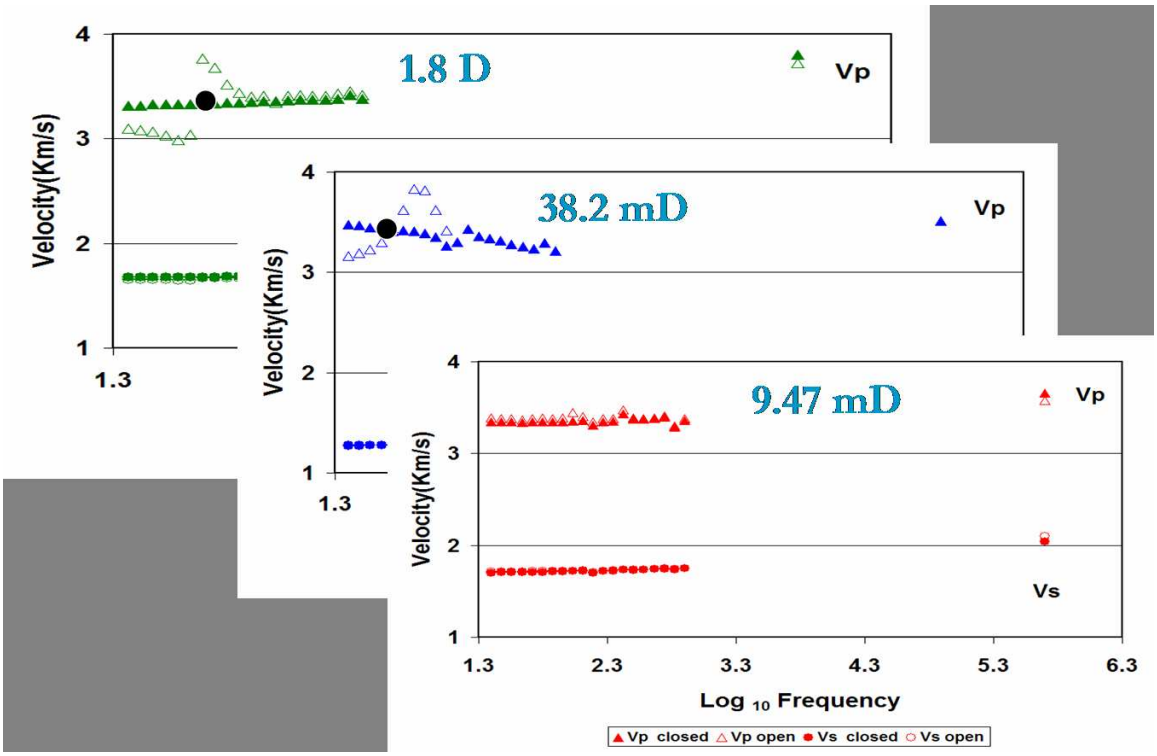

FIG. 5.18. ITF samples: Difference between open and closed boundary Vp for different permeability rocks. The frequency band in which this difference is seen increases with permeability.

these frequencies would be able to provide enough time for fluids to move through the low permeability rock. This is equivalent shift in relaxation frequencies to higher values as the permeability is increased. Again the Biot predictions are opposite to what has been observed through my measurements.

5.4 Effect of fluid distribution

In all the results shown in the previous section, the method of fluid saturation was the same: fluid was injected from the top of the sample through the pore fluid

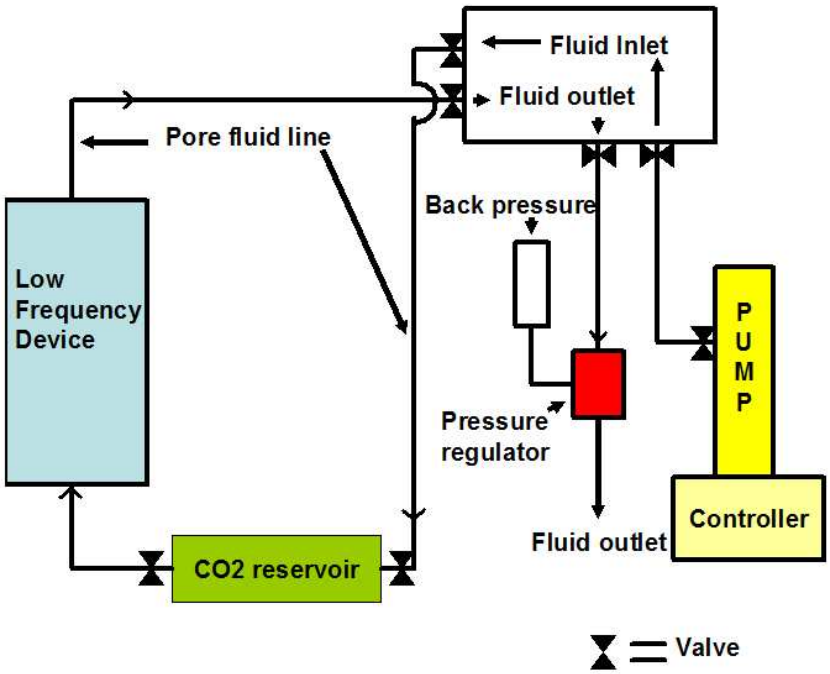

FIG. 5.19. Schematic showing injection of CO_2+water mixture in the rock sample. Also shown is the process which is used to extract water from the sample as CO_2 comes out of solution.

line, and the fluid volume was increased to increase the saturation, given that the pore volume is known. It is very difficult to ascertain anything about the homogeneity of the distribution because of capillary action and gravity effects. However the fluid distribution is an important aspect of many dispersion/attenuation theories. In White's gas pocket model the size of the gas pockets are bigger than the pore size. Squirt mechanism assumes that the individual pores are partially saturated. In order to understand the difference between these two different fluid distributions another method of saturation was used. The configuration is shown in figure 5.19.

A CO_2+water mixture (single phase) is injected in the rock sample from the CO_2 reservoir. The pressure in the reservoir is controlled by the pump. Three pore volumes of CO_2+water mixture was injected in the sample. Then the reservoir was closed and with the help of a pressure regulator and back pressure the pore pressure was dropped slowly starting with the initial value of 6.89 MPa. As the pressure was decreased, CO_2 started coming out of solution displacing water from the pore spaces, which was collected in a graduated cylinder. The CO_2 saturation was computed based on the volume of water expelled from the rock. The partial saturation done this way is on the pore scale level whereas in the previous method it was more like patchy saturation.

The result is shown in figure 5.20(a) and 5.20(b) for ITF-43 sample. The differential pressure was kept constant at 6.89 MPa. Ultrasonic velocity differs significantly from low-frequency velocities at partial saturation. 1/Qp increases with saturation and around 10% CO_2 saturation shows a maximum value. If we compare these results with similar measurements done on ITF-43 sample with patchy saturation method (figures 5.21(a) and 5.21(b)) we can see similar results. This is also the case for the data obtained on ITF-51 sample (figure 5.13 and 5.14(a)). Both methods of saturation produce similar results which means that for these rock samples the global and local permeabilities are the same. Global permeability is responsible for fluid pressure relaxation in patchy saturation whereas local permeability is dominant mechanism for fluid pressure relaxation in case of pore scale partial saturation.

One of the problems with open boundary condition is the complex fluid motion and resonance in the pore fluid system. To avoid this complexity, another method was used to create an 'open' boundary condition. A layer of gas on top of a liquid saturated rock can act as an open boundary condition, as the gas with very high

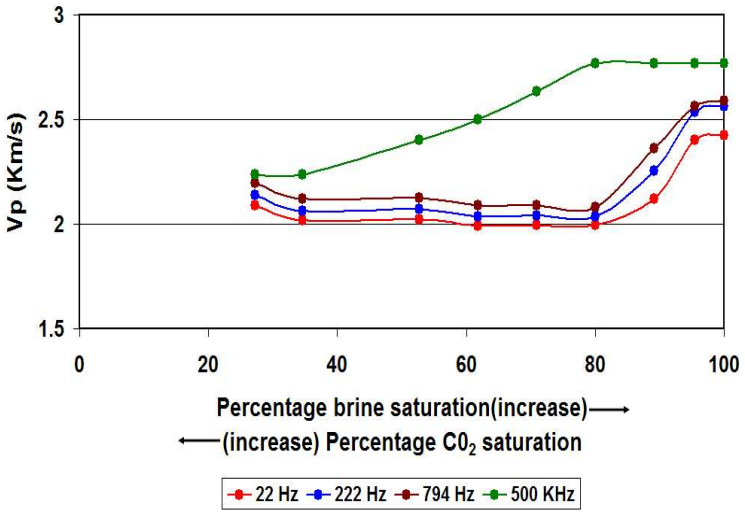

(a) Velocity as a function of partial CO_2 saturation.

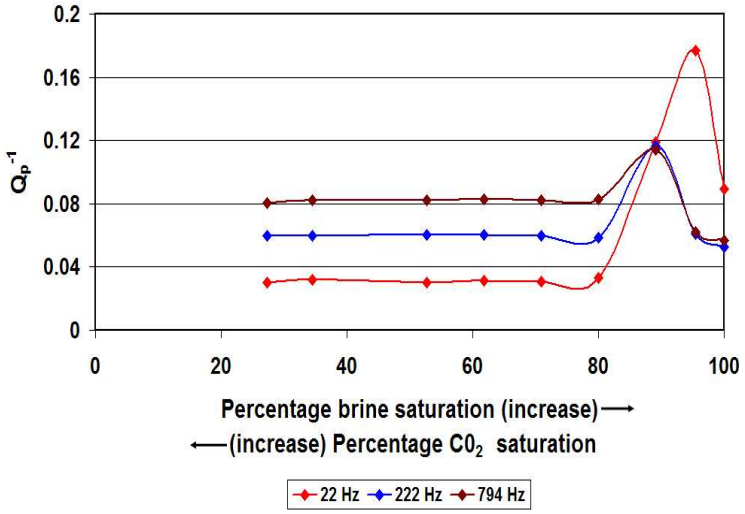

(b) Compressional attenuation as a function of partial CO_2 saturation.

FIG. 5.20. ITF-43 sample: Change in velocity and 1/Qp with partial CO_2 saturation.

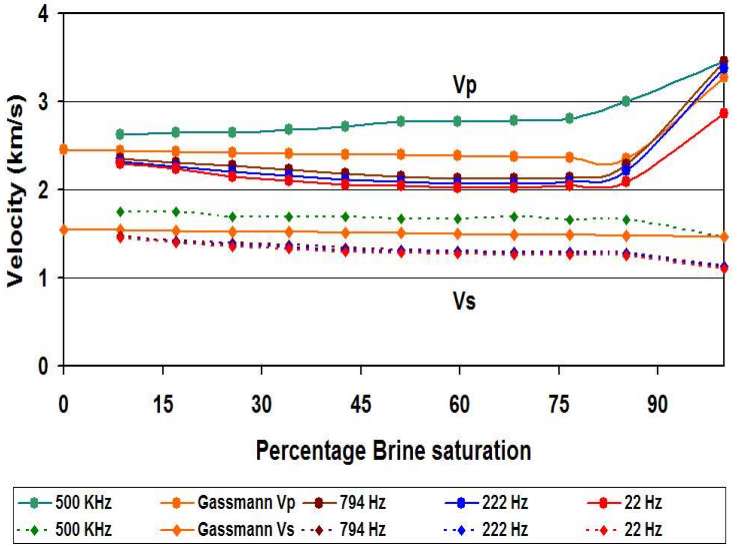

(a) Velocity as a function of partial brine saturation. Differential pressure 6.89 MPa.

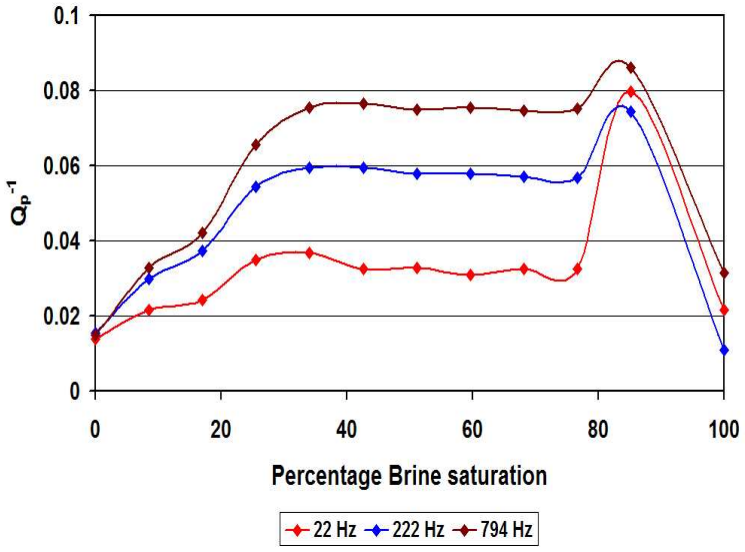

(b) Compressional attenuation as a function of partial brine saturation. Differential pressure=6.89 MPa.

FIG. 5.21. ITF-43 sample: Velocity and 1/Qp as a function of partial brine saturation.

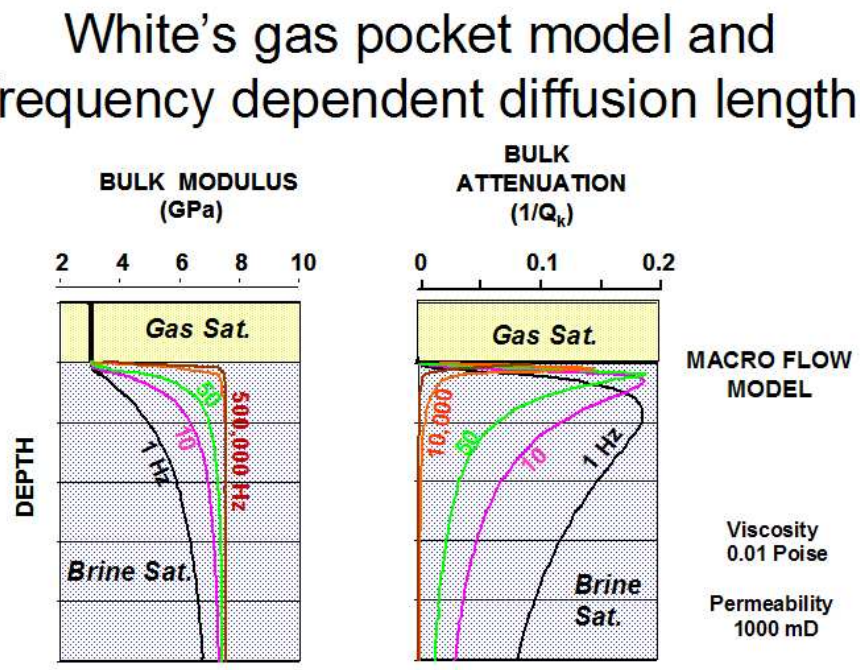

FIG. 5.22. Frequency dependent diffusion length. This is derived from White's gas pocket model assuming that the radii of the gas pockets tend toward infinity (Courtesy: Batzle, 2003).

compressibility can act as a vent for pressure release in the remainder of the sample. This type of fluid distribution can also be used to test White's [1975] *gas pocket model* which has been discussed in Chapter 2. In his model if we increase the radius of the gas pocket to infinity then it becomes a layer of gas in contact with liquid. This situation also commonly exists in the real earth where a thin layer of gas is trapped on top of a liquid saturated zone. This is illustrated in figure 5.22.

The boundary between the gas and the liquid influences the measured properties differently for different frequencies when a wave propagates through the composite medium. This is because the diffusion length is dependent on the frequency (inversely

proportional). For a given frequency, any portion of the rock within a diffusion length from the boundary, is relaxed, which means it can communicate with the gas layer. For a very high permeability rock, the diffusion length is roughly a quarter wavelength [Hoffmann, 2003]. This type of fluid distribution can explain high attenuation in rocks which have a very thin layer of gas on top of brine. The source of attenuation is not only the gas layer but also the brine zone which is inside the diffusion length, allowing brine movement and pressure equilibration with the gas zone. This also means that depending on the frequency of the propagating wave the thickness of the gas zone changes. The portion of the brine saturated rock which is inside this diffusion length will have the same lower bulk modulus as that of the gas due to pressure equilibration. Figures 5.23(a) and 5.23(b) compare the velocities for brine saturated Rim Sandstone with a thin layer of butane on top. We can see that the compressional velocity is reduced as butane is introduced, compared with fully brine saturated case. This happens for almost the entire frequency range. Pressure generated in brine due to wave propagation is released in the butane layer as butane is a very compressive fluid. If we invert for the measured compressional velocity the entire rock would appear to be butane saturated. Figures 5.24(a) and 5.24(b) compare the attenuations under different fluid distributions. The butane saturated rock has very low attenuation. 1 cc butane on top of 9cc brine has the highest 1/Qp. It has already been demonstrated that at around 90% brine saturation (90% brine +10% (air+water vapour)), 1/Qp has the highest value. Injecting 1cc of butane corresponds to 90% brine saturation in this sample. That is why we get highest attenuation values for this fluid distribution. When 2cc (20% butane+80% brine) butane is injected the attenuation drops and becomes very close to 85% brine+15% (water vapour+air) saturated value. Butane does not contribute much to shear attenuation and the reason will be discussed in the

next section. This is why the 1/Qs values for butane saturated case is lowest. In the other saturations 1/Qs depends on the percentage of brine in the pore space. We also know from previous results that 1/Qs increases from dry to partial saturation and becomes almost constant to full saturation. This is the reason why 1cc butane (10% butane+90% brine), 2cc butane (20% butane+80% brine) and 85% brine+15%(water vapour+air) saturated cases have almost the same 1/Qs values for all frequencies.

It should be mentioned that it is very difficult to create a simple, uniform layer of butane on top of brine. The injection process has to be performed slowly and carefully and still we believe that due to viscous fingering and gravity, butane is not distributed as a layer, rather it spreads inhomogeneously. It can be concluded that the two different methods of fluid saturation did show similar results for our experiments. Also, measurements indicate that for the butane on top of brine case half of the rock (the gages are put in the middle of the sample) appears to be inside the diffusion length at all frequencies.

5.5 Effect of fluid substitution

The effect of fluid substitution on velocity and attenuation is an interesting area of application. In dynamic reservoir characterization attenuation and velocity are important seismic attributes which can be used to map fluid flow and changes in the reservoir conditions. Before we extract these properties from seismic data and use it for reservoir assessment, it is important to understand the processes by doing laboratory experiments. In the previous sections it was shown that dry rock attenuation is very small compared to partially saturated rock and the highest compressional attenuation is observed at partial gas saturation (around 90% liquid saturation). Fully saturated rock has very small compressional attenuation for both gas and liquid sat-

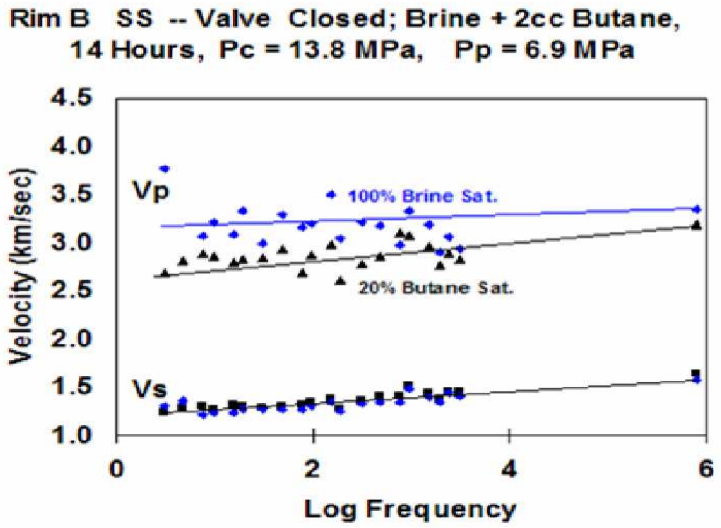

(a) 2 cc butane on top of brine saturated rock. Valve is kept closed.

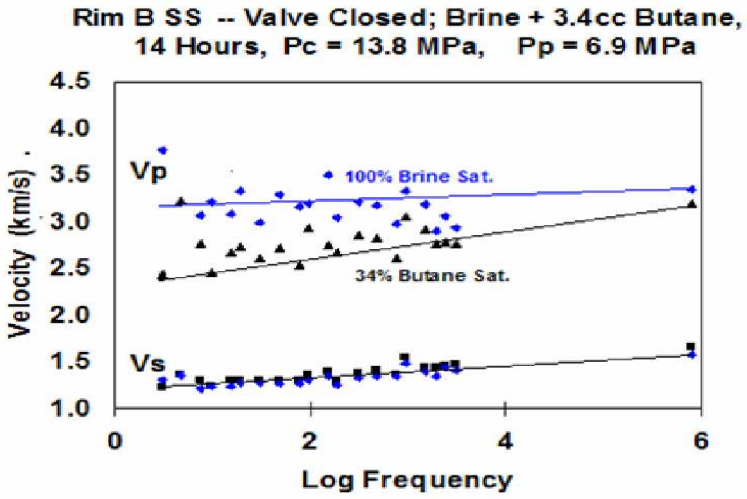

(b) 3.4 cc butane on top of brine saturated rock.Valve is closed.

FIG. 5.23. Rim sandstone: Velocity comparison between brine saturated rock and a layer of butane on top of brine.

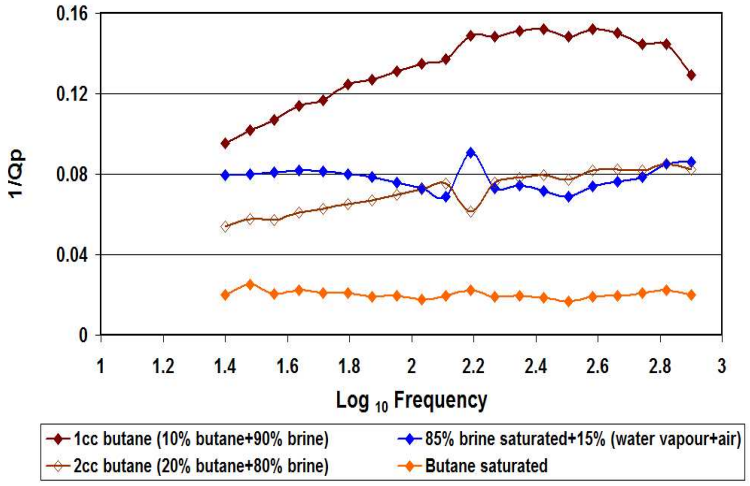

(a) 1/Qp for different saturations and fluid distributions.

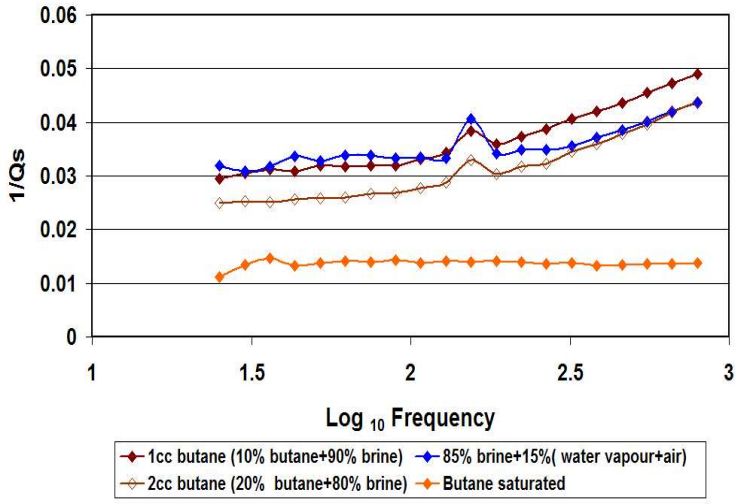

(b) 1/Qs for different saturations and fluid distributions.

FIG. 5.24. ITF-43: Attenuation comparison for different fluid distributions and saturations.

urated rock. Also, as the liquid saturation is increased the low-frequency seismic velocity decreases and ultrasonic velocity increases. Only, at full liquid saturation the seismic velocity increases.

A series of fluid substitution experiments were done on the ITF-43 sample to understand the effect of these substitutions on velocity and attenuation. The sequence of substitutions are as follows:

- Dry measurements.
- Sample saturated with butane (since it is easy to get the butane out of the sample just by releasing the pore pressure as it vaporises at atmospheric pressure).
- Then the rock was slowly saturated with brine with measurements done at small saturation steps.
- After that the sample was saturated with water+CO_2 (single phase) mixture and using the technique discussed earlier the sample finally attained 70% CO_2 saturation with 30% residual brine. Two measurements were done, one at 2 MPa and other at 6.89 MPa so that in the first case we have CO_2 in the gaseous phase and in the other case it is a liquid. Then all the CO_2 was removed (by releasing the pressure and running a vacuum).
- Then pentane was injected which resulted in 70% saturation with 30% residual brine.
- Finally brine was flushed through the rock to simulate a water flood and 5 cc pentane was recovered which corresponds to 80% brine+ 20% residual pentane saturation.

Fluid	Eff. fluid density (gm/cc)	Eff. fluid modulus (GPa)	Rock bulk modulus (GPa)
Dry	0.0	0.0	5.6
100% Butane saturated	0.584	0.59	8.08
100% Brine saturated	1.0	2.5	17.0
70% Gas CO_2 + 30% Brine	0.335	0.0454	5.8
70% Liquid CO_2 + 30% Brine	0.622	0.0638	5.89
70% Pentane+ 30% Brine	0.741	0.938	9.6
80% Brine+ 20% Pentane	0.926	1.69	12.4

Table 5.1. ITF-43 sample: Change in rock bulk modulus with different fluid substitution/saturation. These measurements are done by computing effective fluid modulus and density and using Gassmann substitution.

The effect on bulk modulus was computed using Gassmann substitution and this was compared with the measured change in the bulk modulus. The fluid properties were computed using STRAPP (NIST standard reference database for NIST thermophysical properties for hydrocarbon mixture) software and FLAG (fluid property calculation software developed by Center for Rock Abuse, CSM and University of Houston) program. For a mixture of fluids the bulk modulus was volume averaged (equation 5.4). The effective fluid density, effective modulus, rock bulk modulus is shown in table 5.1.

The measured change in bulk modulus is shown in figure 5.25(a). Initial butane saturation increases the modulus of the saturated rock from 5.6 GPa (dry) to 8.08 GPa. Butane has a small bulk modulus of 0.59 GPa at room temperature and 3.45 MPa pressure. The Gassmann calculation predicted the same value as the actual measured rock value. 100% brine saturated rock has the highest bulk modulus (17.0 GPa). This is because brine (50,000 ppm) has a bulk modulus of 2.5 GPa at room temperature and 6.89 MPa pressure. The measured bulk modulus for 100% brine sat-

urated rock has slightly higher values (around 21.0 GPa). The velocity is also highest (figure 5.25(b)) for brine saturated case but the velocity shows negative dispersion which is difficult to explain. 70% gas CO_2+30% brine saturated case lowers the bulk modulus of the rock to 5.8 GPa. This is due to a very low bulk modulus of gas CO_2 (0.032 GPa at room temperature and 2 MPa pressure). The rock bulk modulus does not change much when we go from 70% gas CO_2+30% brine to 70% liquid CO_2+30% brine (5.8-5.89 GPa). This is because the bulk modulus of 70% liquid CO_2+30% brine is also very small (0.045 GPa) and comparable to 70% gas CO_2+30% brine (0.032 GPa). The actual measured rock bulk modulus for 70% gas CO_2+30% brine and 70% liquid CO_2+30% brine case is smaller than the Gassmann computed bulk moduli. Infact the measurd values are less than the dry rock bulk moduli. This is an error as a fluid saturated rock should have higher bulk modulus compared to dry case [Gassmann, 1951]. This error could be because of the softening of the rock due to fluid injection. Due to the density effect and a probable drop in shear modulus due to grain softening, the measured velocity of the 70% gas CO_2+30% brine and 70% liquid CO_2+30% brine saturated rock is less than the measured dry velocity (see figure 5.25(b)). The measured velocity of 70% liquid CO_2+30% brine saturated case is less than 70% gas CO_2+30% brine saturated case because of the much higher density of liquid CO_2 compared to gaseous CO_2, but almost equal bulk modulus. 70% pentane+30% brine saturated case increases the rock bulk modulus to 9.6 GPa. Pentane has a fairly high bulk modulus of 0.74 GPa at room temperature and 6.89 MPa pressure. The measured rock bulk modulus for this case is almost the same as the Gassmann predicted value. When the volume fraction of brine is increased from 30% to 80% (water flood resulting in 80% brine+20% pentane) the rock bulk modulus increases from 9.6 GPa (70% pentane +30% brine) to 12.4 GPa. This is due to

higher contribution of brine bulk modulus in the effective fluid modulus calculation. Again the measured rock bulk modulus matches the calculated value. For all these substitutions the differential pressure (Pd) was kept constant at 6.89 MPa.

Figure 5.26(a) and 5.26(b) show the effect on compressional and shear attenuation because of the fluid substitution for ITF-43 sample. It can be seen that butane saturated and brine saturated 1/Qp's are very small and are very close to dry 1/Qp values. The compressional attenuation for 70% CO_2+ 30% brine saturated rock is the highest. This is like a partial saturated case where attenuation increases with increasing brine saturation and reaches maximum at around 90% brine saturation. We should note that the negative 1/Qp values for 20% pentane+ 80% brine saturated case must be erroneous and at this point there is no explanation for this behavior. A closer look at 1/Qs values suggests that dry rock and butane saturated rock have very small shear attenuation. This can be explained using the stress relaxation mechanism proposed by Spencer [1981]. Through his measurements he established that the relaxations occur mainly in the shear modulus which are thermally activated and have low activation energies. When a low-amplitude stress is applied to the rock strain is generated which causes active deformation sites. The relaxation process involves movement of adsorbed molecules to these sites. These molecules bond to the surface and reduce the surface free energy. The higher the reduction in surface free energy the higher is the modulus defect which corresponds to higher peak attenuation values. The modulus defect (maximum attenaution) is large with water which is polar and are probably hydrogen bonded to hydroxyls on silica and quartz. Nonpolar liquids like butane, n-decane and n-pentane weakly interact with the hydroxyls and thus the modulus defect is small. This is probably the reason why butane saturated and dry rock show very small shear attenuation. The rest of the fluid substitutions show

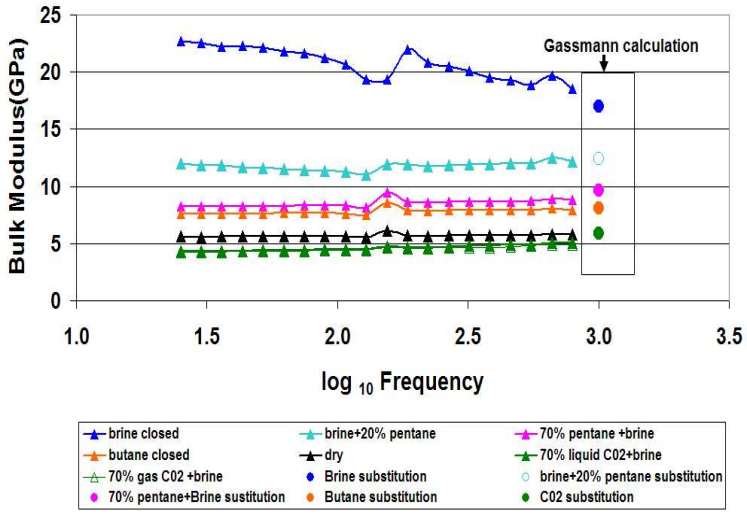

(a) Bulk modulus change with different fluid substitution. The isolated points are Gassmann calculations.

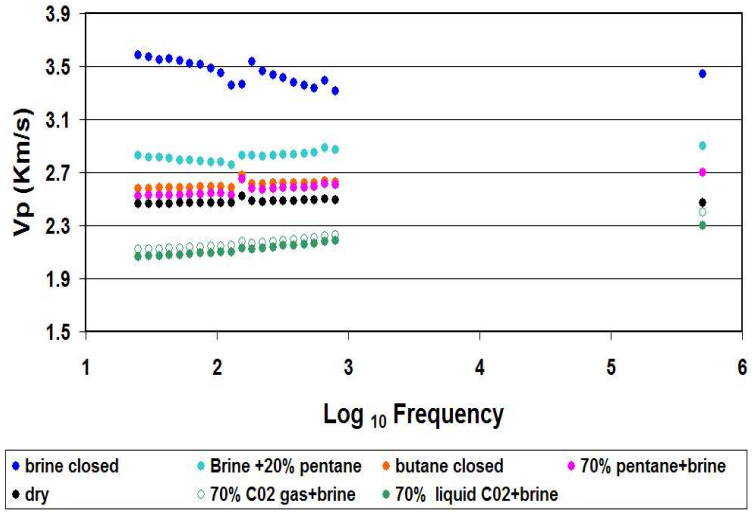

(b) Change in velocity due to different fluid substitution. Isolated points are measured ultrasonic velocities.

FIG. 5.25. ITF-43 sample: Bulk modulus and velocity comparison for different fluid substitutions/saturations.

almost the same shear attenuation. During all the fluid substitutions water was the wetting phase and the stress relaxation occurs in the wetting phase. Due to this reason the change in fluid does not effect the shear attenuation values. This is also true with the rock shear velocity where the shear modulus does not change with fluid but the velocity changes due to density effect.

5.6 Effect of clay

Clays play a very important role in the attenuation and dispersion measurements. Most of the discussion on attenuation and dispersion in the literature ignore the fact that majority of the rocks in the subsurface are shales and sandstones, and can have clays in their pore spaces. Clays react with water and many types will swell depending on the water chemistry. This swelling can reduce the permeability of the rock, change the elastic properties and influence the attenuation and dispersion measurements. To understand the effect of clays on these measurements, I used the Foxhill's formation sandstone sample which has pore lining and pore filling clays (see Chapter 4). Figure 5.27(a) shows the velocity at 3.45 MPa differential pressure for Foxhill's sample. Compressional velocity shows a hump like feature. Initially this was difficult to explain. When the open valve 1/Qe was compared with close valve 1/Qe the result was also surprising (figure 5.27(b)). Open valve 1/Qe is smaller than close valve which is contrary to what we have seen earlier. Open valve allows more fluid flow and this should correspond to higher attenuation at low frequencies. As mentioned in the previous sections, with increasing saturations we expect 1/Qe to increase, then at 100% saturation 1/Qe should drop to a lower value.

Figure 5.28 shows the change in 1/Qe with water saturation for Foxhill's sandstone. At 100% distilled water saturation, 1/Qe value is the highest. All these results

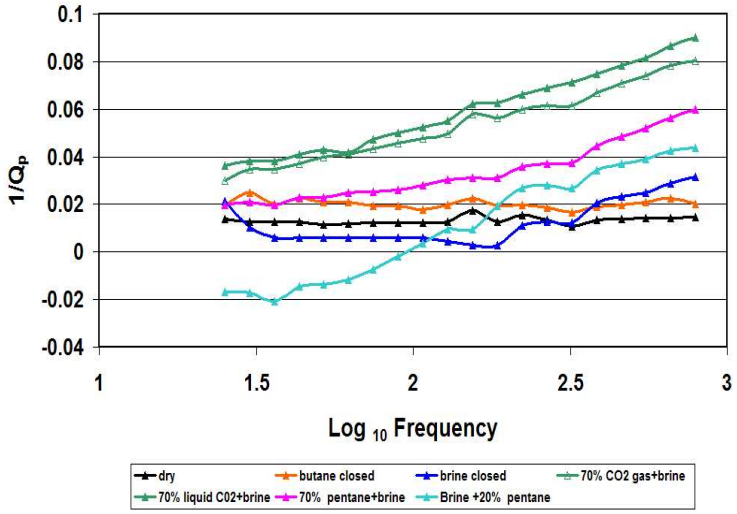

(a) 1/Qp change with different fluid substitution.

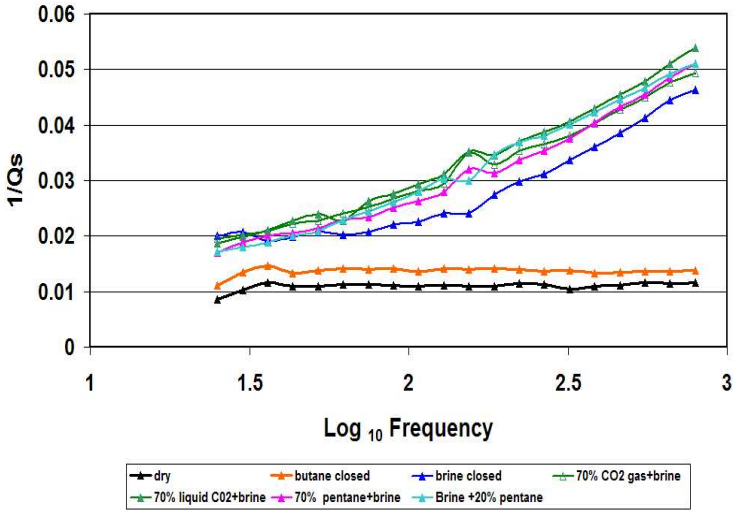

(b) 1/Qs change with different fluid substitution.

FIG. 5.26. ITF-43: Change in attenuation with different fluid substitution.

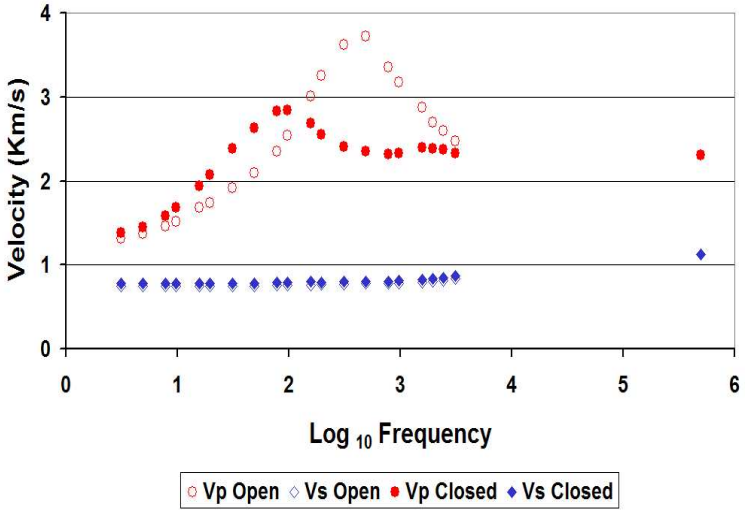

(a) Velocity as a function of frequency. Pc=3.45 MPa, Pp=0 MPa.

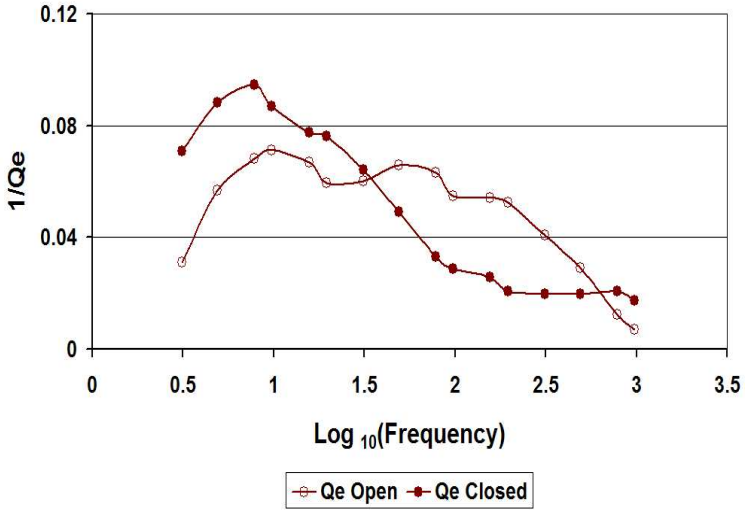

(b) 1/Qe for open and close boundary condition. Pc=3.45 MPa, Pp=0 MPa.

FIG. 5.27. Foxhill's sandstone: Velocity and attenuation at 3.45 MPa confining pressure and zero pore pressure.

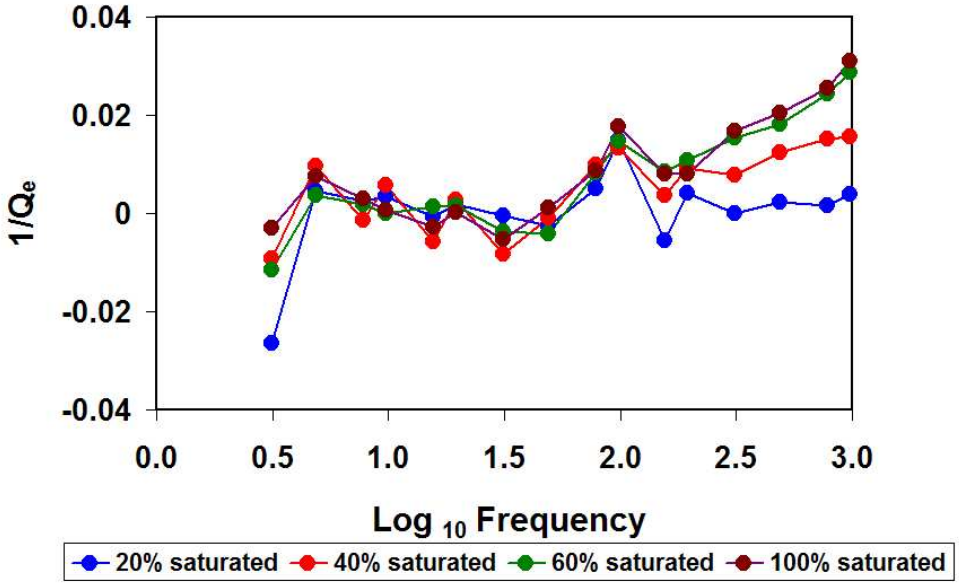

FIG. 5.28. Foxhill's sandstone: Change of 1/Qe with percentage water saturation. 100% saturated 1/Qe should be lower than 60% saturated. Due to zero pore pressure the sample is still not completely 100% water saturated.

were unexpected. However, the Poisson's ratio measured at 3.45 MPa confining pressure and zero pore pressure (figure 5.29) helped explain these unexpected results. The value of Poisson's ratio was 0.45 which is very close to the rock being a fluid (fluid Poisson's ratio=0.5). Clays swell when they react with distilled water and produce a swelling pressure which counteracts the applied confining pressure. Due to this the rock starts behaving almost like a fluid where the grains float in a more fluid clay matrix. This is probably why the Poisson's ratio increased and became very close to that of a liquid. Also, 100% water saturation can never be achieved at zero pore pressure because of the presence of small amount of gas and water vapor in the pores. Then the confining pressure was increased to overcome the clay swelling, and the pore

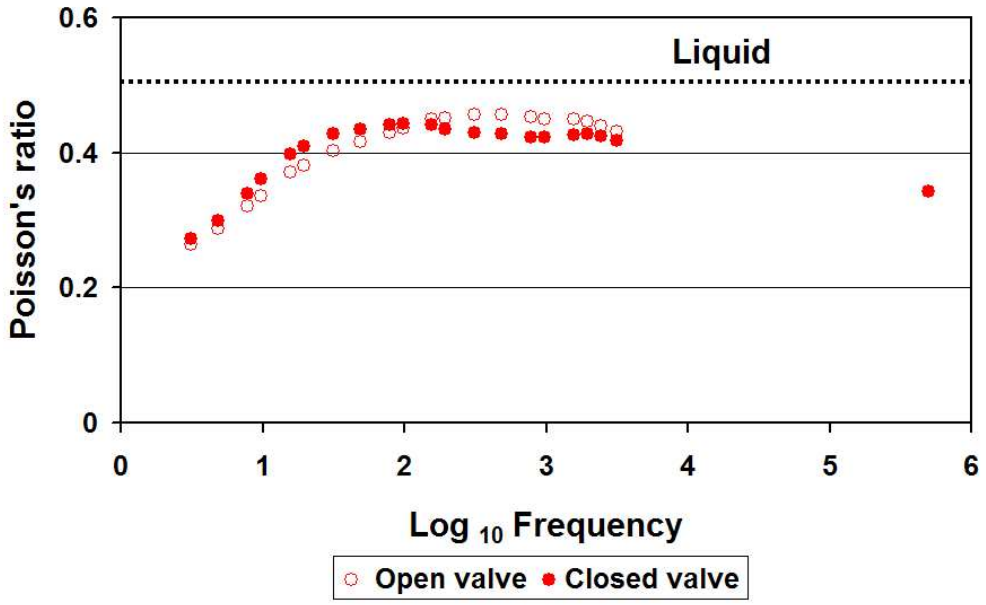

FIG. 5.29. Foxhill's sandstone: Poisson's ratio as a function of frequency at 3.45 MPa differential pressure. A value of 0.45 is very close to being a liquid.

pressure was increased to achieve 100% saturation. The velocity and 1/Qe values are shown in figures 5.30(a) and 5.30(b). The resonance effect is removed from the compressional velocity curve and open boundary 1/Qe is larger than closed velocity. Also, the Poisson's ratio reduced to a value of 0.35 with increasing confining pressure (figure 5.31(a)). Figure 5.31(b) shows the decrease in 1/Qe values with increasing pore pressure. This shows that with increasing pore pressure the remaining gas and the water vapor goes into solution and the rock becomes 100% water saturated. Thus, it can be seen that clays play a very important role and extra care should be taken when the rock to be measured has clay in it's pore spaces. As a precaution brine should be always used instead of distilled water. If possible a clay analysis should be performed in order to better understand its effect on these measurements.

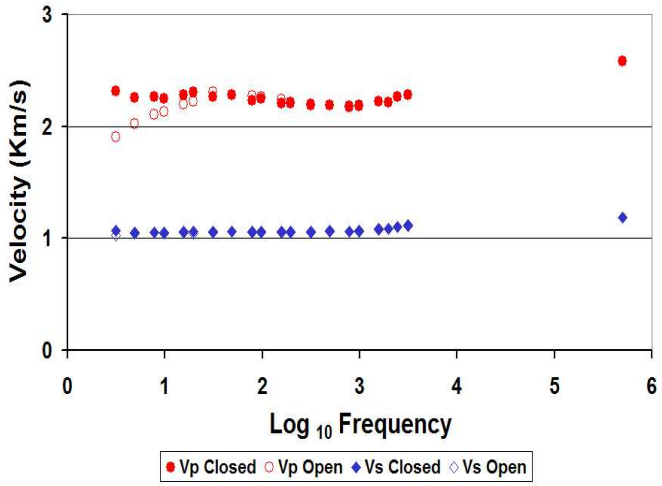

(a) Velocity as a function of frequency. Pc=13.78 MPa, Pp=6.89 MPa.

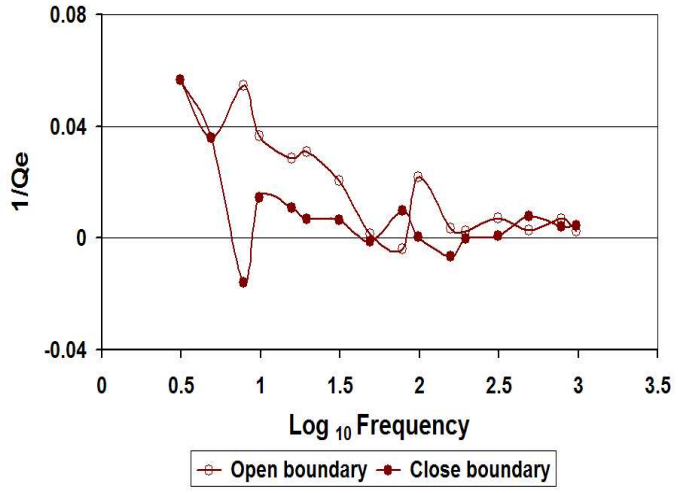

(b) 1/Qe for open and close boundary condition. Pd=13.78 MPa, Pp=6.89 MPa.

FIG. 5.30. Foxhill's sandstone: Velocity and attenuation at 13.78 MPa confining pressure and 6.89 MPa pore pressure.

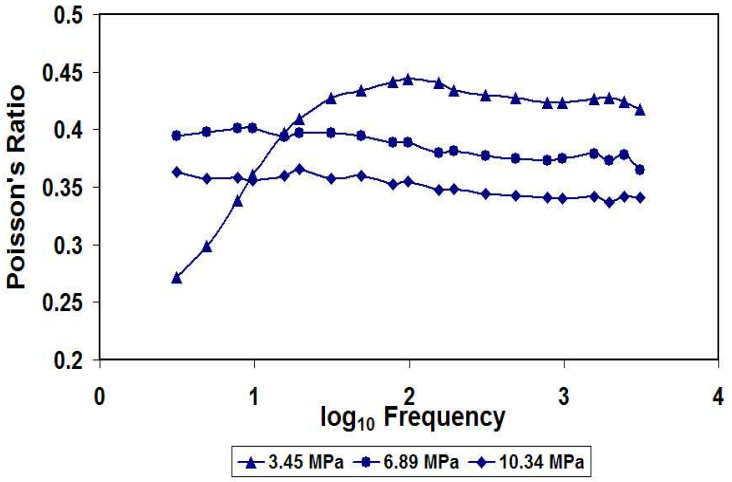

(a) Poisson's ratio with increasing differential pressure.

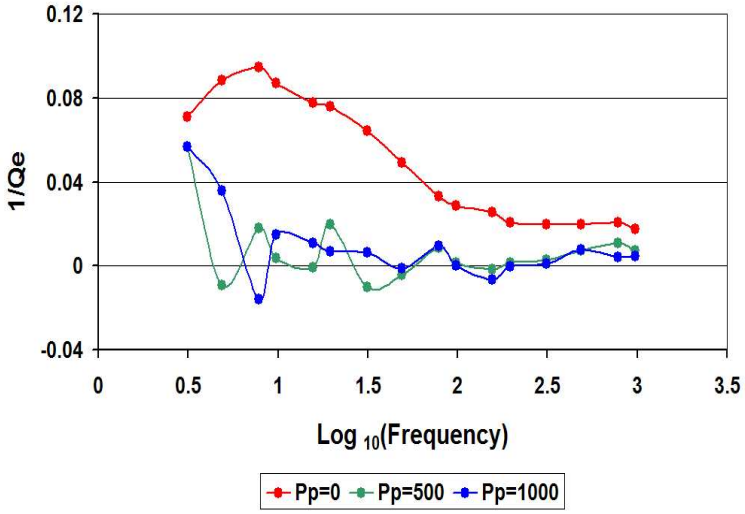

(b) 1/Qe with increasing pore pressure.

FIG. 5.31. Foxhill's sandstone: Increase in differential pressure and pore pressure gets rid of the clay swelling pressure and water vapor respectively.

Chapter 6

CONCLUSIONS

Attenuation and velocity dispersion are strongly dependent on fluid type, saturation, mobility and distribution. Thus attenuation measurements are useful in estimating the fluid properties like viscosity, degree of saturation and to identify zones of high permeability.

Seismic attenuation is closely related to velocity dispersion. Dry rock attenuation and velocity dispersion is negligible. In some cases where the dry rock has moisture the values may be quite high. At partial saturation, attenuation increases and *compressional* attenuation is twice as large as *shear*. At full saturation, *compressional* attenuation drops significantly and becomes one-third of the *shear* attenuation. Open and close boundary conditions make a significant difference in compressional velocity and attenuation for fully-saturated rock. Open boundary allows macroscopic fluid fluid flow where liquid from region of low compressibility flows to a region of high compressibility (gas). The three different types of saturation conditions is shows in figure 6.1. Only at low-frequencies can we distinguish between open and close boundary conditions and the crossover frequency depends on the fluid mobility. At low-frequencies a fully saturated rock acts as partially saturated if the boundary is open for the fluid to equilibrate with the surrounding. This causes a significant drop in *compressional* velocity and an increase in *compressional* attenuation. Thus, depending on the frequency of investigation, the velocity and attenuation values will be significantly different.

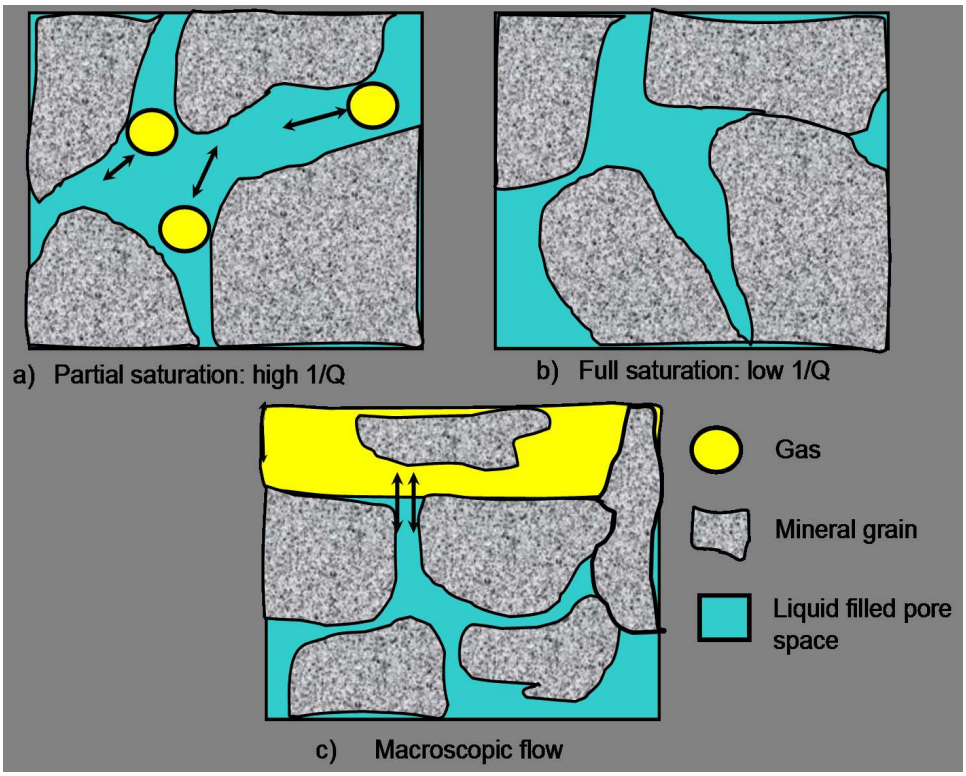

FIG. 6.1. Change in attenuation with saturation state of a rock.

As the differential pressure is increased the velocities increase and attenuation drops due to the closing of compliant pores or cracks. The rate of increase in velocity is high for lower differential pressures and reduces with increased differential pressure. The rate of decrease in attenuation ($\frac{1}{Q}$) is high for lower differential pressures. At higher differential pressures this rate becomes almost constant. The rate of change in attenuation is dependent on the saturation state of the rock. Only the heavy oil sample (Uvalde carbonate) showed a reversed trend, as the velocities decreased with increasing apparent differential pressure and this may be due to pore pressure coupling with the confining pressure.

A change in mobility of the fluid inside a rock shifts the peak attenuation frequency or the relaxation peak. Biot's prediction that an increase in viscosity or a decrease in permeability would shift the peak toward higher frequencies, was found invalid through my measurements. This result becomes very significant if we are trying to model the change in attenuation with changing fluid mobility. These kinds of measurements or associated modeling are particularly useful in thermal Enhanced Oil Recovery (EOR) processes where the change in viscosity could be detected through attenuation measurements [Ken Headlin, 2001].

Two different mechanisms of partial saturation were compared. In the first case the size of the saturated regions are larger than the pore size and in the second case individual pores are partially saturated. There was no perceptible difference in the velocity or attenuation measurements done with these two different saturation mechanisms. At partial saturations there is significant velocity dispersion as the ultrasonic compressional velocity increases with liquid saturation and low-frequency velocity decreases. At around 90% liquid saturation the attenuation is maximum. At full saturation low-frequency velocity increases significantly and *compressional* attenuation drops. This result is also significant because at gas-oil and gas-water contact in homogeneous reservoir rocks, there is a transition zone where the gas saturation varies through a wide range (figure 6.2). This transition zone will be the zone of maximum attenuation. Also, during production as the pressure drops, the gas may come out of solution creating distributed pockets of free gas and cause very high attenuation. Attenuation measurements could be used to monitor this transition zone. A layer of gas saturation on top of a liquid saturation acts as an open boundary condition and causes a drop in velocity and and increase in attenuation. This kind of situation may exist where shale stringers or laminae may trap local pockets of gas and create

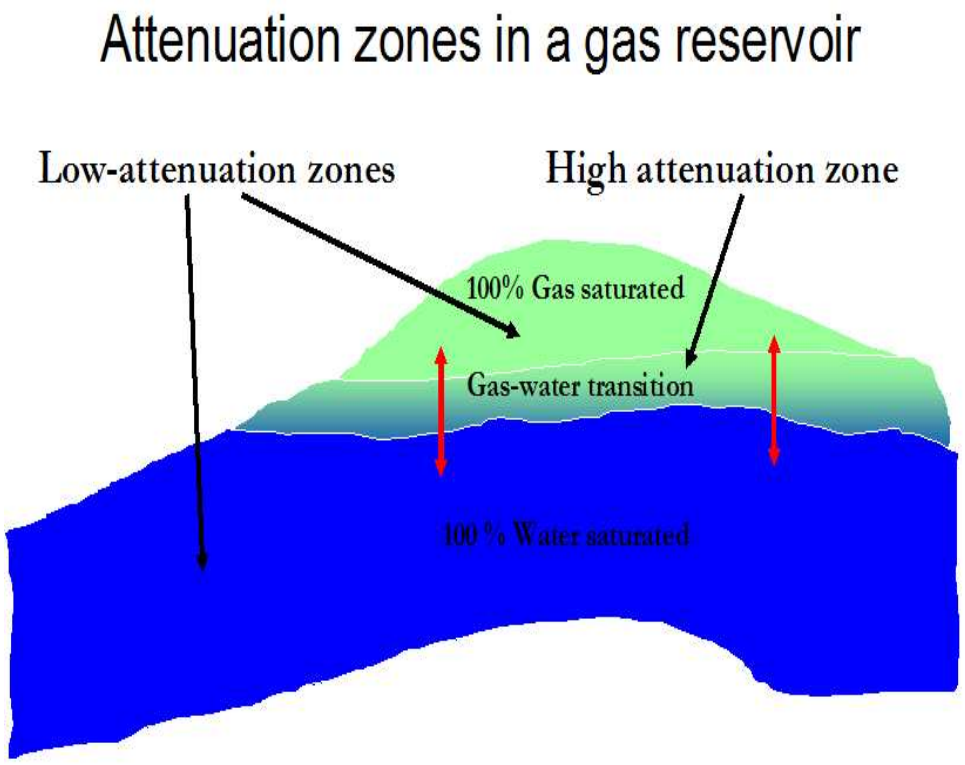

FIG. 6.2. Gas water transition zone produces highest compressional attenuation.

a multitude of gas-liquid contacts.

Different fluid contents within a rock causes a change in velocities and attenuation. Gassmann's substitution does a reasonably good job in predicting the velocity changes. Change in *Compressional* attenuation is governed by the type of fluid and the degree of saturation. Dry and gas saturated rocks have very low *compressional* attenuation and with partial liquid saturation the attenuation increases. *Shear* attenuation can not resolve the different fluid types and distribution if the degree of saturation is comparable (ie % liquid saturation is same) and water is the wetting phase.

The effect of clay on velocity and attenuation measurements is significant as they can alter the rock properties. Clay fluid reaction increase the Poisson's ratio (rock becomes soft). Due to clay swelling inside the pore spaces, the permeability of the rock decreases which means a drop in fluid mobility, causing a shift in the relaxation peak to lower frequencies.

Chapter 7

DISCUSSION AND RECOMMENDATIONS

In this chapter I would discuss about the possible ways to improve the measurement technique. Then some of the important results from my thesis would be compared with similar results obtained by other individuals and group. Then I will conclude with recommendations for future work.

As pointed out in Chapter 4, one of the issues with low-frequency stress-strain measurements is the proper extraction of the amplitude and phase angles form a noisy signal. The time required for data acquisition is also important. Currently it takes around half hour to run one set of measurements. One of the areas of improvement would be to reduce this acquisition time and also increase the frequency bandwidth to include even lower frequencies ($\leq 22Hz$).$These couldbedoneintwodifferentways$:

1)$Hardware$:

- Build a new acquisition system which would be run parallel to the present system so that separate data analysis could be done.
- Increase the digitizing rate of the A/D converter.

2) Software

- Improve the Matlab algorithm to reduce the acquisition time and include lower frequencies.
- Update the Labview subroutine to include more frequencies.

The effect of permeability on attenuation was examined using four ITF samples which have similar porosity but different permeability. The increase in permeability increases the mobility, allowing a decrease in relaxation time, which corresponds to higher relaxation peak frequency. Also, at a given frequency the attenuation dropped with increasing permeability. Similar effect was observed by Dvorkin, Hoeksema and Nur [1994]. They modeled the results of Klimentos and McCann [1990] where ultrasonic (1 MHz) Velocity and attenuation were measured as a function of permeability for 16 water saturated samples. They observed that at small permeabilities the attenuation increases to its maxima at intermediate permeability and then decreases for higher permeability (figure 7.1). The result can be understood by examining the behavior of velocity and attenuation as a function of frequency and mobility. We know that the largest change in velocity occurs at the peak relaxation frequency which corresponds to a maxima in the attenuation curve (figure 7.2). At other frequencies the attenuation is small for a single relaxation process. At low permeability (low-mobility), the pore fluid is unrelaxed and attenuation is small (corresponds to high frequencies). At high permeability (high mobility) the pore fluid is relaxed and again attenuation is small (corresponds to low frequencies). There fore the attenuation maxima is situated between these two extreme permeabilities (corresponds to relaxation peak).

In the Uvalde carbonate sample we saw that the velocity decreased with increasing confining pressure. The velocity decreased with increasing temperature. These results were contrary to the results obtained with other samples. The unexpected behavior was due to the presence of heavy oil in the pore spaces of the Uvalde carbonate and has been discussed in the Chapter 5. The attenua-

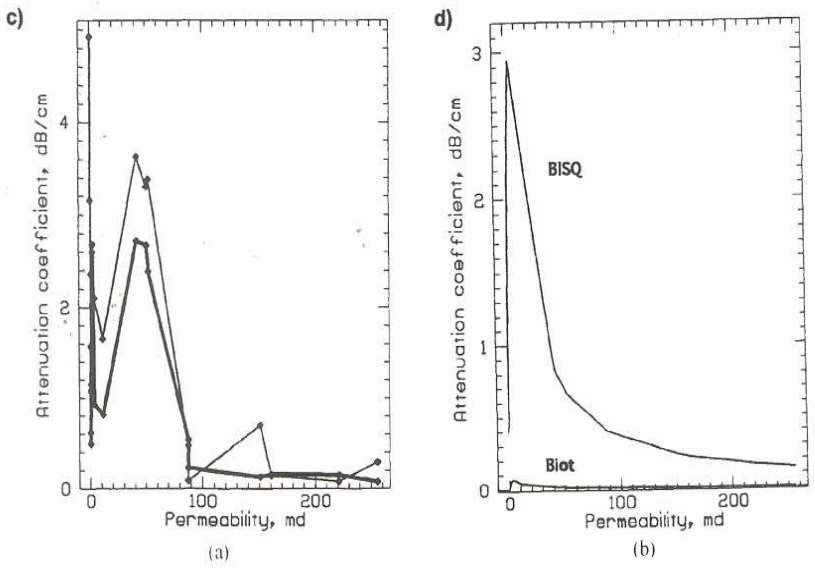

(a) Attenuation coefficient versus permeability-regular scale.
(b) Attenuation coefficient versus permeability-hypothetical samples.

FIG. 7.1. (a) Attenuation coefficient versus permeability for the selected 16 samples. (b) Comparison between Biot and BISQ attenuation as a function of frequency for some hypothetical samples.

tion decreased with decreasing temperature (increasing viscosity) and the peak relaxation frequency was smaller than the seismic frequency range. Thus, the seismic frequencies act as the ultrasonic frequencies where the pore pressure is unrelaxed. Ken Hedlin [2001] in his Master's thesis modeled attenuation for a very high viscosity oil reservoir and matched it with the attenuation values extracted from VSP data. His modeling result shows that peak attenuation frequency for the cold reservoir is around 0.1 Hz. Also with increase in temperature the viscosity of the oil decreases and the attenuation increases. He also men-

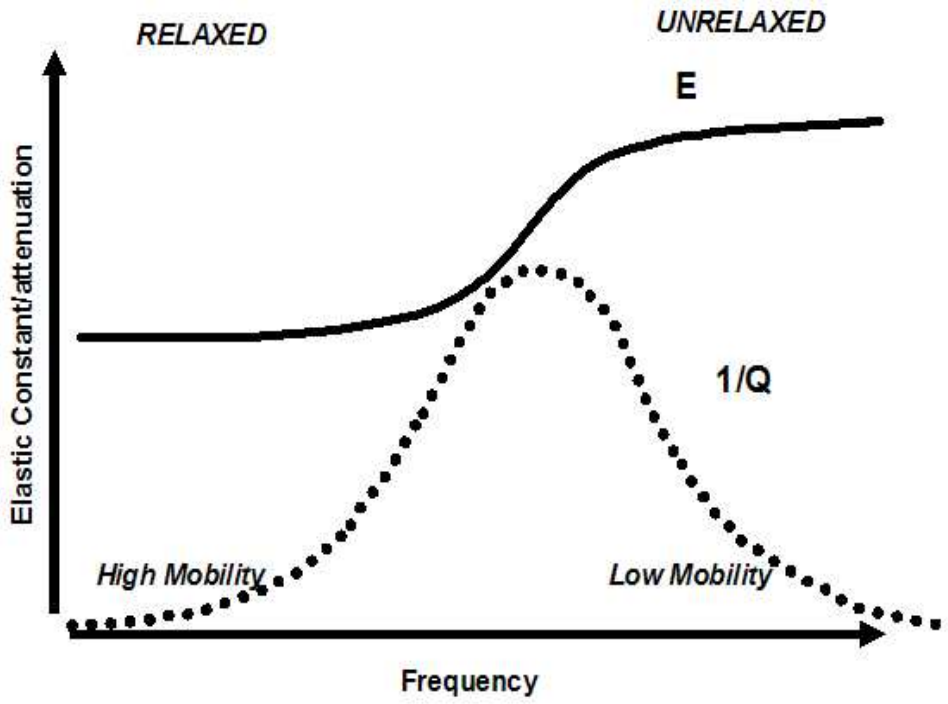

FIG. 7.2. Schematic relation among elastic moduli (or velocity), attenuation, frequency and fluid mobility. At low mobility, pore pressure remains unrelaxed, even at seismic frequencies. Hence, for low permeability rocks, the attenuation is small. At high mobility (high permeability rocks) the pore pressure is relaxed and again attenuation is small. At intermediate permeability there is attenuation maxima.

tions that with increase in temperature the velocity decreased. His conclusions match exactly with my laboratory measurements. The modeled attenuation curve is shown in figure 7.3(a) and the compressional attenuation measurement for Uvalde carbonate is shown in figure 7.3(b). More such measurements should be made with heavy oil samples. The heavy oil could be extracted out of the rock sample. It would be interesting to measure velocity and attenuation on the Uvalde sample with different fluid substitution.

In order to compare the difference between local and global permeability two different saturation methods were used. In the first method the size of the saturation patches were bigger than the pore size and in the second method partial saturation was achieved at pore scale level. Measurements done on ITF-43 sample showed that there is no difference between the local and global permeability for this sample. Also, fluid substitutions done on ITF-43 sample confirmed the theory and were consistent in a qualitative sense, but more measurements with different fluid substitutions and distributions should be made with greater control on fluid distribution and boundary conditions to quantitatively match the theory. One suggestion would be to take x-ray images of saturated rocks in order to understand the effect of viscous fingering and gravity similar to Cadoret [1998]. Better understanding of the fluid distribution would also help to better model the rock for velocity and attenuation measurement.

It has been mentioned that the gas-water transition zone produces the highest attenuation compared to a gas saturated or a water saturated zone. In order to test this an experiment could be designed where the transition zone is increased in steps and the change in attenuation and velocity dispersion is monitored. If the attenuation increases with an increase in transition zone then we can confirm this hypothesis.

Finally, the effect of clays on attenuation and velocity dispersion should be examined in more detail. More clay rich rocks should be measured and a detailed analysis of the clays should be done before making the measurements. More sensitive clays should be compared with less sensitive clays. Also, clays with different structures should be compared. It would be interesting to differenti-

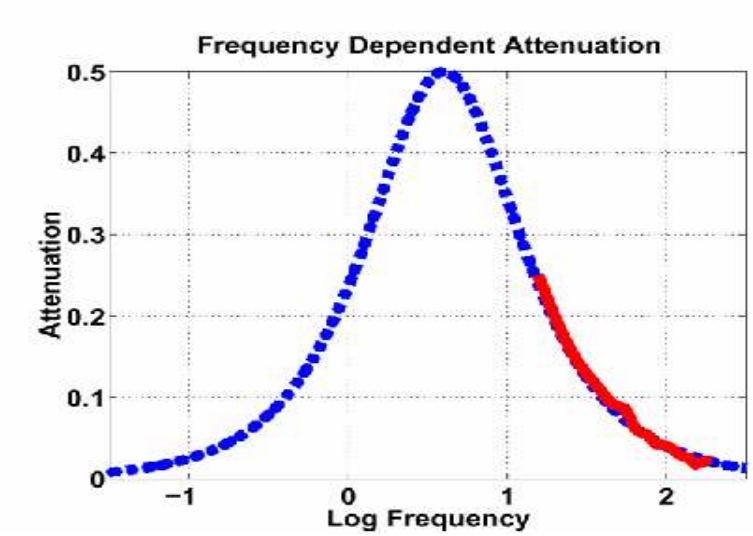

(a) Modeled and measured attenuation as a function of frequency for a heavy oil reservoir. The peak attenuation frequency is less than 10Hz.

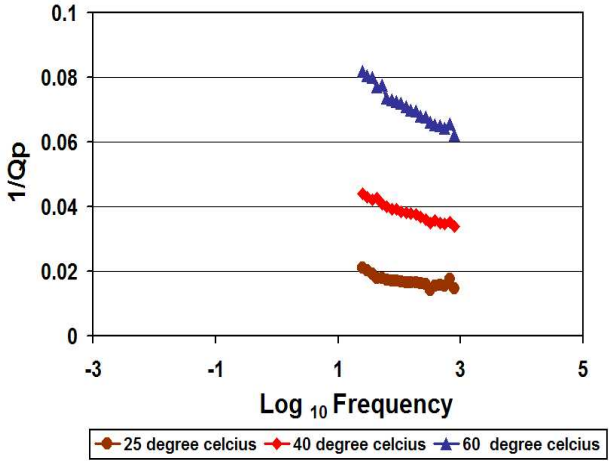

(b) Uvalde carbonate: Change in attenuation with temperature. Notice the increase in attenuation with increasing temperature.

FIG. 7.3. Comparison of Ken Hedlin's [2001] modeled and measured attenuation values for a heavy oil reservoir with the laboratory measurement done on Uvalde carbonate sample which is filled with heavy oil.

ate between a pore lining clay and a pore filling clay type based on velocity dispersion and attenuation measurements.

REFERENCES

Abeele, K.E.-A.V.D., Carmeliet, J., Johnson, P.A., and Zinszner, B., 2002, Influence of water saturation on the nonlinear elastic mesoscopic response in Earth materials and the implications to the mechanism of nonlinearity.

Batzle, M.L., 2003, Personal communication.

Biot, M.A., 1956a, Theory of propagation of elastic waves in a fluid-saturated porous solid, I: Low-frequency range, Journal of Acoustical Society of America, **28**, 168-178.

Biot, M.A., 1956b, Theory of propagation of elastic waves in a fluid-saturated porous solid, II: Higher frequency range, Journal of Acoustical Society of America, **28**, 179-191.

Cadoret, T., Mavko, G., and Zinszner, B.E., 1998, Fluid distribution effect on sonic attenuation in partially saturated limestones, Geophysics, **63**, 154-160.

Castagna, J.P., Sun S., and Siegfried, R.W., 2003, Instantaneous spectral analysis: Detection of low-frequency shadows associated with hydrocarbons, The Leading Edge, **22**, 120-127.

Clark, V.A., Spencer, T.W., Tittmann, B.R., Ahlberg, L.A., and Coombe, L.T., 1980, Effect of volatiles on attenuation (Q^{-1}) and velocity in sedimentary rocks, Journal of Geophysical Research, **85**, 5190-5198.

Cole, K.S and Cole, R.H, 1941, Dispersion and absorption in dielectrics I. Alternating current characteristics, J. Chem. Phys., **9**, 341-351.

Domenico, S.M., 1977, Elastic properties of unconsolidated porous sand reservoirs, Geophysics, **42**, 1339.

Dutta, N.C. and Odé, H., 1979, Attenuation and dispersion of compressional waves in fluid-filled porous rocks with partial gas saturation (White model)-Part 1: Biot theory, Part II: Results, Geophysics, **44**, 1777-1805.

Dvorkin, J., Mavko, G., and Nur, A., 1995, Squirt flow in fully saturated rocks, Geophysics, **60**, 97-107.

Dvorkin, J. and Nur, A., 1993, Dynamic poroelasticity: A unified model with the squirt and the Biot mechanisms, Geophysics, **58**, 524-533.

Futterman, W.I., 1962, Dispersive body waves: J. Geophys. Res., **67**, 5279-5291.

Gardner, G.H.F., Wyllie, M.R.J., and Droschak, D.M., 1964, Effect of pressure and fluid saturation on the attenuation of elastic waves in sands, J. Petr. Tech., 189-198.

Gassmann, F., 1951, Über die Elastizität poröser Medien, *Vier. der Natur. gesellschaft in Zürich*, **96**, 1-23.

Gist, G.A., 1994, Interpreting laboratory velocity measurements in partially gas-saturated rocks, Geophysics, **59**, 1100-1109.

Goloshubin, G.M., Daley, T.M., Korneev, V.A., and Vingalov., V.M., 2002, Seismic low-frequency effects from oil-saturated reservoir zones: Expanded Abstracts, SEG meeting, Salt lake City.

Goloshubin, G.M., Daley, T.M., and Korneev, V.A., 2001, Seismic low-frequency effects in gas reservoir monitoring VSP data: Expanded Abstracts, SEG meeting, San Antonio.

Goloshubin, G.M., Korneev, V.A., 2000, Seismic low-frequency effects from fluid-saturated reservoir: Expanded Abstracts, SEG meeting, Calgary.

Gordon, R.B., and Davis, L.A., 1968, Velocity and attenuation of seismic waves in imperfectly elastic rock: J. Geophys. Res., **73**, 3917-3935.

Hedlin, K., 2001, Steam Flood Delineation Using Attenuation at Husky's Pikes Peak Project, Master's Thesis.

Hofmann, R., 2001, On Gassmann's equation: Colorado School of Mines, Geophysics department, Master's Thesis, Golden, Co.

Hofmann, R., 2003, Personal communication.

Kjartansson, E. and Delinger R., 1977, Seismic wave attenuation due to thermal relaxation in porous media, Geophysics, **42**, 7, 1516.

Klimentos, T. and McCann, C., 1990, Relationships among compressional wave attenuation, porosity, clay content, and permeability in sandstones, Geophysics, **55**, 998-1014.

Mavko, G.M. and Jizba, D., 1991, Estimating grain-scaled fluid effects on velocity and dispersion in rocks: Geophysics, **56**, 1940-1949.

Mavko, G.M. and Nur, A., 1979, Wave attenuation in partially saturated rocks, Geophysics, **44**, 161-178.

Mochizuki, S., 1982, Attenuation in partially saturated rocks, J. Geophys. Res., **87**, 8598-8604.

Mörig, R., and Burkhardt H., 1989, Experimental evidence for the Biot-Gardner theory, Geophysics, **54**, 524-527.

Murphy, W., Reischer, A., and Hsu, K., 1993, Modulus decomposition of compressional and shear velocities in sand bodies, Geophysics, **58**, 227-239.

Nowick, A.S. and Berry, B.S., 1972, Anelastic relaxation in crystalline solids: Academic Press.

Nur, A., and Simmons, G., 1969a, The effect of viscosity of a fluid phase on velocity in low-porosity rock, Earth Planet. Sci. lett., **7**, 183-193.

O'Connell, R.J and Budiansky, B., 1977, Viscoelastic properties of fluid-saturated cracked solids: J. Geophys. Res., **82**, 5719-5735.

Plona, T.J., 1980, observation of a second bulk compressional wave in a porous medium at ultrasonic frequencies, Appl. Phys. Lett., **36**, 259-261.

Spencer, J.W., Jr., 1981, Stress relaxation at low frequencies in fluid saturated rocks: attenuation and modulus dispersion, J. Geophys. Res., **86**, 1803-1812.

Spencer, J.W., Jr., 1979, Bulk and shear attenuation in Berea sandstone: The effects of pore fluids, J. Geophys. Res., **84**, 7521-7523.

Taner, M.T., et al, 1976, extraction of complex seismic trace, 46th Ann. Mtg., Soc. Exploration Geophys., Houston.

Tittmann, B.R., Nadler, H., Clark, V.A., Ahlberg, L.A., and Spencer, T.W., 1981, Frequency dependence of seismic dissipation in saturated rocks, Geophys. Res. lett., **8**, 36-38.

Toksöz, M.N. and Johnston, D.H., 1981, Seismic Wave Attenuation: Geophysics reprint series No. 2.

Walsh, J.B., 1966, Seismic wave attenuation in rock due to friction, J. Geophys. Res., **71**, 2591-2599.

Winkler, K. and Nur, A., 1979, Pore fluids and seismic attenuation in rocks: Geophys. Res. Lett., **6**, 1-4.

Winkler, K. and Nur, A., and Gladwin, M., 1979, Friction and seismic attenuation in rocks: Nature, **277**, 528-531.

White, J.E., 1983, Underground Sound: Application of Seismic Waves: Elsevier.

White, J.E., 1975, Computed seismic speeds and attenuation in rocks with partial gas saturation: Geophysics, **40**, 224.

White, J.E. and Zechman, R.E, 1968, Computed response of an acoustic logging tool, Geophysics, **33**, 302-310.

White, J.E., 1965, Seismic waves: radiation, transmission, and attenuation: New York, McGraw-Hill Book Co., Inc.

Wideman, C.J. and Major, M.W., 1967, Strain steps associated with earthquakes, Bulletin of the Seismological Society of America, **57**, 1429-1444.

Wyllie, M.R.J., Gardner, G.H.F and Gregory, A.R., 1962, Studies of elastic wave attenuation in porous media, Geophysics, **27**, 569-589.

Wyllie, M.R.J., Gregory, A.R., and Gardner, G.H.F., 1958, An experimental investigation of factors affecting elastic wave velocities in porous media, geophysics, **23**, 459-493.

APPENDIX A

When a medium is attenuative, the relation between the stress and the strain involves a time shift. To analyze this we assume that the applied stress, observed strain and the moduli are all complex quantities. An important assumption is made in order to derive the relation between different modes of attenuation (Q_E, Q_S, Q_P, Q_K) is that the imaginary component of the moduli (and thus the attenuation) is very small and any second or higher order terms can be neglected.

It has been discussed in the theory section that

$$\frac{1}{Q} = \frac{M_I}{M_R} \tag{1}$$

If we consider the Young's modulus to be complex then :

$$E = E^{''} + \iota E^{''} \tag{2}$$

$$\frac{1}{Q_E} = \frac{E^{''}}{E^{'}} = tan\delta_E \tag{3}$$

where E is the Young's modulus and $E^{'}$ is the real part of the Young's modulus and $E^{''}$ is the imaginary part of Young's modulus and tanδ_E is the phase angle between the applied stress and observed strain in a Young's modulus type experiment (like our measurement).

Shear modulus (μ) is related to the Young's modulus and the Poisson's ratio

(ν) as:

$$\mu = \frac{E}{2(1+\nu)} \tag{4}$$

In case of a complex shear modulus the real part follows this relation (eqn 4). In order to compute the relation between the imaginary component we consider the equation 4 but assume that all the moduli and the Poisson's ratio are complex. Thus,

$$\mu^{'} + \iota\mu^{''} = \frac{E^{'} + \iota E^{''}}{2(1+\nu^{'} + \iota\nu^{''})} \tag{5}$$

$$\tag{6}$$

comparing the imaginary part on both sides of eqn. 5 and neglecting $\nu^{''2}$ we get the imaginary part of the shear modulus in terms of Young's modulus and Poisson's ratio:

$$\mu^{''} = \frac{(1+\nu^{'})E^{''} - E^{'}\nu^{''}}{2(1+\nu^{'})^2} \tag{7}$$

where ' stands for real part and " stands for imaginary part of the quantities. If the real part of the shear modulus takes the form equation 4 then the shear attenuation $\frac{1}{Q_S}$ is given as:

$$\frac{1}{Q_S} = \frac{\mu^{''}}{\mu^{'}} = \frac{(1+\nu^{'})\frac{E^{''}}{E^{'}} - \nu^{''}}{(1+\nu^{'}} \tag{8}$$

$$= \frac{(1+\nu^{'})\frac{E^{''}}{E^{'}} - \nu^{'}\frac{\nu^{''}}{\nu^{'}}}{(1+\nu^{'})} \tag{9}$$

If we define a Poisson's loss tangent as

$$tan\delta_\nu = \frac{\nu''}{\nu'} \tag{10}$$

then we get

$$\frac{\mu''}{\mu'} = \frac{(1+\nu')tan\delta_E - \nu' tan\delta_\nu}{(1+\nu')} \tag{11}$$

If we assume that the real part of the Poisson's ratio is approximately equal to the magnitude (small loss)and using eqn 3 we get the shear attenuation as

$$\frac{\mu''}{\mu'} = \frac{1}{Q_S} = \frac{(1+\nu')\frac{1}{Q_E} - \nu' tan\delta_\nu}{(1+\nu')} \tag{12}$$

where tan δ_ν is the phase angle difference between the horizontal (Poisson's gage) and vertical (Young's gage). In our experiment we measure this phase angle and compute the shear attenuation ($\frac{1}{Q_S}$) using eqn 12.

The Bulk modulus (K) is related to the Young's modulus and the Poisson's ratio as

$$K = \frac{E}{3(1-2\nu)} \tag{13}$$

As in the case with shear modulus if we consider all the moduli in eqn 13 to be complex then we get

$$K' + \iota K'' = \frac{E' + \iota E''}{3(1-2(\nu' + \iota\nu''))} \tag{14}$$

Equating the imaginary parts of eqn 14 and neglecting ν''^2 we get the imaginary

part of the bulk modulus

$$K'' = \frac{(1-2\nu')E'' + 2E'\nu''}{3(1-2\nu')^2} \tag{15}$$

If the real part of the bulk modulus takes the form of eqn 13 then from equation 15 the bulk attenuation $\frac{1}{Q_K}$ is given as

$$\frac{1}{Q_K} = \frac{K''}{K'} = \frac{E''}{E'} + \frac{2\frac{\nu''}{\nu'}\nu'}{(1-2\nu')} \tag{16}$$

$$\tag{17}$$

Using eqn 3 and 10 we get

$$\frac{1}{Q_K} = \frac{1}{Q_E} + \frac{2tan\delta_\nu \nu'}{(1-2\nu')} \tag{18}$$

Now, replacing tanδ_ν from eqn 12 in eqn 18 and assuming that imaginary part of Poisson's ratio is almost equal to the magnitude we get

$$\frac{3}{Q_E} = \frac{(1-2\nu)}{Q_K} + \frac{2(1+\nu)}{Q_S} \tag{19}$$

The P-wave modulus (M) is related to the bulk modulus and the shear modulus as

$$M = K + \frac{4}{3}\mu \tag{20}$$

Using eqns 4 and 13 we get the P-wave modulus in terms of Young's modulus

and Poisson's ratio we get

$$M = \frac{E(1-\nu)}{(1-\nu-2\nu^2)} \tag{21}$$

Using the same steps as before we the imaginary part of the P-wave modulus ($M^{''}$) as

$$M^{''} = \frac{(1-\nu^{'2})(1-2\nu^{'})E^{''} + 2E^{'}\nu^{'}(2-\nu^{'})\nu^{''}}{(1-\nu^{'}-2\nu^{'2})^2} (from\, White\, 1965) \tag{22}$$

The P-wave attenuation $\frac{1}{Q_P}$ is given as

$$\frac{1}{Q_P} = \frac{M^{''}}{M^{'}} = \frac{(1+\nu^{'})(1-2\nu^{'})}{(1-\nu^{'}-2\nu^{'2})}\frac{E^{''}}{E^{'}} + \frac{2(2-\nu^{'})\nu^{''}\nu^{'}}{(1-\nu^{'}-\nu^{'2})(1-\nu^{'})} \tag{23}$$

$$\tag{24}$$

using eqns 3, 10 and factorizing $(1-\nu^{'}-2\nu^{'2}) = (1+\nu^{'})(1-2\nu^{'})$ we get

$$\frac{1}{Q_P} = \frac{1}{Q_E} + \frac{2(2-\nu^{'})\nu^{'2}tan\delta_\nu}{(1-2\nu^{'})(1+\nu^{'})(1-\nu^{'})} \tag{25}$$

$$= \frac{1}{Q_E} + \frac{\nu^{'}tan\delta_\nu}{(1+\nu^{'})}\frac{2\nu^{'}(2-\nu^{'})}{(1-2\nu^{'})(1-\nu^{'})} \tag{26}$$

Using eqn 12 we get

$$\frac{1}{Q_P} = \frac{1}{Q_E} + \frac{2\nu^{'}(2-\nu^{'})}{(1-2\nu^{'})(1-\nu^{'})}\left(\frac{1}{Q_E} - \frac{1}{Q_S}\right) \tag{27}$$

Ordering and rearranging the terms and substituting the imaginary part of the

Poisson's ratio with the magnitude (small attenuation) we get

$$\frac{(1-2\nu)(1-\nu)}{Q_P} = \frac{(1+\nu)}{Q_E} - \frac{2\nu(2-\nu)}{Q_S} \tag{28}$$

We use eqn 28 to compute P-wave attenuation ($\frac{1}{Q_P}$) given $\frac{1}{Q_E}$ and $\frac{1}{Q_S}$. Substituting $\frac{1}{Q_E}$ with $\frac{1}{Q_S}$ and $\frac{1}{Q_K}$ (using eqn 19) into eqn 28 we get the final relation between $\frac{1}{Q_K}$,$\frac{1}{Q_S}$ and $\frac{1}{Q_P}$ as:

$$\frac{(1+\nu)}{Q_K} = \frac{3(1-\nu)}{Q_P} - \frac{2(1-2\nu)}{Q_S} \tag{29}$$

APPENDIX B

Matlab program for data acquisition using SRS-850 DSP Lock-In Amplifier.
This program collects data from six channels.

```
**************************************************************************
**************************************************************************

p=gpib('ni',0,5);     % assigning a variable to the SRS-850 lock-in amplifier%
v=gpib('ni',0,4);     % assigning a variable to switch 1%
sw=gpib('ni',0,2);    % assigning a variable to switch 2 %

**************************************************************************
**************************************************************************

p.timeout=100;
p.inputbuffersize=50000;   % set the input buffer size of the amplifier%
p.outputbuffersize=50000; % set the output buffer size of the amplifier %
fopen(p);              % set the amplifier on remote communication %
fopen(v);              % set switch 1 on remote communication %
fopen(sw);             % set switch 2 on remote communication %

**************************************************************************
**************************************************************************

fprintf(p,'OUTX1'); % set the output interface of the amplifier to GPIB %
```

```
set(p,'EOSMode','readwrite') % set end of statement to read and write %
fprintf(p,'FMOD0');     % reference source is set as internal %
fprintf(p,'PHAS0');     % reference phase shift is set to zero %
fprintf(p,'RSLP1');     % sets the reference slope to sine zero crossing %
fprintf(p,'SYNC1');     % synchronous filter is switched on%
fprintf(p,'oflt8');         % time constant is set to 100 ms %

**************************************************************************
**************************************************************************

rep=menu('Save the data in a file','yes','no');
if rep==1
name=input('Please give a file name to save the data ::','s');
end

**************************************************************************
**************************************************************************

% set the trace definition for X=in phase, Y=quadrature, R=amplitude, θ=phase
angle %

for i=1:4
fprintf(p,['TRCD' num2str(i) ',' num2str(i) ',' '0' ',' '0' ',' '1'])
end

fprintf(p,'slvl.15'); % set the amplitude of the sine output to 0.15 Volts %
```

```
**************************************************************************
**************************************************************************
% generate a list to select the channels for data acquition %
[tr,v1]=listdlg('promptstring','Select the channels for data collection','listsize',[160
100], ...
'liststring',str2mat('X(in phase)','Y(quadrature)','R(amplitude)','Theta(phase an-
gle)'));
s=size(tr,2); % number of traces selected

**************************************************************************
**************************************************************************
% generates a choice list to either select interactive data acquition or use the
default setting %
ch=menu('Start the default frequency sweep or interactive','Interactive','Default');
if ch==1 % if interactive %

****************************************
input the frequency range and increment
****************************************
sf=input('The starting frequency::');
ef=input('The end frequency::');
inc=input('The frequency increment::');
```

```
**************************************
loop to generate the data and store it
**************************************

j=1;

for i=sf:inc:ef
data(j,1)=log10(i);                % save the frequency in the first column
fprintf(p,['FREQ' num2str(i)]) % generate the signal at the given frequency
pause(20/i)

for k=1:s                          % for the traces selected
fprintf(p,['OUTR?' num2str(tr(k))]) % read the value of kth trace
data(j,k+1)=str2num(fscanf(p));      % save the data
pause(1) % pause for 1 second before collecting data from next trace
end

j=j+1;
end

else % default frequencies

fre= logspace(1.4,2.9,20); % generate logarithmically spaced frequencies
s1=size(fre,2);                % total no of frequency points
for i=1:s1
data(i,1)=log10(fre(i));     % save log frequencies in first column
```

```
end

clear i;
ref=0; % to track the column entry for data

******************************************
to collect data from all 6 channels
******************************************
for cha=1:6

['Collecting data from channel ' num2str(cha)]

************************************************
select the proper channel by combining switches
************************************************ if cha≤ 4
fprintf(sw,'A1')
fprintf(v,['A' num2str(cha)])
else
fprintf(sw,'A2')
fprintf(v,['B' num2str(cha-4)])
end

******************************************
collect data for each channel
******************************************
```

```
fprintf(p,'oflt10'); % change the time constant to 1 second

for i=1:12 % generate frequencies between 10Hz and 100Hz
fprintf(p,['FREQ' num2str(fre(i)) ]) % set the driving frequency
pause(15);                           % acquisition time
for k=1:s                            % for all the traces selected
fprintf(p,['OUTR?' num2str(tr(k))]) % read the value of kth trace
data(i,ref+k+1)=str2num(fscanf(p)); % save the data
pause(1)
end
end

clear i;


fprintf(p,'oflt9'); % change the time constant to 300 ms

for i=13:20 % generate frequencies between 200Hz and 1000Hz
fprintf(p,['FREQ' num2str(fre(i)) ]) % set the driving frequency
pause(10);                           % acquisition time
for k=1:s                            % for all traces selected
fprintf(p,['OUTR?' num2str(tr(k))]) % read the value of kth trace
data(i,ref+k+1)=str2num(fscanf(p)); % save the data
pause(1)
end
```

```
end

ref=ref+k; % change the reference to the next channel
end % end of the loop for all the six channels
end % end statement to the if command for selecting interective or default set-
ting

**************************************************************************
**************************************************************************
% close and delete all the variables representing each equipment
fclose(p);
fclose(v);
fclose(sw);
delete(p);
delete(v);
delete(sw);

**************************************************************************
**************************************************************************
eval(['save ' name '.dat' ' data -ascii']) % save the data file with the given file
name
clear all;
```